# Satellite Laser Ranging and the ETALON Geodetic Satellites

Graham Michael Appleby

Doctor of Philosophy

The University of Aston in Birmingham

October 1996

The University of Aston in Birmingham

Satellite Laser Ranging and the ETALON Geodetic Satellites

Graham Michael Appleby

Doctor of Philosophy

1996

## Abstract.

The technique of Satellite Laser Ranging is today a mature, important tool with applications in many areas of geodynamics, geodesy and satellite dynamics. A global network of some 40 stations regularly obtains range observations with sub-cm precision to more than twelve orbiting spacecraft. At such levels of precision it is important to minimise potential sources of range bias in the observations, and part of the thesis is a study of subtle effects caused by the extended nature of the arrays of retro-reflectors on the satellites. We develop models that give a precise correction of the range measurements to the centres of mass of the geodetic satellites Lageos and Etalon, appropriate to a variety of different ranging systems, and use the Etalon values, which were not determined during pre-launch tests, in an extended orbital analysis. We have fitted continuous 2.5 year orbits to range observations of the Etalons from the global network of stations, and analysed the results by mapping the range residuals from these orbits into equivalent corrections to orbital elements over short time intervals. From these residuals we have detected and studied large un-modelled along-track accelerations associated with periods during which the satellites are undergoing eclipse by the Earth's shadow. We also find that the eccentricity residuals are significantly different for the two satellites, with Etalon-2 undergoing a year-long eccentricity anomaly similar in character to that experienced at intervals by Lageos-1. The nodal residuals show that the satellites define a very stable reference frame for Earth rotation determination, with very little drift-off during the 2.5 year period. We show that an analysis of more than about eight years of tracking data would be required to derive a significant value for $\dot{J}_2$. The reference frame defined by the station coordinates derived from the analyses shows very good agreement with that of ITRF93.

Key Words: Space Geodesy; Satellite Signatures; Non–Gravitational Forces

# Dedication

To Maggie, Chris and Caroline

# Acknowledgements

I am indebted to my employer, the Royal Greenwich Observatory, Cambridge, for giving me the opportunity to carry out this study. It is a pleasure to thank my external supervisor, Dr Andrew Sinclair, head of the Space Geodesy Group at RGO, for his continuing interest in the project, for many useful discussions and encouragement to complete the thesis. I thank my internal supervisor, Dr Phil Moore of the Department of Civil Engineering, for his interest in the project, and for discussions both during his visits to RGO and at occasional meetings at conferences and committee meetings. Finally I thank my colleagues at RGO for their moral support.

# Contents

# List of Figures

# List of Tables

# Chapter 1

# Introduction and Outline of Research

## 1.1 Introduction

Satellite Laser Ranging (SLR) began as a concept in 1962 when Plotkin [1] of the Goddard Space Flight Centre (GSFC) in Maryland, USA first proposed the development of accurate laser ranging to retro-reflectors on orbiting spacecraft in order to improve geodetic information. At that time optical and radar tracking of satellites was yielding station coordinates at the 100-metre level of accuracy. The interesting geophysical processes that are deforming the solid Earth, such as Earth tides and plate tectonic motions, were understood to be altering station coordinates at the level of only a few cm over timescales varying from sub-daily to several years. It was clear that only if the measurement techniques could reach the level of accuracy of a few cm, and carry out observations over many years, would they be able to challenge the theoretical work.

The first SLR observations, of the Beacon Explorer-B spacecraft in 1964 achieved metre-level precision in range, and showed that the technique was viable and potentially capable of reaching the required centimetric precision. These experiments prompted NASA to place retro-reflectors on the GEOS I and II spacecraft and on the Moon, and to start to develop more SLR stations. In 1975 France launched the first geodetic satellite STARLETTE into a relatively low 950 km orbit, and this was followed in 1976 when NASA launched its Laser Geodynamic Satellite LAGEOS into a near-circular, near polar

orbit at a height of nearly 6000 km. Both these satellites are inert, dense spheres, encrusted with a number of retro-reflecting corner-cubes specifically designed to reflect laser light back to the emitting tracking station. STARLETTE has a diameter of 24 cm, LAGEOS a diameter of 60 cm.

In 1979 NASA created the Crustal Dynamics Project (CDP) with the aim of 'developing Laser Ranging and Very Long Baseline Interferometry (VLBI) systems to obtain relative positions with ± 2 cm accuracy to define directions with respect to the inertial reference with a 0.001 arcsec accuracy: to monitor relative rates of motion of different parts of the Earth's crust well enough to infer irregularities in plate tectonic motions, and to monitor the wobbles and rotational variations to infer their excitations and dampings, as well as to determine accurately the orbits of the distant satellites (higher than 6000 km altitude)' [2].

This project formalised and consolidated the cooperative efforts between scientists and engineers which were already underway in several countries, and other independent groups worldwide began to design and build their own SLR systems.

During the 1970s, the accuracy of the best systems was at the decimetre level, limited mainly by the relatively long laser pulse-lengths that were in routine use at the time. For a typical pulse-length of some 30 cm, a large uncertainty exists in the measurement because it is impossible to relate the detected photons to their position within the pulse. However, advances in both laser and electronic technology continued such that within ten years the best systems were obtaining single-shot precisions of better than 5 cm. During the late 1970s the Royal Greenwich Observatory at Herstmonceux, in collaboration with the University of Hull, began to develop a UK SLR Facility, with the initial objective of making range measurements to LAGEOS during the daytime as well as at night to a single-shot precision of 5 cm. The first returns were obtained, from STARLETTE, on the night of 1983 March 31, followed a few hours later by observations of LAGEOS. Since those initial experiments, the station has become one of the most prolific and accurate systems in the world, regularly tracking more than 200 satellite passes each month, with a single-shot precision of about 8 mm.

In the following sections of this Chapter we discuss in more detail the technique of satellite laser ranging with particular emphasis on the UK system, and outline the current

research which focuses both on a deeper understanding of the measurement process, and on an analysis of SLR observations of two high-altitude Russian geodetic satellites.

## 1.2 Satellite Laser Ranging

The technique of SLR is, in principle, very simple. A short pulse of laser light is emitted from a telescope that is following the predicted position of an orbiting satellite, the time of emission is accurately recorded and an interval counter is started. The pulse of light reaches the corner-cube retro-reflectors on the satellite, and is directed back towards the telescope. Upon receipt of the reflected laser light, a high-speed detector generates an electronic signal, and the signal stops the interval counter. The round-trip time of flight is then calculated. Half this time of flight multiplied by the speed of light gives the range of the satellite at the emission time of the laser pulse, also known as the epoch of the observation. This process is shown schematically in Figure 1.1.

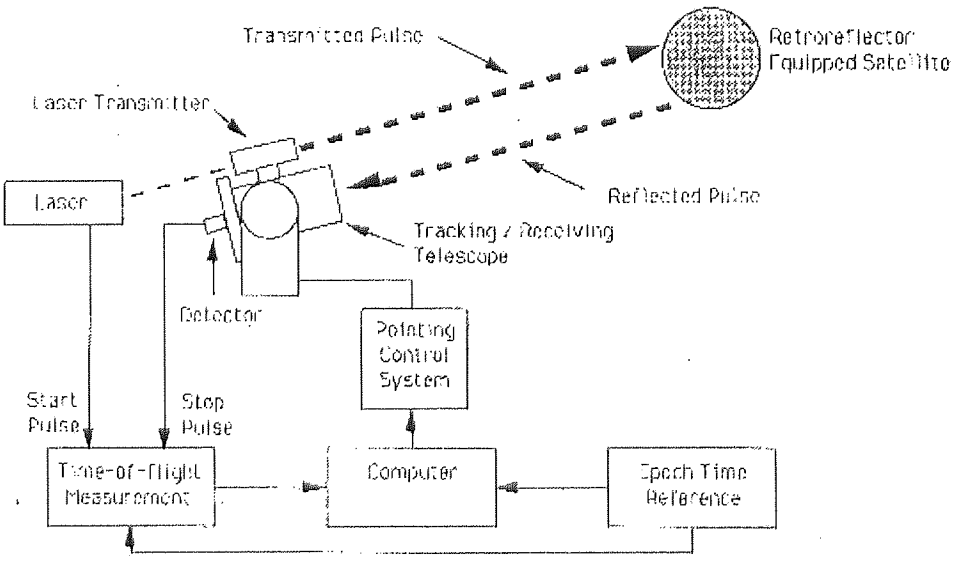


Figure 1.1: The Satellite Laser Ranging Technique

Given the objective of making range measurements to a precision of a few mm, we can estimate the precision with which the epoch of an observation must be recorded.

The speed of a typical geodetic satellite in its path around the Earth is about 5 km $s^{-1}$, or 5 $\times 10^6$ mm $s^{-1}$. Thus the epoch should be recorded to a precision of better that a micro-second. These days most stations record observational epochs with respect to the timescale broadcast by the Global Positioning System (GPS), which is precisely related to and closely aligned with Universal Time (UTC). The range measurement itself, of course, must be made to the required precision of a few mm, which in terms of two-way measured time of flight is equivalent to a precision of better than about 20 pico-seconds (20 ps = 20.0 $\times 10^{-12}$ s).

In order to convert this measurement precision into measurement accuracy, range calibration measurements are frequently carried out to a nearby reflective target-board, whose accurate distance from the invariant point of the ranging telescope has been independently surveyed. The calibration measurements are used to determine the sum of the internal electronic and optical-path delays in the ranging system, which is removed during a pre-processing stage from each raw range observation.

### 1.2.1 Tracking Stations

There are currently more than 40 active SLR systems in the worldwide network, regularly contributing observations to the data centres, from where they are rapidly available to the analysis community. Many of these instruments achieve a range precision of better than 1 cm rms. Many of the systems are associated with geodetic and astronomical stations, which also operate other geodetic systems such as permanent GPS receivers, PRARE (Precise Range and Range-Rate Experiment) ground stations, DORIS (Doppler Orbitography and Radiopositioning Integrated by Satellite) beacons, VLBI antennae and gravimeters. The UK station at Herstmonceux has a ROGUE GPS receiver which routinely contributes observations to the International GPS Service (IGS), has operated for a few months during 1995 a PRARE receiver belonging to the UK's Proudman Oceanographic Laboratory, and has recently had a first-epoch visit by an absolute gravimeter also belonging to POL.

Among the network of SLR stations there are essentially two different types, depending upon the original design specifications. Some are designed to work at a multi-photon level of return, whereby each returning pulse of reflected laser light is typically at the

level of at least 10 photons, and is often measured at several hundreds of photons. The detectors used in such systems are Micro-Channel Plate (MCP) detectors, which are very fast, physically small, multiple photomultipliers. The discriminating electronics associated with the MCP detectors are usually configured such that the detector is triggered by the leading edge of the returning laser pulse, leading to a very precise range measurement, affected little by the particular waveform of that pulse. All of the NASA systems fall into this category.

The second type of system, which includes the Herstmonceux station, works at or close to a single-photon level of return. The philosophy behind the design of such a system is that the ability to detect such low return levels improves the chances of making observations when atmospheric conditions are poor. For stations at or near sea level and in rapidly changing climates, such as many of the European stations, this ability maintains their competitiveness with systems working in dry conditions at high-altitude locations. The detectors usually used by the single photon systems are Single Photon Avalanche Diodes (SPADs), which are solid state devices with sensitive areas of the order of 100 microns in size. The SPAD is armed a short time before the returning laser pulse reaches the telescope. Either internal noise or an external photon, which may be background noise from the sky or from the satellite, will then trigger the avalanche within a few microseconds. Once an avalanche of photo-electrons has been triggered, the SPAD is unable to detect further photons until it is again armed during the next ranging cycle. In this way photons originating from anywhere within the returning pulse have the potential to be detected, provided they can be distinguished from the noise. If the returning pulse is at the level of single photons, then over the course of many hundreds of such detections during a satellite pass, the waveform of the whole return pulse will be sampled.

This essential difference between the multi and single-photon systems is explored in detail as part of this research. We investigate the determination of accurate corrections to refer range measurements made to the retro-reflectors on the surface of the satellites to the centres of mass of the satellites. The pre-launch tests to measure such corrections were carried out almost exclusively at multi-photon levels, and we find that the values appropriate to the single-photon mode of operation are significantly different from the

laboratory results. We also investigate the effects in terms of the potential bias introduced into the range measurements of departure from the single-photon return level. With ranging precision at the level of a few mm, it is essential that we understand such subtle effects if we are not to produce biased data which could appear to be or mask some small geophysical signal.

### 1.2.2 Satellites

A number of satellites is routinely tracked by the worldwide network of tracking stations, and for a variety of scientific applications. The satellites fall into two main classes; geodetic and applications. The geodetic satellites are small, spherical and inert, containing a high-density core and a surface uniformly covered with corner-cube reflectors (retro-reflectors). Figure 1.2 shows Etalon-1, which has a diameter of 129 cm, and carries 2146 retro-reflectors distributed over its surface. The satellites are designed to have a

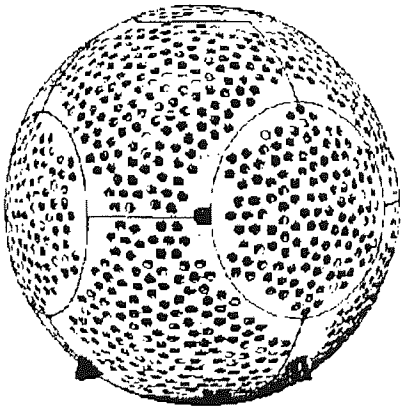

Figure 1.2: The Etalon-1 Geodetic Satellite.

small area to mass ratio to minimise accelerations due to non-gravitational forces such as from solar radiation pressure. Those geodetic satellites that are regularly tracked are listed in Table 1.1, which gives the satellites' diameters (cm) and dates of launch, in order of their heights in Km above the surface of the Earth. All are in near-circular orbits, and have diameters ranging from 20 cm to over 2 m. The principal applications addressed by observations of these satellites depend mainly upon their heights above the Earth. The low satellites GFZ-1, Starlette, Stella and Ajisai are particularly suited to determination of high-frequency terms in the expansion of the Earth's gravitational potential, studying

| Satellite | Height Km | Diam cm | Launch Year |
|---|---|---|---|
| GFZ-1 | 390 | 20 | 1995 |
| STARLETTE | 960 | 24 | 1975 |
| STELLA | 810 | 24 | 1993 |
| AJISAI | 1500 | 215 | 1986 |
| LAGEOS-I | 6000 | 60 | 1976 |
| LAGEOS-II | 6000 | 60 | 1992 |
| ETALON-I, II | 19000 | 129 | 1989 |

Table 1.1: Geodetic satellites tracked by SLR

ocean tides and modelling variations in atmospheric density. The Lageos satellites are extensively used for global terrestrial reference frame determination for studying crustal motions, Earth rotation and for determination of and monitoring changes in low frequency terms in the gravity field. The extent to which the Etalon satellites could also contribute to the Lageos applications is a major objective of this current research.

The applications satellites are large, irregularly shaped and carry a large number of remote-sensing devices as well as solar arrays for generating power. The principal active satellites in this class are ERS-2, the European Remote Sensing satellite orbiting at an altitude of 780 Km, and Topex/Poseidon, the joint French-USA altimetry satellite at an altitude of 1336 Km. These satellites require precise tracking to calibrate their altimetry observations to the surface of the oceans and ice sheets. ERS-2 carries the experimental space-borne micro-wave tracking system PRARE and a small array of laser retro-reflectors. Topex/Poseidon carries a GPS receiver, the French DORIS ground-based tracking system, and a large circular array of retro-reflectors. In addition, two of the constellation of GPS satellites at altitudes of 20000 Km carry retro-reflector arrays in order that comparisons may be made between the orbits determined using the GPS technique and those based on laser range measurements.

Because of the different heights of these satellites, their times of visibility during which range observations from a given tracking station can be attempted varies from five

minutes for the low GFZ-1, to 40 minutes for Lageos, to five hours for the high-altitude Etalon satellites. Tracking-station schedules are usually based upon the times of passes of the 'primary' satellites such as Lageos, but modern systems can rapidly switch from tracking one satellite to tracking another to maximize their operational efficiency.

## 1.3 The Etalon Satellites

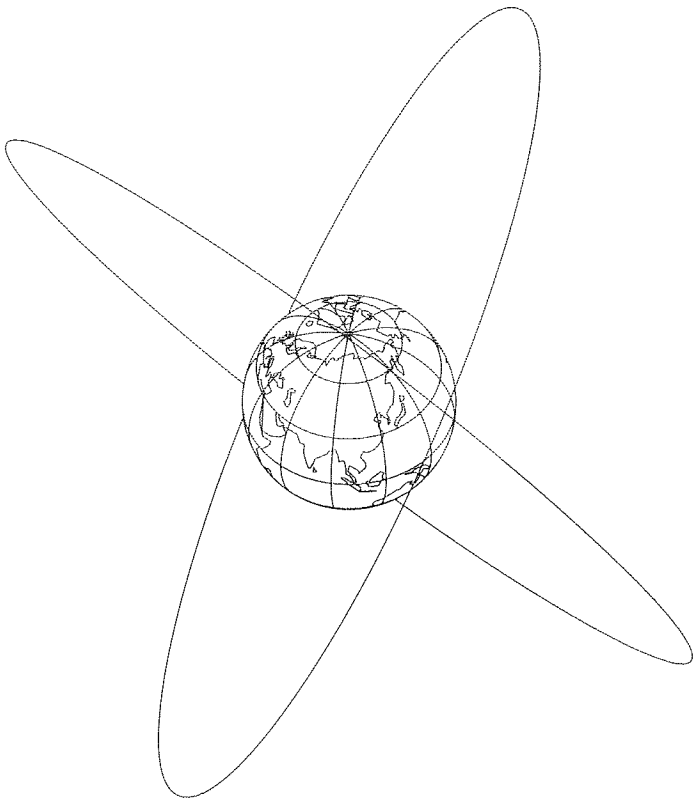

Figure 1.3: The Orbits of the Etalon Satellites.

We now consider in more detail the characteristics of the satellites whose laser range observations are a subject of this study. The two Etalon geodetic satellites were launched on 1989 January 10 and 1989 May 31 into near circular ($e \sim 0.001$) orbits at heights of 19000 km with orbital periods of 675 minutes. Each satellite was launched along with two vehicles of the Soviet Glonass Navigation system, these active satellites being rapidly moved away in orbital longitude from the inert Etalons. The orbits are inclined to the Earth's equator by approximately 65 degrees, and the orbital planes are separated by

120 degrees in longitude. The orbital configuration is shown to scale in Figure 1.3

The Etalon mission objectives and details of the satellites were announced to the SLR community by the then Astronomical Council of the USSR Academy of Sciences in the report 'The Programme of the Use of Passive Spacecraft for the Solution of Fundamental and Applied Problems in Geodesy, Geodynamics and Geophysics' [3]. The broad mission objectives were stated to be the construction of a high precision global geocentric coordinate system and corresponding evaluation of Earth rotation parameters, measurement of trans-continental baselines from pseudo-simultaneous tracking, determination of and detection of possible variation in low order terms in the Earth's gravity field, and the determination of a precise value of the product of the gravitational constant with the mass of the Moon. To encourage the international community to track these satellites in a systematic way, an international tracking campaign was announced at the 1992 May meeting of the SLR Subcommission of the International Coordination of Space Techniques for Geodesy and Geodynamics (CSTG), held during the Eighth International Workshop on Laser Ranging Instrumentation in Annapolis, Maryland. The aim of the campaign was to provide a robust data set for analysis groups to begin work using both dynamical and geometric techniques, by providing the widest possible sampling of the Etalon orbits and supporting rapid data availability. The campaign began on 1992 June 1, and about half of the global network of stations began routine tracking.

We have carried out analyses of Etalon data obtained during a 2.5 year period from the start of that campaign with the specific goal of testing the value of such data against the stated objectives of the mission.

## 1.4 Outline of Research

In this section, we give a very brief overview of the content of each chapter of the thesis, in order to describe the overall development of the work.

### 1.4.1 Chapter 2

In Chapter 2 we discuss the work carried out to allow routine, rapid extraction of fully-calibrated range normal points from the raw observations obtained at a tracking station.

We fit a computed orbit to the observations obtained during a satellite pass, and use this orbit as a smoothing function from which to calculate the set of normal points. We apply a statistical test to the residuals from this function to test for the presence of systematic trends in the residuals.

### 1.4.2 Chapter 3

In Chapter 3 we consider in more detail the process of laser ranging at a single-photon level of return, with particular emphasis on a study of the influence of the shape of the satellite on the measurement of its range. We develop a model to represent the observations by convolution of the responses of the various components in the system, and use this model to derive centre-of-mass corrections appropriate to systems with different measurement precision and for different levels of return.

### 1.4.3 Chapter 4

In Chapter 4 we discuss the computer package developed partly by the author to analyse SLR observations. During the course of the current study, we have carried out modifications and improvements to the package, and these are discussed in detail.

### 1.4.4 Chapter 5

In Chapter 5 we begin our analysis of SLR observations of the high-altitude Etalon geodetic satellites. Following a preliminary study of a few month's observations, we decide to carry out a fit of a 2.5 year continuous orbit to range data from the global network of stations, to study the long-term stability of the reference frame defined by the deduced coordinates of the tracking stations. We use the range residuals from the long-arc solutions to infer corrections to the mean orbital elements over short time intervals, with a view to identifying deficiencies in the force model, and to compute series of residual along-track accelerations.

### 1.4.5 Chapter 6

In Chapter 6 we use the residual along-track acceleration and eccentricity series in a detailed study of thermal force perturbations on the satellites, and compare the results with those from Lageos. We particularly investigate the effects of the cooling of the satellites during eclipse periods.

### 1.4.6 Chapter 7

In Chapter 7 we use the Etalon observations to derive corrections to Earth rotation parameters and station coordinates, and attempt to solve for corrections to selected terms in the expansion of the gravity field. We discuss whether we are able to detect temporal changes in the gravity field, and whether the analysis leads to a significant correction or verification of the adopted value of the product of the mass of the Moon with the universal gravitational constant.

### 1.4.7 Chapter 8

In Chapter 8 we summarize the main results of the work, and point out areas that should lead to some interesting future work.

# Chapter 2

# Pre-processing of Laser Ranging Observations.

## 2.1 Introduction

The observations obtained by a laser ranging station must be processed to extract the satellite distance measurements from noise events and to apply a calibration correction to refer those measurements to the system datum point. The observations are then communicated to the laser ranging community. Until September 1990 the procedures for data transmission were that a 'quicklook' sample of some 50 range measurements from each pass were rapidly communicated by telex and later by e-mail to the agencies responsible for producing predictions for the tracking stations. However, the 'full-rate' observations were accumulated for a calendar month and then sent on magnetic tape to NASA's Crustal Dynamics Data Information System (CDDIS), where data from the world-wide network of stations were merged and sorted into time order for later distribution on magnetic tape to the analysis community. This process resulted in a delay of some seven months from the time that the observations were obtained until the time that they were available to the analysis community.

In preparation for the launch in 1991 of the European Space Agency's applications satellite ERS-1, it became more urgent to make the observations available to the analysis community in support of the altimeter data obtained by the satellite. The principal precise tracking system that was planned for ERS-1 was SLR, and in fact the exper-

imental tracking system named PRARE (Precise Range and Range Rate Experiment) failed shortly after launch. Further, the then anticipated US/French altimetry satellite TOPEX/POSEIDON would also require intensive SLR tracking, to complement and help calibrate the on-board GPS and DORIS tracking equipment. These were some of the factors that provided the impetus for the stations to work towards computing on-site normal points for transmission rapidly either to NASA's Crustal Dynamics Data Information System (CDDIS) in Washington or to the European Data Centre (EDC) in Munich, from which centres high quality data would be available to analysts within a day of the observations being carried out.

Normal points are designed to compact the large number of individual range measurements made during a satellite pass into a few 'average' ranges, which contain the same information as the original raw data. The normal points have higher precision than the raw data through reduction of the random scatter inherent in the observations. At the Fifth International Laser Ranging Instrumentation Workshop held at Herstmonceux in 1984 an algorithm [4] to compute normal points was agreed by the laser ranging community, and it was proposed that laser range normal points should be formed by the stations shortly after each satellite pass and transmitted as quicklook data. This proposal was not immediately implemented however, and it was not until after the final version of the quicklook normal point format was agreed by the SLR Subcommission of the CSTG and published in the April 1990 Satellite Laser Ranging Newsletter [5] that normal points came into routine use for rapid transmission of observations to the data centres.

In order to pre-process the raw observations and form normal points, we have to carry out two stages; (a) fitting a smoothing function to the observational range differences from a predicted orbit and subtracting the function in order to form a flat track of residuals, and (b) rejecting noise and outliers and forming the mean values of the accepted residuals in bins spread through the pass. The values of the smoothing function and the predicted orbit at the epoch of an actual observation nearest the mean epoch of the bin are then added to the mean value of the residuals in the bin. The resulting normal points are then virtually independent of both the smoothing function and of the predicted orbit.

In this chapter we discuss the computation of the smoothing function, and apply a statistical test to check that the post-solution set of range residuals is free of systematic

trends.

## 2.2 Development of the Smoothing Function.

During the observation of a satellite pass, differences from the predicted range are computed for all events detected within the range gate and displayed in realtime; true satellite returns appearing as a continuous track of points among the randomly distributed noise points. Because of the appearance of this set of correlated range residuals, we use the term 'track' in this context throughout this document. An example of such a plot is given in Figure 2.1, which shows a pass of Lageos-1. Several parallel tracks are seen in the plot; these result from an experimental situation whereby a 'train' of laser pulses is transmitted each time the laser fires. The separation in time of the individual pulses from one another gives rise to the multiple tracks, since the range residuals are calculated with respect to the first pulse in the train. The rejection of gross noise events is carried out visually using the plot, and the subsequent set of satellite range measurements and some noise events are passed to the next stage of processing.

There are two ways to form the smoothing function. The first and simplest method is to compute and fit a high-order ($\geq 10^{th}$) polynomial to the range residuals. The second is to fit an orbital arc to the observed range measurements. The advantage of the polynomial method is that it does not require any orbital information, but the disadvantages are that the fit of the polynomial can become corrupted in the presence of noise, and also that the results of the fitting process give no information on the accuracy of the original prediction of the position of the satellite. The disadvantage of the orbital fit method is that it requires a file of predicted coordinates of the satellite in order to compare with the observations. However, the main advantage is that the results of the fitting process can be used to improve subsequent predictions, which is an important consideration. Thus the alternative of an arbitrary polynomial for the smoothing function was not adopted.

To carry out the fit of the predicted orbit to the range observations, we express orbital corrections as along-track, across-track and radial displacements to the predicted position. Such corrections are then readily applied to the geocentric orbit during the solution iteration process, and the derived along-track correction can be expressed as an

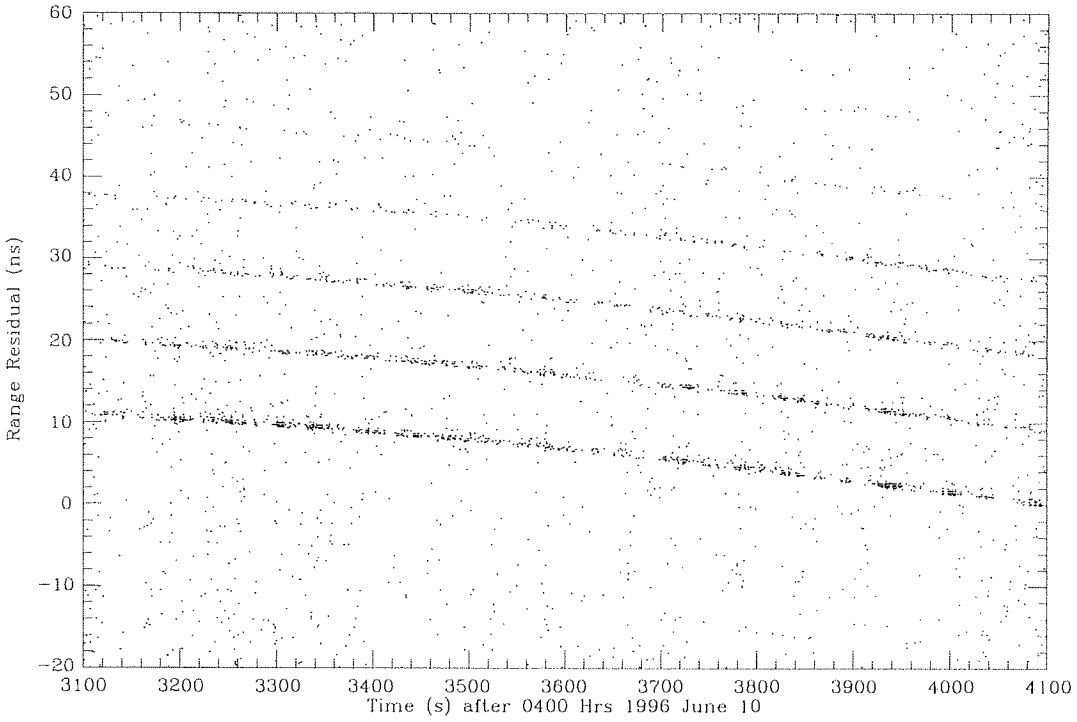


Figure 2.1: Observations of Lageos - comparison of measured and predicted ranges

orbital time-bias for improving subsequent predictions. During the prediction process an orbit in the form of geocentric rectangular satellite coordinates and velocities at 1-minute intervals of time and in units of Mm and Mm/day, is computed by numerical integration of the equations of motion, using so-called Inter-Range Vectors for the initial conditions [6]. For each observational epoch, we use 8th order Lagrangean interpolation to compute the instantaneous position $\mathbf{r}$ and velocity $\mathbf{v}$ of the satellite. Let $\mathbf{r}$ = (x,y,z), and $\mathbf{v} = (\dot{x}, \dot{y}, \dot{z})$, and let the magnitudes of these vectors be $r$ and $v$ respectively. The reference frame used is the true equator and mean equinox at 0hrs UT of the epoch of the IRVs, [6]. At the observational epoch, we compute the coordinates of the observing station in the same reference frame. Let the station coordinates be $\mathbf{s} = (x_s, y_s, z_s)$. Then the predicted topocentric coordinates of the satellite are

$$x_T = x - x_s, \quad y_T = y - y_s, \quad z_T = z - z_s \quad ,$$

and the predicted range is the magnitude of this topocentric vector. We thus form the

difference of the observed from the predicted range, and in order to solve for corrections to the predicted orbit we set up the following observation equation for solution by the method of least-squares.

$$\frac{\partial R}{\partial \Delta T}\Delta T + \frac{\partial R}{\partial \Delta Q}\Delta Q + \frac{\partial R}{\partial \Delta r}\Delta r = R_{obs} - R_{calc} + \nu, \tag{2.1}$$

where $\Delta T$ is the time-bias, $\Delta Q$ is the across-track displacement and $\Delta r$ is the radial displacement. $\nu$ is the least squares residual that we wish to minimise by adjusting our initial estimates of the three displacements.

To form the observation equation (2.1), we require partial derivatives of range with respect to the along-track, across-track and radial components of the displacement of the predicted orbit.

### 2.2.1 Partial Derivatives.

For an along-track displacement corresponding to a time-bias of $\Delta$T, the displaced range R is given by

$$R^2 = (x + \dot{x}\Delta T - x_s)^2 + (y + \dot{y}\Delta T - y_s)^2 + (z + \dot{z}\Delta T - z_s)^2.$$

Then

$$R\frac{\partial R}{\partial \Delta T} = \dot{x}(x + \dot{x}\Delta T - x_s) + \dot{y}(y + \dot{y}\Delta T - y_s) + \dot{z}(z + \dot{z}\Delta T - z_s),$$

or approximately

$$\frac{\partial R}{\partial \Delta T} = (\dot{x}x_T + \dot{y}y_T + \dot{z}z_T)/R$$

For an across-track displacement of $\Delta$ Q, we have that the across-track direction is

$$\frac{\mathbf{r} \times \mathbf{v}}{\mathbf{r} \cdot \mathbf{v}} = (l, m, n) \qquad \text{, say.}$$

So,

$$l = (y\dot{z} - z\dot{y})/rv$$

$$m = (z\dot{x} - x\dot{z})/rv$$

$$n = (x\dot{y} - y\dot{x})/rv$$

So the displaced range $R$ is given by

$$R^2 = (x + l\Delta Q - x_s)^2 + (y + m\Delta Q - y_s)^2 + (z + n\Delta Q - z_s)^2$$

So,

$$R\frac{\partial R}{\partial \Delta Q} = l(x + l\Delta Q - x_s) + m(y + m\Delta Q - y_s) + n(z + n\Delta Q - z_s)),$$

or approximately

$$\frac{\partial R}{\partial \Delta Q} = (l\,x_T + m\,y_T + n\,z_T)/R$$

For a radial displacement of $\Delta r$, the displaced coordinates of the satellite are $x + x\Delta r/r$, etc. So the displaced range $R$ is given by

$$R^2 = (x + \frac{x\Delta r}{r} - x_s)^2 + (y + \frac{y\Delta r}{r} - y_s)^2 + (z + \frac{z\Delta r}{r} - z_s)^2$$

Then as before we calculate the approximate partial derivative

$$\frac{\partial R}{\partial \Delta r} = (x\,x_T + y\,y_T + z\,z_T)/(rR)$$

### 2.2.2 Least-squares Adjustment.

For each observation obtained during the pass, we now form the observation equation (2.1). If there are $n$ observations, and we are solving for corrections to say $k$ parameters, we may write this system of equations in matrix form as

$$\mathbf{Ax} = \mathbf{b} + \mathbf{v}, \tag{2.2}$$

where

| | | | |
|---|---|---|---|
| $\mathbf{A}$ | : | $(n \times k)$ | matrix of obs. equation coefficients (partial derivatives) |
| $\mathbf{x}$ | : | $(k \times 1)$ | vector of corrections to initial estimates of the parameters |
| $\mathbf{b}$ | : | $(n \times 1)$ | vector of $R_{obs} - R_{calc}$ values |
| $\mathbf{v}$ | : | $(n \times 1)$ | vector of residuals $\nu_i$ |

If we wish to weight the observation equations, we multiply each one by the square root of the required weight $w$.

The weights are defined to be the reciprocal of the observational standard error squared. That is the $(n \times n)$ weight matrix $W$ is

$$\mathbf{W} = \begin{pmatrix} \frac{1}{\sigma_1^2} & 0 & 0 & \dots & 0 \\ 0 & \frac{1}{\sigma_2^2} & & & \\ \vdots & & \ddots & & \\ 0 & & & & \frac{1}{\sigma_n^2} \end{pmatrix}$$

So equation (2.2) becomes

$$\mathbf{W}^{\frac{1}{2}}\mathbf{A}\mathbf{x} = \mathbf{W}^{\frac{1}{2}}\mathbf{b} + \mathbf{W}^{\frac{1}{2}}\mathbf{v} \tag{2.3}$$

In the present situation, all the observations are of equal weight since only one observing station is involved, and we may take the weight matrix $\mathbf{W}$ to be the unit matrix.

### 2.2.3 Solutions

The normal equations are formed from the observation equations, and the system solved by Choleski triangular decomposition of the normal matrix. We initially carried out solutions for the parameters $\Delta T$, $\Delta Q$, and $\Delta r$. In practice it was found that the across-track correction was always highly correlated with the radial correction, with correlation coefficient $\geq 0.99$, and in many cases the solution was indeterminate. Hence both could not be solved-for, and so it was decided to suppress the solution for across-track, and solve for a radial correction only, which would thus also absorb any across-track error. It was also found that simple constant along-track and radial corrections to the predicted orbit did not in general absorb all the error in the orbits, and that the set of parameters to be determined for a particular pass should be selected from along-track and radial displacements and their time rates of change and accelerations. We denote these parameters $T, \dot{T}, \ddot{T}, R, \dot{R}, \ddot{R}$. The partial derivatives of range with respect to the rates of change and accelerations of these parameters were formed from those of the constant terms by multiplication by $t$ and $t^2$, where time $t$ is the epoch of each observation relative to the mid-time of the pass. Such a definition for the origin of $t$ is optimum in reducing correlations between the unknowns.

We found that it was necessary to solve for only three or four of the possible six parameters, but they were not always the same three or four parameters, and so a trial and error approach using all six was needed. Initially a scheme was devised to automatically check for very high (>0.999) correlations among the four unknowns $\dot{T}, \ddot{T}, \dot{R}, \ddot{R}$, and to suppress any one or two of them in order to obtain a determinate solution, consistent with obtaining a flat track of residuals. However experience showed that the values determined for these four parameters were always quite small, of the order of 0.1 ms/minute for $\dot{T}$ and 1.0 cm/minute for $\dot{R}$, and of similar magnitude for the accelerations. We thus imposed a-

priori standard errors of these magnitudes upon the 4 parameters as follows, and allowed the program to solve for all six unknowns.

### 2.2.4 Application of *a-priori* standard errors

Suppose we know *a-priori* that the value of a particular parameter $x_j$ from the set of parameters $\mathbf{x}$ is, within the standard error $\sigma$,

$$x_j = c \pm \sigma$$

Then we have an additional observation equation

$$\frac{1}{\sigma} x_j = c$$

Now we can write the normal equations

$$\mathbf{A}^T\mathbf{W}\mathbf{A}\mathbf{x} = \mathbf{A}^T\mathbf{W}\mathbf{b},$$

or

$$\mathbf{N}\mathbf{x} = \mathbf{d},$$

where $\mathbf{N}$ is the $(n \times n)$ normal matrix. Then the contribution of the additional observation equation is

$$\mathbf{N}(j,j) := \mathbf{N}(j,j) + \left(\frac{1}{\sigma}\right)^2,$$

and

$$d_j := d_j + \frac{1}{\sigma} c$$

There are no contributions to any other elements of $\mathbf{N}$ or $\mathbf{d}$

### 2.2.5 Iteration of the solution.

With the imposition of the *a-priori* standard errors on the four parameters $\dot{T}, \ddot{T}, \dot{R}, \ddot{R}$, we find that the solution is always determinate. In order to iterate the solution, at each stage we replace the predicted coordinates of the satellite by the displaced coordinates as determined from the previous solution. So for example

$$x = x + \dot{x}\Delta T + l\Delta Q + x\Delta r/r$$

and similarly for $y$ and $z$. It was found that 4 or 5 iterations were usually sufficient, where outliers of magnitude greater than $3 \times$ rms were removed at each stage.

The scheme was found to be determinate for a wide variety of satellites and pass durations and quality of predictions, and has been adopted at Herstmonceux. A version of the software coded in FORTRAN 77 and named 'SOLVE' is also in use at several European SLR stations. The deduced values of time bias are used to good effect for improving subsequent predictions, and as described by Wood and Gibbs [7], the software is used each day to generate time bias values from the quicklook observations from Herstmonceux and other SLR stations. The values over several days are represented by a low-order polynomial, and these are widely distributed to SLR stations to improve the quality of the predictions.

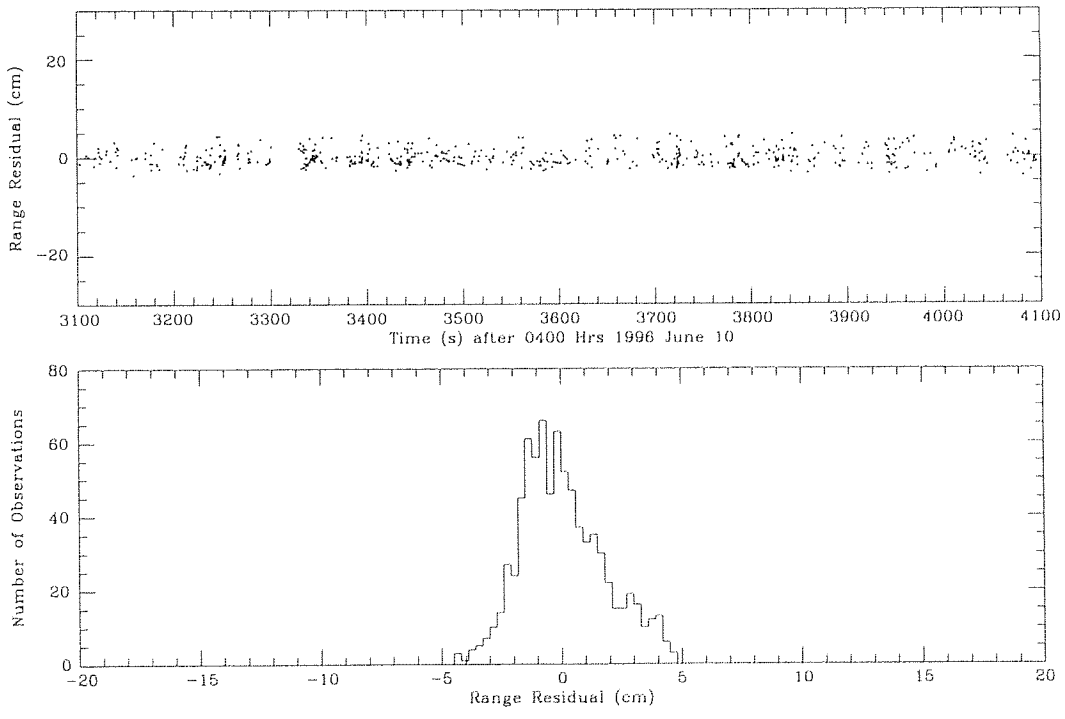


Figure 2.2: Observations of Lageos - post-solution range residuals.

A plot of the observational residuals from the pass shown in Figure 2.1 is given in Figure 2.2, where the results, expressed in one-way range in cm, are presented both in a scatter plot against time, and in histogram form. It is clear from the scatter plot that

all trends and noise events have been removed and thus these residuals are readily used to form normal points using the Herstmonceux algorithm [4]. We also use the residuals to estimate the single-shot range precision, by calculating the root-mean square of the residuals in each pass. This parameter is a good indicator of the general behaviour of the system, since any decrease in precision suggests that one or more of the components of the ranging system may be becoming defective or mal–adjusted. We also wish to examine the probability distribution of the residuals, represented by the histogram, to investigate potential satellite–dependent signatures. For these reasons, it is necessary that all trends have been removed from the residuals. Any trends left in the residuals will artificially increase the value of the rms calculated from the residuals and distort the probability distribution as defined by the histogram.

### 2.2.6 Statistical test for 'flat' track of residuals.

As a final check that the track of residuals is indeed statistically flat, and as an aid to automating the process without the need for somewhat subjective examination of the residuals scatter plot, we have introduced an Analysis Of Variance (ANOVA, [8]) test on the residuals. This statistical test is widely used in quality-control work in order to test whether a given change in procedures has had a significant effect on some series of measured parameters, such as the mean yield of a particular product, or whether the observed differences in the parameters can be wholly attributed to statistical fluctuations. We have applied this technique to check for significant differences between the means of residuals grouped into normal point bins; any differences indicate that not all trends have been removed from the residuals, and a warning is given that normal points should not be formed until the cause of the problem is traced. Another cause of signatures remaining in the residuals could be system calibration changes during a pass, and the technique helps to locate such problems. We use a Type–1, single factor ANOVA test to check whether, given the overall pass rms, we can consider that all the mean values are the same. In the jargon of ANOVA, the different *treatments* are the normal–point bins. There are $r$ treatments, with index $i$, and each bin contains $m_i$ observations. There are $n$ observations in the data set (pass), so $n = \sum_{i=1}^{r} m_i$. Each observation in the data set

can be written as

$$x_{it} = \mu + \alpha_i + \epsilon_{it}, \tag{2.4}$$

with $i = 1, \cdots r, t = 1, \cdots m_i$. Here $\mu$ is the overall mean value of the residuals, $\alpha_i$ the mean value of the residuals in bin $i$ and the $\epsilon_{it}$ is the random deviation from the $i$'th bin–mean of the $t$'th residual in bin $i$. The assumption is that the $\epsilon_{it}$ have independent, normal distributions with mean zero and common variance $\sigma_0^2$, estimated through the square of the pass rms.

If for the moment we assume that the number of observations in each bin is the same, and equal to $m$, then the sum of the squared deviations of all $n$ $(=rm)$ observations from the overall mean $\bar{x}$ can be written as $m$ times the sum of the squared deviations of the $r$ bin means from the overall mean *plus* the sum of the squared deviations of individual observations from their respective bin means, that is

$$\sum_{i=1}^{r}\sum_{t=1}^{m}(x_{it} - \bar{x})^2 = m\sum_{i=1}^{r}(x_i - \bar{x})^2 + \sum_{i=1}^{r}\sum_{t=1}^{m}(x_{it} - x_i)^2. \tag{2.5}$$

We make the null hypothesis that the bin means are all zero, which is what we want to test; i.e. that the $\alpha_i$ in equation (2.4) are all zero. If this null hypothesis is true, we have three unbiased estimates $s^2$ of the common variance $\sigma_0^2$ of the $r$ bins, obtained by dividing the sums of squares in equation (2.5) by their respective degrees of freedom. The estimates are

$$s_1^2 = \frac{1}{n-1}\sum_{i=1}^{r}\sum_{t=1}^{m}(x_{it} - \bar{x})^2 \tag{2.6}$$

$$s_2^2 = \frac{m}{r-1}\sum_{i=1}^{r}(x_i - \bar{x})^2 \tag{2.7}$$

$$s_3^2 = \frac{1}{n-r}\sum_{i=1}^{r}\sum_{t=1}^{m}(x_{it} - x_i)^2 \tag{2.8}$$

These three estimates of the common variance $\sigma_0^2$ are referred to as the 'total', 'among bins' and 'within bins' estimates respectively. The respective sums of squares in the above

three expressions are rearranged in more convenient forms for computation as follows.

$$\begin{aligned}
(1) &= \sum_{i=1}^{r}\sum_{t=1}^{m}\left(x_{it}-\bar{x}\right)^2 &&= \frac{n\sum_{i,t}x_{it}^2-\left(\sum_{i,t}x_{it}\right)^2}{n}\\
(2) &= \sum_{i=1}^{r}\left(x_i-\bar{x}\right)^2 &&= \frac{r\sum_i\left(\sum_t x_{it}\right)^2-\left(\sum_{i,t}x_{it}\right)^2}{n}\\
(3) &= (1) &&- (2)
\end{aligned}$$

Then for the more usual situation of unequal numbers of observations within each bin, say $m_i$ observations in bin $i$, equation 2.7 becomes

$$s_2^2 = \frac{1}{r-1}\sum_{i}^{r}\frac{\left(\sum_i^r x_{it}\right)^2}{m_i} - \frac{\left(\sum_{i,t}x_{it}\right)^2}{n}, \tag{2.9}$$

If the null hypothesis of equal bin means is true, then the two quantities $s_2^2$ and $s_3^2$ should be about equal, with a ratio near one, since they represent independent estimates of $\sigma_0^2$. The standard test for ratios of variances is the $F$ test (for example in Crow, Davis and Maxfield, [8]). For a given test level of significance, $\alpha$, and for the two sets of degrees of freedom $r-1$ and $n-r$, we extract from published tables the value of $F_\alpha(r-1, n-r)$. If the quotient $s_2^2/s_3^2$ exceeds the tabular value , then we reject the null hypothesis at significance level $\alpha$, that is we cannot assume that the track of residuals is flat. We have chosen a level of significance, $\alpha$, of 5%, that is we only expect incorrectly to make such a decision 5% of the time.

## 2.3 Conclusion

We have described our method of preprocessing laser range observations to remove noise events and to form normal points., including a test that all trends have been removed from the range residuals. In the next Chapter we discuss potential sources of bias during laser ranging operations which may lead to a track of residuals showing systematic trends, and thus failing such a test. We consider return-level effects upon the measurements and effects due to the extended nature of the retro-reflector arrays of the satellites.

# Chapter 3

# Systematic Effects in Laser Range Measurements

## 3.1 Introduction.

With the continuing drive to improve the precision of laser ranging systems, it is important to understand the potential for systematic bias within any of the system parameters, as we do not wish to generate highly precise data which are not of comparable accuracy. In this chapter we discuss the work that has been carried out to understand such effects over a variety of system parameters such as return energy level and for a variety of range targets including the flat calibration board and the geodetic satellites Lageos and Etalon. We develop numerical models of expected range distributions, and compare them to the observations, and in particular we derive for the Lageos and Etalon satellites values of the centre of mass corrections appropriate for both single–photon and multi-photon ranging systems. For Lageos, the values are compared to the published ground–test results which were derived using only the multi–photon ranging techniques. For the Etalon satellites, no such ground–tests were carried out, so this work is required in order to derive appropriate centre of mass corrections.

We first give a general outline of the factors that need to be considered. The principle components that affect the precision of a ranging system are

- the laser pulse width;

- the detection of the outgoing laser pulse, using a photo-diode detector (the start diode);
- the characteristics of the reflection at the satellite;
- the detection of the returning photon or pulse of photons;
- the instrument used to measure the time interval.

All of these have characteristics which cause a random variation or jitter of the measured range about its actual value. These components all have their own intrinsic distributions, e.g., the distribution of energy within the laser pulse and the distribution of retro-reflectors on a satellite, and the final distribution of measured ranges is a convolution of the contributing distributions. These distributions are described by their full-width-half-maximum values (FWHM) or by their RMS variation from a mean, or in the case of a Gaussian distribution by the standard deviation $\sigma$. For a Gaussian distribution, FWHM equals 2.35 $\times\sigma$, and RMS is sufficiently close to $\sigma$ that we do not distinguish them.

For ranging to a calibration target board all of these factors except the satellite will affect the data distribution, and we refer to this combined effect as the ranging system response function. The RMS of this distribution is the system precision.

The units used are either nanoseconds (ns) or picoseconds (ps) for two-way time of flight, or mm for one-way range. The conversion is

$$1ns = 1000ps = 150mm$$

Laser pulse width is usually measured in time units (the time taken for it to pass a given point) rather than in length units, as it is a two-way factor; its effect on range is half the pulse width.

What is finally seen in the data distribution depends strongly on the type of detector used. For the MCP systems, the return level is typically of about 10 photons, the detector triggering on the leading edge of the return pulse, which means that information on the shape of the distribution is mainly lost. The shape of the resulting data distribution will therefore depend mainly on the consistency of hardware settings of trigger levels. However, an avalanche photo-diode, for example a SPAD detector, triggers on the first

photon that it successfully detects. So the data distribution shape will depend on the return level; if only single photons are returning in each pulse, then after a large number of such pulses are detected the shape of the data distribution will represent the average pulse-shape. We then have to make a choice in software about which point within the distribution we consider as the reference point. The advantage of the single-photon system is therefore a greater control over the measurement process, but a deep understanding of these various subtle effects is needed.

## 3.2 Satellite Observations

The range residuals from the fitted smoothing function, generated as described in Chapter 2, are free from orbital errors which might lead to systematic trends. The residuals thus contain purely quantitative information about the precision of the process of making range measurements, namely the jitter imposed by the time–interval counter and the start diode, by the finite pulsewidth of the laser, by the SPAD detector and potentially by the extended nature of the laser retro array of the particular satellite concerned. The range residuals from each pass are used to form histograms with respect to range residual, expressed in cm. As a final stage in eliminating outliers, and in order to estimate the pass-mean and rms value, a Gaussian distribution is fitted by least–squares to the histogram by adjustment of initial estimates of the mean $\mu$ and standard deviation $\sigma$.

Figure 3.1 shows a series of plots in histogram form of range residuals from the target board and from most of the spherical laser satellites, and including Topex/Poseidon, in increasing order of satellite size. The curves in each plot are the fitted Gaussian distributions. There is a clear broadening of the distributions with increasing satellite size, such that the single–shot precision decreases from about 10mm for target board and ERS–1 ranging, through 17mm for Lageos, to 45mm for Etalon. Decreasing precision is accompanied by poorer fits to the Gaussian distributions, with the Etalon data being particularly badly approximated.

It is useful to compare these results with some observations taken from a NASA ranging system, working at multi–photon levels and using an MCP detector. In figure 3.2 we show a histogram of range residuals of Etalon-I obtained by the MOBLAS–4

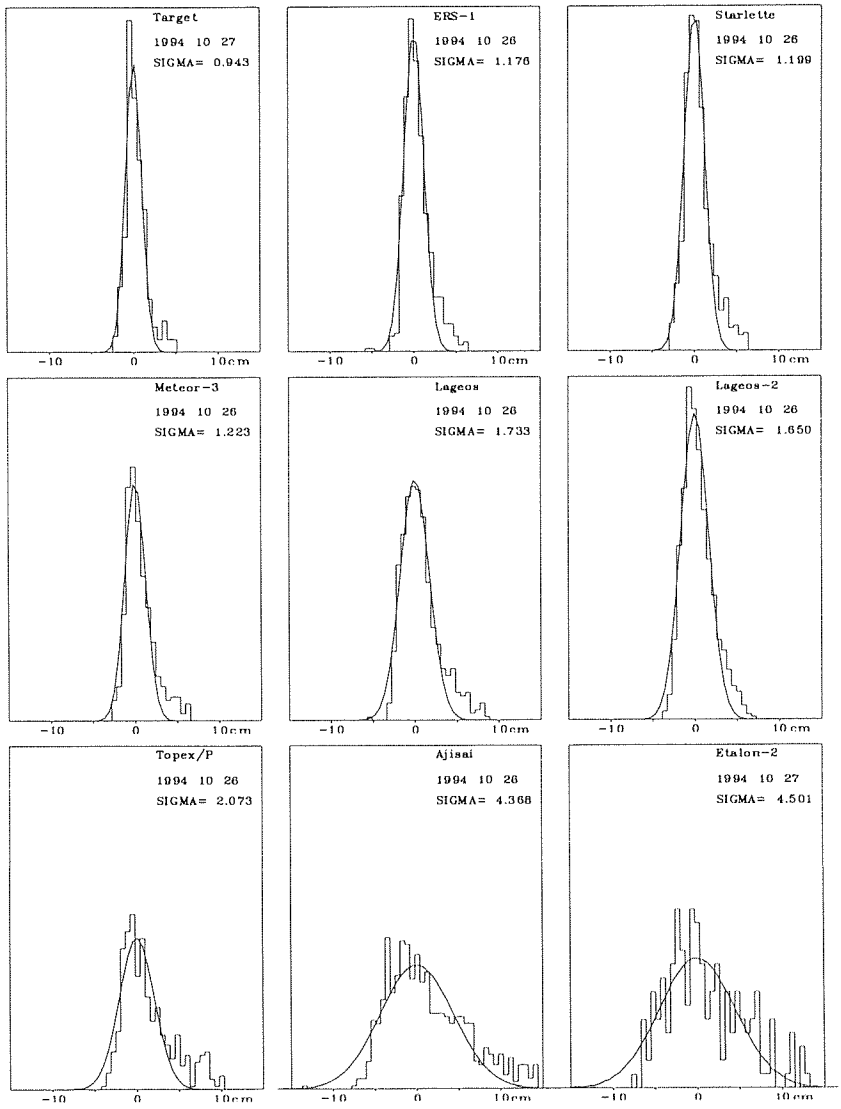


Figure 3.1: Distribution of Range Residuals from Herstmonceux

system at Monument Peak, California on 1992 Dec 17.

The distribution is clearly different from those of the Herstmonceux system, showing little of the broadening present in that data. Consequently the range precision from the Monument Peak system is nearly the same for all satellites, and significantly better than that obtained at Herstmonceux. Clearly this effect requires investigation, particularly as it appears possible that the centre of mass corrections for these satellites might be ranging system dependent. At the start of the current investigation, some doubt was cast by the ranging community on the reality of the effects shown in Figure 3.1, the belief being expressed that the effects may be due to poor alignment within the single–photon ranging systems. We set out here the development of the argument to contradict

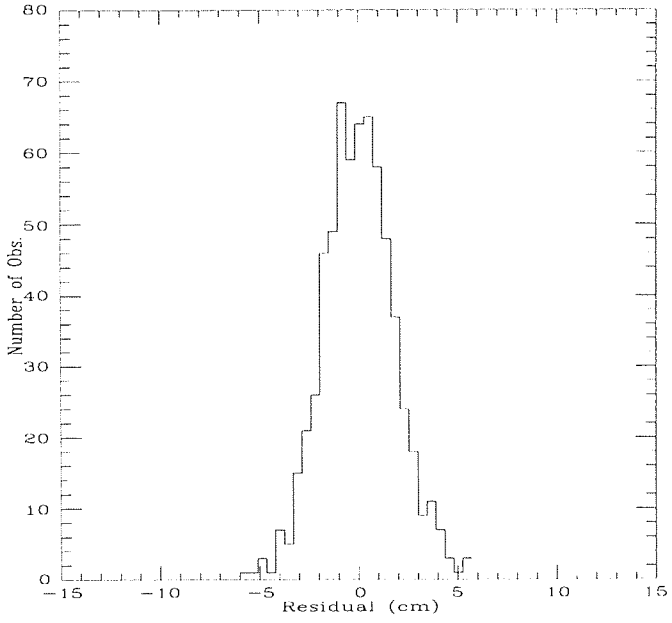


Figure 3.2: Distribution of Range Residuals of Etalon-I from Monument Peak

this explanation by first modelling the ranging system response and then the expected effects of the satellite. An early version of these results was presented at the Eighth International Workshop on Laser Ranging Instrumentation held at Annapolis, MD in May 1992 [9].

## 3.3 Ranging–System Response

A ranging system response is represented by the observed distribution of range measurements to a flat target–board, provided that a single–photon return level is maintained. A typical set of results from the Herstmonceux system is shown in histogram form in Figure 3.3(a), where a large number of observations was obtained during a ranging session of some 20 minutes. The range measurements have been converted to one–way range in mm, and expressed with respect to an arbitrary origin. The derived single–shot precision is 11mm, and the distribution is seen to be significantly skewed towards long ranges, with significant numbers of observations at distances up to 150mm from the distribution peak.

In order to examine this distribution, we develop a model of the system signature represented by these observations by estimating the probability distributions for the

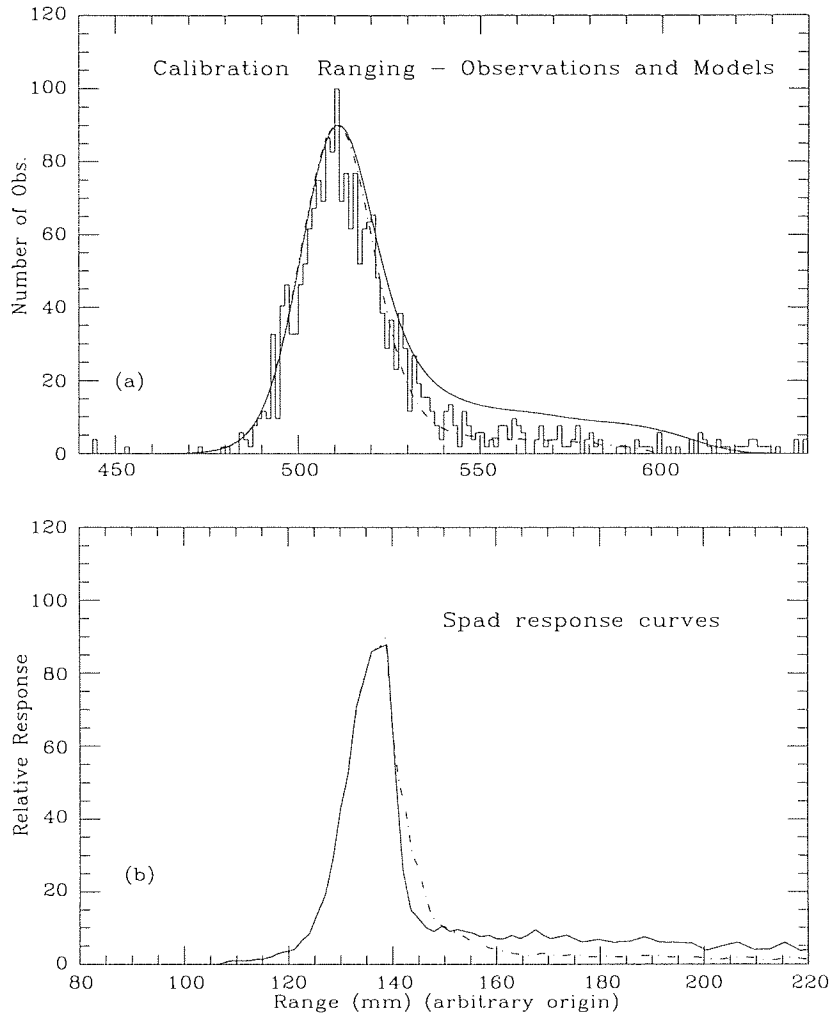


Figure 3.3: Distribution of Calibration Range Residuals and Models.

components of the system, that is distribution functions that describe statistically the 'jitter' contributed to a given measurement by a given component. To represent the response of the SPAD we digitised the response curve of the RGO SPAD provided by the supplier (Prochazka [10]). To represent the density distribution of the laser pulse which closely approximates a Gaussian function of estimated FWHM 120ps, we digitized and scaled a streak camera image of a mode–locked Yag laser pulse [11]. We assume Gaussian responses of FWHM 47ps and 64ps for the Stanford interval timer and start diode respectively. (these figures have been measured for the Herstmonceux system). We expect the observed distribution of target board ranges to be closely approximated by a response function derived by convolution of these four elements, which is carried out as follows. If we represent a particular response curve by a set of values $y(i), i = 0, \ldots, n$

and convolve it with a second distribution represented by $z(i), i = 0, \ldots, n$, then the resulting convolved distribution $c(k), k = 0, \ldots, n$ is obtained from

$$c(k) = \sum_{i=0}^{m} z(i)y(k-i), \tag{3.1}$$

where in generating a given element of the vector $c$ the summation limit $m$ is large enough that all non-zero elements of the vectors $y$ and $z$ are considered.

Using this equation we numerically convolve the distributions to form a model of the expected whole–system single–photon response, which may be directly compared to the observed distribution. This model is plotted as the full line in figure 3.3(a), shown as an envelope about the observed distribution of target–board ranges. We have applied a scaling factor to the model function values to achieve the best fit to the data, since the response curves have arbitrary amplitudes.

The model represents the data well, including the long tail, except that it clearly over–estimates the amplitude of the tail of the distribution. To address this point, and since the amplitude of the tail in the distribution is a result of that in our model of the SPAD response, we modified the original distribution of the SPAD response and repeated the convolution, again comparing the result to the observed distribution. We iterrated this process until reasonable agreement was found between the model and the observations. The resulting model is also shown in Figure 3.3(a), as a dotted line envelope, where the agreement with the data is now satisfactory. For the subsequent computation of satellite signature models, we use this system response curve, as represented by the dotted line. We show in Figure 3.3(b) as a full line the original SPAD response measured by Prochazka [10], and as a dotted line the modified response as implied by our data.

## 3.4 Satellite Signatures

### 3.4.1 Preliminary investigation

In order to model the observed distribution of the satellite range residuals, we must convolve our system response model with a distribution function which represents the response of the satellite retro–reflector array. We shall refer to this as the satellite response function. Other terms sometimes used are impulse function or optical transfer function.

When a transmitted laser pulse illuminates a satellite, all the cube corners within some angle of the direction of motion of the pulse reflect energy back towards the transmitter. Because the individual cube corners are on the surface of a sphere, they are all at different distances from the transmitter, and the pulses reflected back to the transmitter will be displaced in time. The situation is shown in Figure 3.4, taken from NASA Technical

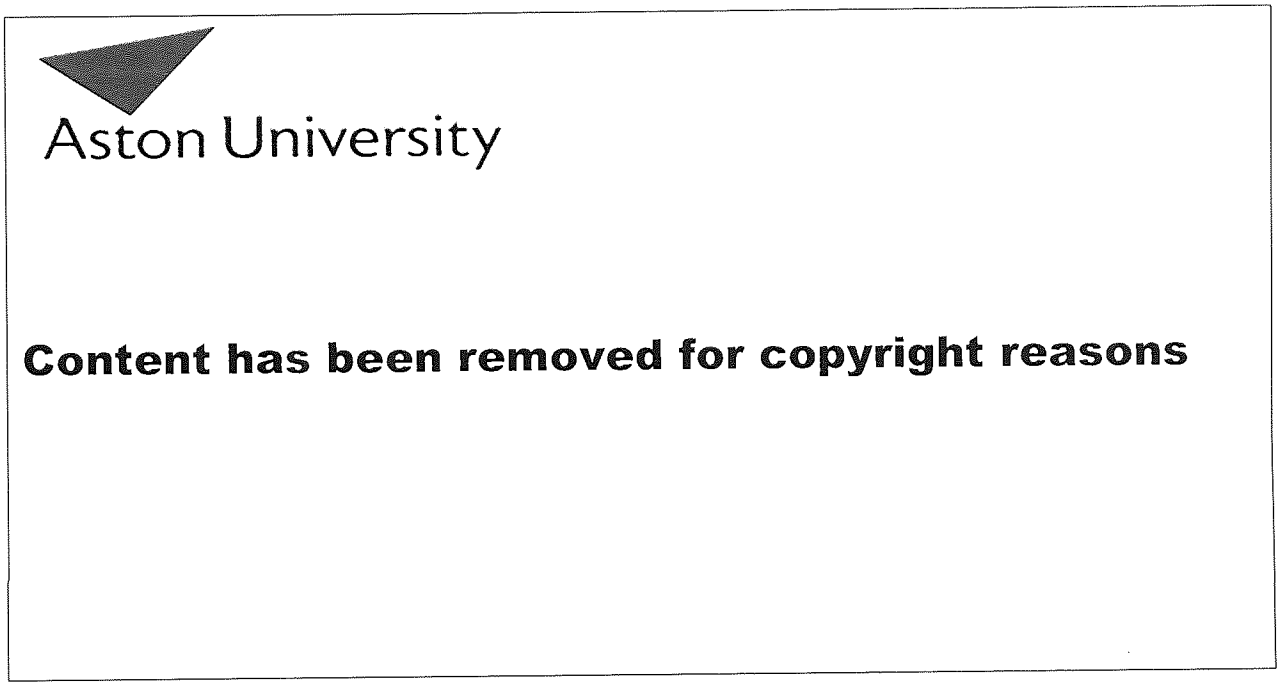


Figure 3.4: Schematic of pulse spreading by satellite retro–array

Paper 1062, 'Prelaunch Testing of the Laser Geodynamic Satellite (LAGEOS) [12].

If the return pulse, the sum of these displaced individual pulses, is then sampled at the single photon level by the detector, then on average over a large number of such observations, we would expect to obtain a range residual distribution formed by the convolution of the system response function with the satellite response function. It is pointed out in the NASA Technical Paper that in those cases where the reflected pulses overlap in time, the resultant waveform is dependent on the relative phases of the optical fields of the respective pulses, that is coherent interference may take place and distort the simple summation argument. However, for average pulse–spreading considerations, we assume that these coherent effects may be neglected and that the average reflected pulse shape can be obtained by summing of the displaced individual pulses. A preliminary experiment to use such a simple model for the satellite response was carried out using a

table of reflectivity cross sections of Lageos given as a function of distance from the centre of mass of the satellite in the NASA TP 1062 [12]. The cross section values were treated as the satellite response function, and convolved with our system response function. The resulting distribution was scaled and compared to the observed distribution of a set of range residuals. A plot of the results is shown in figure 3.5, where the agreement is fairly good. The rms of a single observation is 17mm. The estimated FWHM of the response function is 38mm, which for a Gaussian approximation converts to a standard deviation of 16mm.

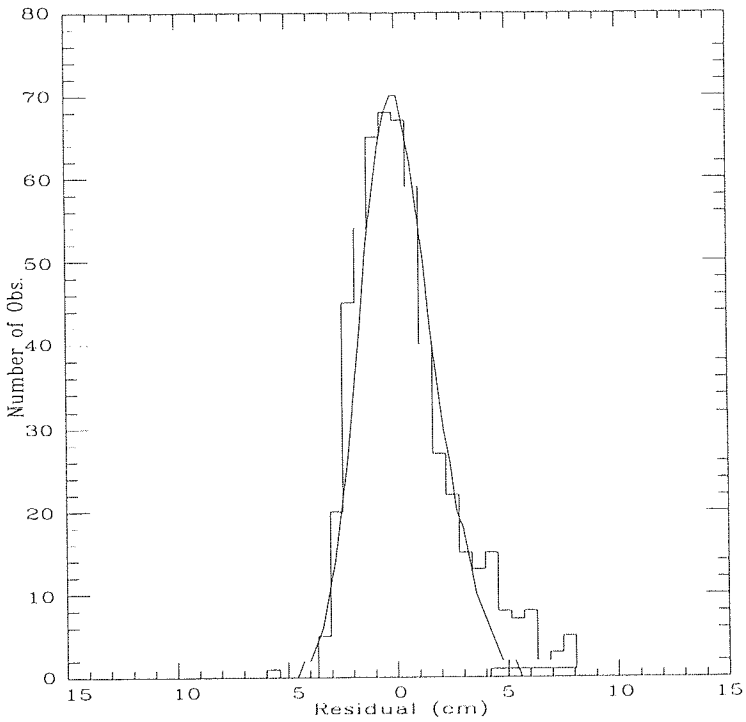


Figure 3.5: Histogram of Range Residuals of Lageos with Modelled Distribution.

Results on a similar investigation into the distribution of range residuals from the Japanese satellite Ajisai, using an empirical response function derived by Sasaki and Hashimoto [13], were presented along with the Lageos results at the Annapolis Workshop [9]. Results on the detection of satellite signatures at the Graz, Austria single–photon SLR station were also presented at that Workshop by Kirchner and Koidl [14].

### 3.4.2 Use of Analytical Response Functions.

Along with the observational evidence for detection of satellite signatures by the single–photon systems, and approximate modelling of the satellite response functions, analytical models have been developed which can be applied readily to any spherical satellite. Degnan [15] and Neubert [16] develop the response function by regarding the satellite's sphere to be quasi–continuously covered by small cube corner reflectors. We follow the work of Neubert [16], and consider Figure 3.6, which shows the basic relationships from which we calculate the distance from the centre of the satellite of the equivalent reflection plane for a given retroreflector receiving laser light at an angle of incidence of $\Phi$.

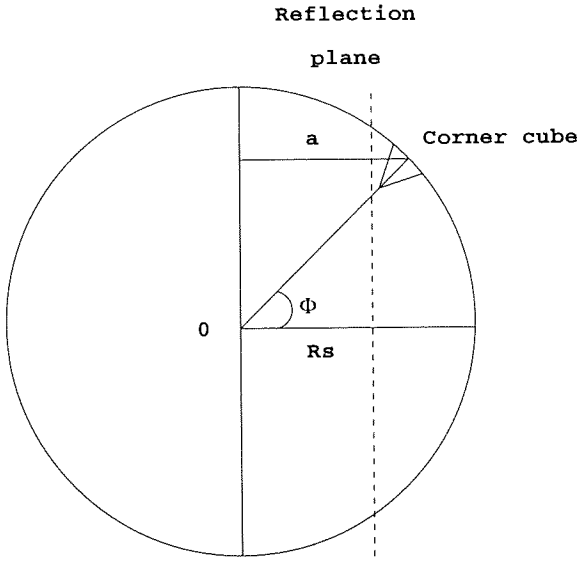


Figure 3.6: Schematic of spherical satellite and a single corner cube

In Figure 3.6, $R_s$ is the radius of the satellite, $a$ is the distance from the front face of the corner cube to the plane perpendicular to the incident laser beam, and containing the centre of the satellite, and the plane of reflection is represented by the dotted vertical line.

Now $a = R_s \cos(\Phi)$. The equivalent reflection point for a solid corner cube is given by [12]

$$\Delta R = L\sqrt{n^2 - \sin^2 \Phi}, \tag{3.2}$$

where $\Delta R$ is measured from the front face of the cube to the reflection point, $L$ is the distance from the vertex to the front–face of the cube, and $n$ is the refractive index of

the quartz. So the distance $x(\Phi)$ of the reflection plane from the centre of the satellite is

$$x(\Phi) = a - \Delta R = R_s \cos(\Phi) - L\sqrt{n^2 - \sin^2 \Phi} \tag{3.3}$$

Neubert then considers the intensity $I_\Phi$ of the reflected energy that comes from a zone of equal angle $\Phi$, and obtains

$$I_\Phi(\Phi) = \frac{1}{A}(\sin(\Phi)\eta(\Phi)), \tag{3.4}$$

where $A$ is a normalising factor, and

$$A = \int_{\Phi_c}^{0} \sin(\Phi)\eta(\Phi)\, d\Phi, \tag{3.5}$$

where $\sin(\Phi)\, d\Phi$ is the surface element on the unit sphere, and $\eta(\Phi)$ is a function describing the angular dependence of the effective reflectivity of an individual cube corner. This function has been approximated by Degnan [15] as

$$\eta(\Phi) = \left(1 - \frac{\Phi}{\Phi_c}\right)^2, \tag{3.6}$$

where the angle $\Phi_c$ is the cutoff angle of incidence; for values of $\Phi$ greater than this, no significant reflection occurs.

Neubert then expresses as a function of distance $x$ from the centre of the satellite the fraction $I_x(\Phi)$ of the reflected intensity that is contained in the small interval $\{x, x+dx\}$, by dividing $I_\Phi$ by $\frac{dx(\Phi)}{d\Phi}$.

$$I_x(\Phi) = \frac{I_\Phi(\Phi)}{x'(\Phi)} = \frac{\frac{1}{A}\eta(\Phi))}{R_s + \frac{L\cos(\Phi)}{\sqrt{n^2 - \sin^2 \Phi}}} \tag{3.7}$$

If now we compute from equation 3.7 $I_x(\Phi)$ for $\Phi$ running from zero to $\Phi_c$, and plot the results against $x(\Phi)$ from equation 3.3, we have the impulse function of the satellite as a function of distance from the centre of the satellite.

We have computed these satellite response functions for Lageos and Etalon and plotted the results in Figure 3.7, where here the x–axis gives increasing distance in mm from the front surface of the satellite, obtained by subtracting $x(\Phi)$ from the satellites' radius $R_s$. The y axis is an arbitrary amplitude. The corner cube cutoff angles $\Phi_c$ were taken

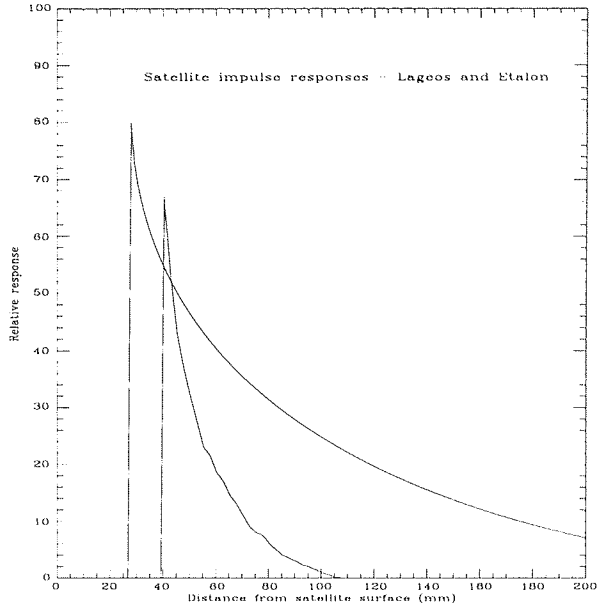


Figure 3.7: Lageos and Etalon Impulse Functions, from Neubert

as 0.75 radians for the uncoated quartz glass of Lageos [17] and 1.00 radians for the aluminium back–coated cubes of Etalon [18], and from the same references $R_s = 298.0$mm for Lageos and $R_s = 641.5$mm for Etalon.

We now use our system response model and these satellite response functions to generate theoretical probability distributions of range measurements of Lageos and Etalon. For this comparison with real observations, we choose to take the mean value of the system response as the zero–point of our system, and convolved the system about the satellite impulses with respect to that origin. (Other reference points are possible, such as the peak, and we will discuss their use later in the chapter.) We compare in Figure 3.8 the resulting theoretical distributions with those of sets of range residuals from passes of Lageos and Etalon, where the x–axis represents true distance from the satellite surface, for mean–value data processing. The observations are given in histogram form and the model is represented by the continuous line. The model distributions have been fitted to the observations in a least–squares sense by adjusting only the vertical scale of the model, and shifting the range residuals from their original mean value of near–zero. The models are seen to represent the data very closely, and emphasize in particular the long tail in the distribution of ranges from Etalon, which might have appeared to be system noise. It is interesting to note that this long tail relative to that of Lageos is due mainly to the back coating of the Etalon reflectors, whereas the Lageos reflectors are uncoated;

back coating for Etalon increases the return signal from these distant satellites, but at the expense of degrading the satellite response function.

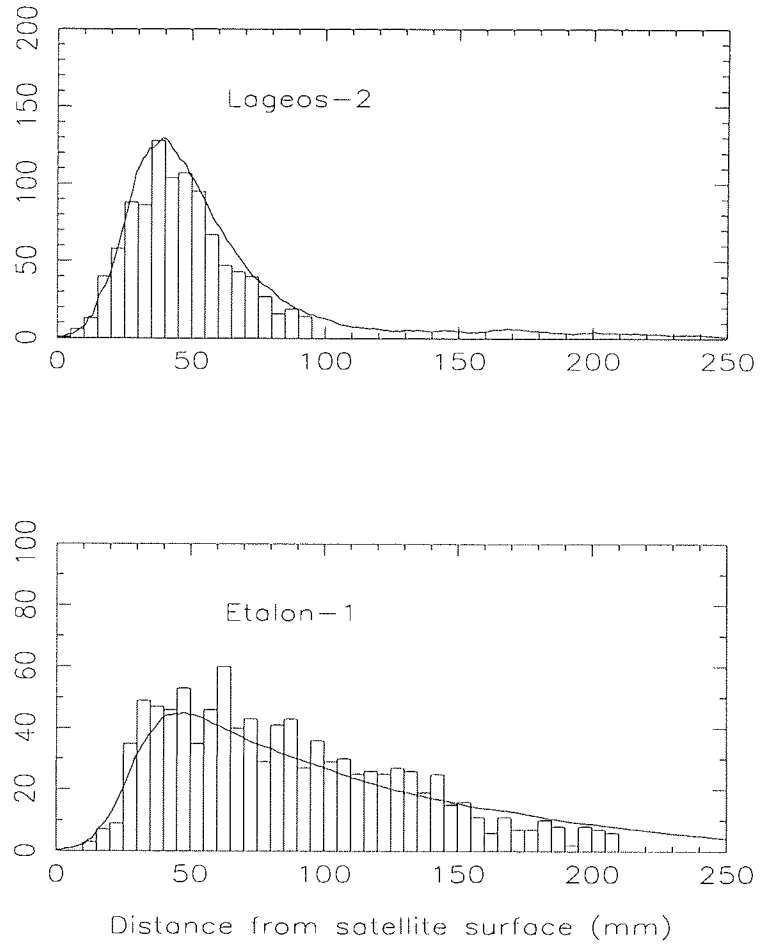


Figure 3.8: Lageos and Etalon Observational and Modelled Distributions

### 3.4.3 Centre of Mass Corrections.

We now use our models of the single–photon signatures of Lageos and Etalon to derive appropriate centres–of–mass (CoM) corrections for 3 different methods of range estimation, and for laser systems with different levels of precision. We take our system response curve, of assumed 12 mm single-shot precision, and use the smoothing algorithm derived by Sinclair [19] to estimate the peak, the mean and the leading–edge, half–maximum (LEHM) of the distribution. For each of these three estimates of the origin of the system response, we convolve it with the satellite response functions to form models of the expected distributions of satellite range observations. We again use the smoothing algo-

rithm to estimate for Lageos and Etalon the CoM corrections for mean, peak and LEHM detection.

The whole process is repeated for hypothetical systems with single–shot calibration precision 6 mm and 20 mm respectively, by altering the width of our model of the laser pulse. Shown in Tables 3.1 and 3.2 are the deduced CoM corrections for Lageos and for Etalon for each of the three systems, including the Herstmonceux results (12mm precision), for each of the processing methods.

| System | Processing | | |
|---|---|---|---|
| Precision | Peak | Mean | LEHM |
| (mm) | mm | mm | mm |
| 6 | 250 | 248 | 252 |
| 12 | 246 | 240 | 250 |
| 20 | 241 | 236 | 247 |

Table 3.1: Lageos CoM corrections.

| System | Processing | | |
|---|---|---|---|
| Precision | Peak | Mean | LEHM |
| (mm) | mm | mm | mm |
| 6 | 605 | 581 | 610 |
| 12 | 599 | 582 | 607 |
| 20 | 594 | 584 | 595 |

Table 3.2: Etalon CoM corrections.

The standard procedures currently in operation at Herstmonceux to derive a reference point from the distributions of data from both the calibration ranges and of the residuals within each normal point bin, in fact determine the peaks of the distributions by fitting Gaussian distributions as shown in figure 3.1. Therefore from Table 3.1 the appropriate CoM correction for Lageos is 246mm for our system. This is to be compared with the 251mm currently recommended for all systems in IERS Standards 1992 [20]. Other

systems operating at the single photon level typically use the mean as a reference point, and for those systems the appropriate CoM correction is about 240mm, depending on system precision. For the multi-photon systems, employing leading–edge, half–maximum detection and with precision values of about 6mm, our CoM value is 252, very close to the recommended value, which was obtained by the ground–tests of Lageos [12] and Lageos–II [21]. For Etalon, from Table 3.2, the appropriate CoM value for the Herstmonceux system is 599mm, and for the multiphoton systems is 610mm. These values are significantly different from the 558mm given in IERS Standards 1992 (McCarthy, 1992), and from the 576mm deduced by Mironov [18]. No ground–based measurements of the Etalon satellites were carried out, and we suggest that the CoM values deduced here should be used for analyses of observations of these satellites. In the subsequent analyses reported in this current work, we use the values in Table 3.2, taking account of each system's detection method (single or multi–photon) and precision, if known.

## 3.5 Multi-Photon Return Levels.

### 3.5.1 Introduction.

In this section we consider the effects for a system using a detector that detects the first photon of using a return level higher than a single photon. From the models and observations discussed in the previous Sections, is is clear that working at the single photon level of return implies that there is a limit to the precision achievable, which for a given ranging system, is set by the contribution to the error budget of the signature of the satellite. Experience at Herstmonceux shows that in fact return levels significantly higher than the single photon level are available, and that neutral density filters in the return optical path are frequently employed to maintain the single–photon regime. Now if we were to depart from this level, and not attenuate the return pulse, then photons in the leading edge of the pulse would have a greater probability of being detected, and the contribution to the error budget of the pulse–distribution would be diminished. The single–shot range precision would improve by approximately $\sqrt{n}$, where $n$ is the number of photons in the pulse. In the following, we describe experiments carried out at Herstmonceux to explore the possibility of this approach, and in particular to test

whether any significant bias will be introduced into the range observations as a result of departing from the intended single–photon level.

### 3.5.2 Target–Board Ranging.

It is difficult to measure the numbers of photons entering a detector without interfering with the precise measurement of arrival time, and so we deduce this from the average proportion of shots fired on which a return is obtained. We compute the return rate during ranging sessions by counting the number of laser shots in a given time interval, say 15 seconds. For each of these shots we check whether a noise event is detected, each of which reduces by one the effective number of laser shots. Given the number of true returns within the interval, we compute the true return rate as a percentage of the effective number of laser shots. This information is displayed to the observer in near realtime. From the observed return rate we compute the average number of photons entering the detector on each shot. Any detector has a certain probability of detecting a given event, referred to as its quantum efficiency. For a detector with quantum efficiency $q$, where $(0 < q < 1)$, we can relate the return rate to the average number $n$ of photons reaching the detector from the following consideration. The average number of photoelectrons at the detector is $qn$, and for a detection to be made we must have $qn \geq 1$. So from Poisson statistics, the probability of detecting a return may be expressed as

$$P(qn \geq 1) = 1 - P(qn = 0),$$

$$P(qn \geq 1) = 1 - \frac{e^{-(qn)}(qn)^0}{0!} = 1 - e^{-(qn)}.$$

Now expressed as a percentage return rate, we have

$$rate = (1 - e^{-(qn)}) \times 100$$

For standard calibration ranging this rate is maintained at about 10-15% by attenuation of the outgoing laser beam, and by selection from a set of neutral density (ND) filters in the receive path. For the SPAD detector at Herstmonceux, $q$=0.2, and so a return rate of 10 - 15% implies that on average 0.6 photons are entering the detector - (or 6 photons in 10 shots). For the duration of the ranging experiments the outgoing beam

was attenuated such that the highest value ND filter was required to maintain single-photon returns. A series of calibration ranges was performed at different receive levels by selection of different ND filters, such that some 12 return levels of between 1 and 1000 photons were obtained. We note that for $n$ above about 15, the observed return rate is close to 100%, so for rates $\geq$ 100%, $n$ is estimated from the known relationships between the densities of the filters. The observations at each return level were used to form iterated mean calibration values and single–shot rms precision, with rejection of outliers at 3 $\times$ rms.

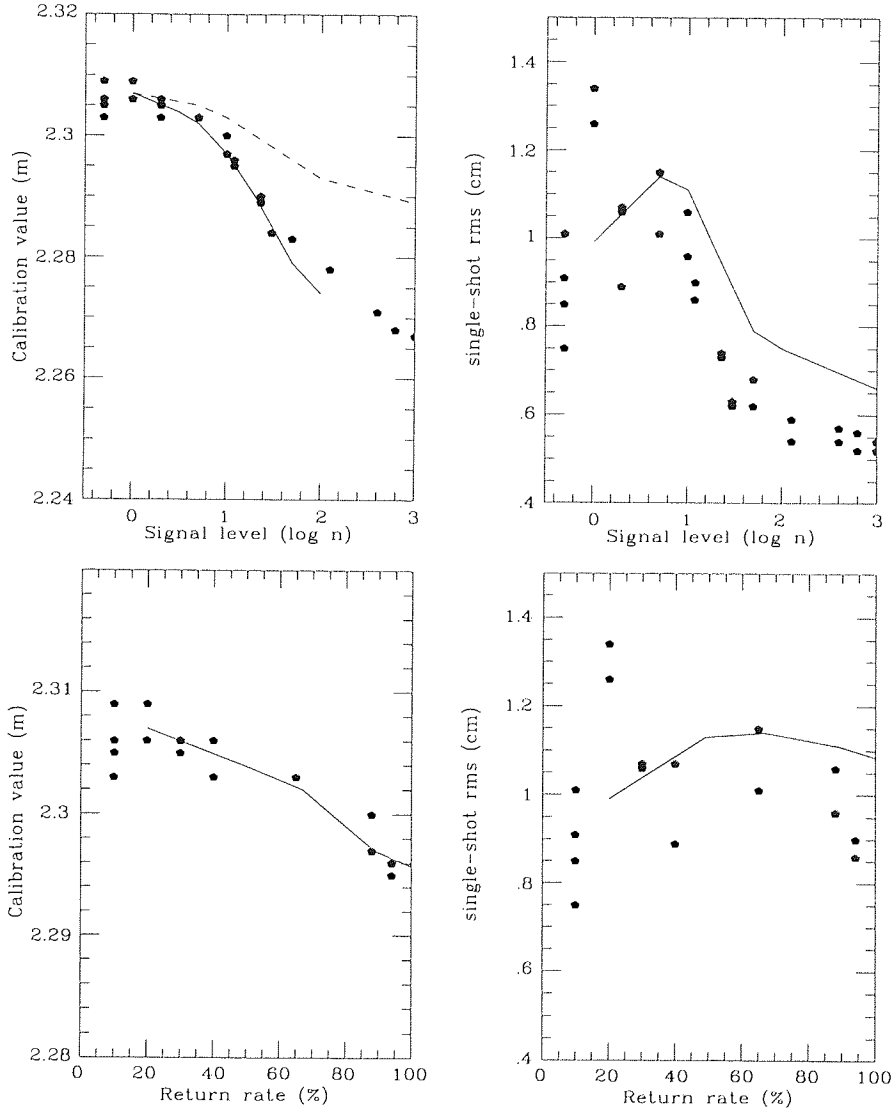


Figure 3.9: Observations and model calibration values as functions of return levels

The observed calibration and rms precision values are shown in Figure 3.9 as functions of return level, where we plot data both from the full dynamic range of the experiment as a function of $Log(n)$, and as a function of return rate (0–100 %). The observed data

are plotted as discrete points. The solid and dashed lines are theoretical modelled values, explained in the next section. For a change of return rate of from zero to 100%, it is seen that the calibration value changes by about 15 mm. The range precision changes little, with mean value about 9 mm, but with a temporary *decrease* to 13 mm at around 20%. This precision decrease has been noted consistently in the Herstmonceux data, and is also seen by Prochazka [10] in laboratory tests of the SPAD. For the results over the full range of the experiment, we see that the calibration value changes by some 40 mm, and the single-shot precision increases to about 6mm.

This observational work was carried out at Herstmonceux in collaboration with P. Gibbs, and the results were presented by the author at the Ninth International Laser Ranging Workshop in Canberra in 1994 November, and a paper by Appleby and Gibbs appeared in the proceedings of that workshop [22].

### 3.5.3 Model of Target–Board Ranging at High Return Levels.

There are two effects to be considered when modelling the range values and the distribution of data to be expected from ranging to a target at high return levels, but using a detector that detects the first returning photon. These are

1. The photon that is detected will tend to have come from the front of the returning pulse shape, rather than statistically sampling the whole of it.

2. The detector may respond differently to a pulse of several photons entering it rather than a single photon. In general the effect is to give a more rapid rise of the output pulse, leading to an earlier time being recorded for the detection of the event, and hence to a shorter measured value of the range. This is referred to as a 'timewalk' of the detector.

We first consider the effect of the detection point moving towards the front of the returning pulse. Our model of the system response closely represents the observed distribution of single–photon returns from the target board, as described in Section 3.3. We now consider this model as representing an average probability distribution of photons in a return pulse. To model the effect of $n$ photons reaching the detector, we use a random number generator to pick one 'photon' from our distribution, then record its time-location

within the distribution, and repeat the process $n$ times. We then sort this sequence of $n$ relative event times into chronological order of arrival at the detector. We model the 20% efficiency of the detector by stepping through the $n$ events in time order, at each step generating an integer random number in the range 1-5. If the random number is 1, the event is accepted (detected). If the random number is not 1, the next event is 'tested'. This whole procedure is repeated a large number of times (usually 500), and in this way we generate a large number of event times each resulting from the selection of a single photon from a series of returns containing an average of $n$ photons, and finally compute the mean time. We have plotted in Figure 3.9 these mean values as the dotted line over the full zero-1000 photon return level. We see from comparing our model to the observations that the model under-estimates by some 25 mm the total change in calibration value, and that the model tends to 'flatten out' at high return level as 'photons' are sampled from close to the leading edge of the modelled distribution.

We now add to these model values an estimate of the return-level dependent timewalk intrinsic to the SPAD detector, by using the results of Prochazka [10] who measured the timewalk over an input level of between zero and 100 photons. The results of this complete model are shown as the full lines in Figure 3.9. We now find much better agreement between the observations and the model where for instance for return rates of from zero to 100% the model agrees with the observed change at the 1-2 mm level. However, at the higher levels of return up to 100 photons, the model over-estimates the total effect by some 4 mm, and does not fully model the observed increase in single-shot precision. Clearly, we have over-estimated the timewalk intrinsic to the SPAD, or our estimate of the laser pulse–width is too large. However, on the assumption that we have correctly estimated the pulse–width, the results from this experiment suggest that the timewalk for our device is some 15 mm, or 100 ps, over a return level of from zero to 100 photons.

### 3.5.4 Satellite Ranging at High Return Level.

We might expect that the bias effects measured from target-board ranging would also be present during satellite ranging if we depart from the single-photon regime. For this experiment, we observed nighttime passes of the satellites ERS-1, Meteor-3, Starlette,

Stella, Lageos and Topex/Poseidon. For the Etalon satellites, their large distances make it unlikely that return levels significantly in excess of single photons can be achieved. At intervals throughout each pass the return levels were changed rapidly between single and multi–photons by removing or inserting ND filters in the receive path. For each pass the single–photon observations were reduced in the standard way, and then the deduced smoothing functions removed from the multi–photon data. Normal points were formed from the raw range measurements, with care taken to ensure that each normal point bin included only low rate or high rate data.

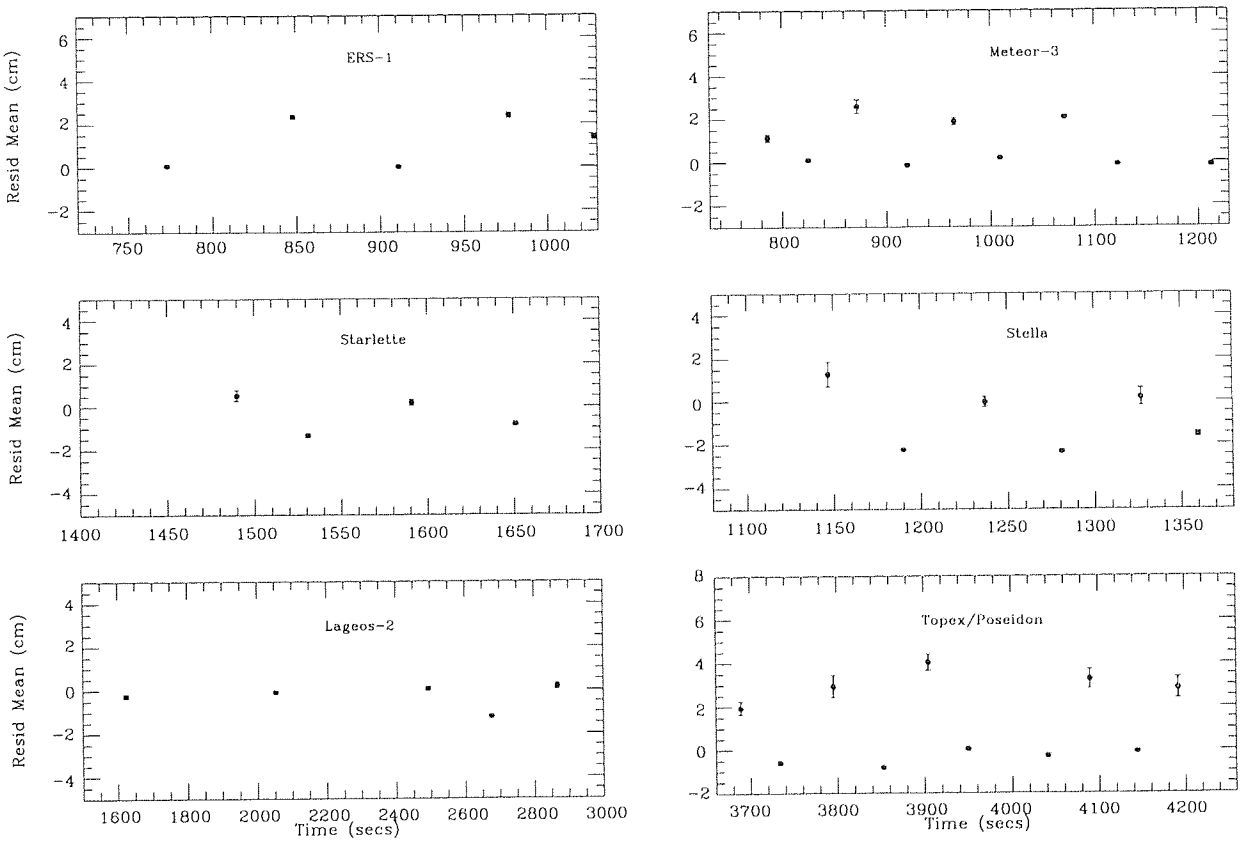


Figure 3.10: Mean values of range residuals - low and high level of return energy

The residuals of the normal points from the smoothing function are displayed in Figure 3.10 where 'steps' of between 10 and 40 mm are clearly evident. From the known densities of the ND filters required to maintain single–photon levels, we have estimated the numbers $n$ of photons reaching the detector during the high-level return phases.

In the plots, the 'upper' points are those obtained at a single-photon return level, and the 'lower' points (reduced range) are those at higher return levels. Formal error

bars are plotted, but these are only distinguishable at the low return level, where fewer observations contribute to the normal points.

Analogous to our model of the target-board results, we have modelled the satellite 'steps' as a function of the numbers of photons reaching the detector. For Lageos we used the model discussed in Section 3.4, and generated response functions for Starlette and the identical Stella from the same analytical treatment of Neubert [16]. We digitized the responses for ERS-1 from the curves derived by Degnan [15], and used the Topex/Poseidon responses of Varghese [23]. We do not currently have a model of the response function of the small Meteor–3 retro-reflector array. We convolved these responses with our system response and sampled from the resulting probability distributions in order to predict the range 'steps'. To these 'step' values we then added the intrinsic timewalk due to the SPAD, as deduced in the target board experiments. The results of the pass–averaged high and low–energy residual peak values and precision estimates, and the observed and predicted steps are shown in Table 3.3, along with the mean numbers of photons $n_p$. In most cases as expected the multi-photon data has the greater single-shot precision, and the predicted 'steps' are in reasonable agreement with the observations, given the quoted observational precision values.

These experimental satellite observations were also carried out at Herstmonceux in collaboration with P. Gibbs, and results presented at and published in the proceedings of the Annual Eurolas Meeting in Munich in 1995 March [24].

### 3.5.5 Lageos CoM values

We have used the simulations in Section 3.5.4 to model the changes to the Lageos centre of mass (CoM) correction appropriate to a range of return energy levels. A system which detects the first photon will sample shot-by-shot during a pass the average distribution of all of these pulses of returning photons. Then when processing the data it is necessary to adopt some feature of this data distribution as the reference point. Possibilities are the mean, peak or leading edge half maximum (LEHM). For the mean it is necessary to reject outliers, and usually a rejection at 3 $\times$ RMS from the mean is used, with the mean being re-determined at each stage of an iterative process. The final range measurement is the difference of the satellite measure and the calibration board measure,

| Sat Name | Single-Photon | | Multi-Photon | | | Step | |
|---|---|---|---|---|---|---|---|
| | Peak mm | rms mm | Peak mm | rms mm | $n_p$ | Obs. mm | Model mm |
| ERS-1 | +24 | 11 | 0 | 9 | 80 | -24 | -35 |
| Meteor | +18 | 14 | 0 | 11 | 20 | -18 | - |
| Star | + 5 | 19 | -10 | 14 | 6 | -15 | -11 |
| Stella | 0 | 12 | -20 | 13 | 12 | -20 | -20 |
| Lag-2 | 0 | 16 | -12 | 15 | 5 | -12 | -10 |
| Topex/P | +35 | 25 | 0 | 10 | 100 | -35 | -55 |

Table 3.3: Observed and modelled energy-dependent range bias.

and the same reference point must be used for both. If the data distributions from the satellite and calibration board were identical then it would not matter which reference point was used. But satellite signatures can cause the distributions to be different, and so the choice of reference point will affect the final range measurement, and this can be expressed as a variation of the value of the appropriate CoM correction. Systems that use MCP detectors respond in some way to the whole of the returning pulse rather than just the first photon, and for these the choice of reference point is made by the setting of a hardware device, rather than subsequently in software. The results are given in Table 3.4 as peak, mean and LEHM. The CoM values have been calculated from the Lageos response model, followed by *subtraction* of the equivalent change of calibration value at each particular return energy level.

We note that this correction implies that calibration and satellite ranging should always be carried out at the same return level; if this is not true, much larger corrections to CoM may be appropriate, depending on the differences in return level. We see that the CoM correction for LEHM processing is little affected by return energy level, as may be anticipated from that statistic's lack of influence from the tail of the distribution. The peak value of CoM is less affected than that of the mean.

| Return Level (photons) | Processing | | |
|---|---|---|---|
| | Peak mm | Mean mm | LEHM mm |
| 1 | 246 | 240 | 250 |
| 2 | 249 | 241 | 249 |
| 3 | 252 | 241 | 249 |
| 4 | 251 | 242 | 250 |
| 5 | 252 | 243 | 250 |
| 6 | 254 | 243 | 248 |
| 7 | 254 | 243 | 247 |
| 8 | 255 | 242 | 248 |
| 9 | 255 | 243 | 248 |
| 10 | 257 | 244 | 248 |
| 50 | 250 | 249 | 250 |

Table 3.4: Lageos CoM corrections with changing return levels.

### 3.5.6 Conclusion.

We have shown that for the Herstmonceux SPAD–based system, departure from the regime of single–photon return levels will result in range bias. We have experimentally examined the degree of bias as a function of return level, over a range of from single to 1000 photons. Simple statistical modelling of the system adequately explains the observational results, and implies that finite pulse-length accounts for about half the bias, and a plausible degree of energy-dependent time-walk within the SPAD system accounts for the remainder. For satellite ranging we find similar energy-dependent biases, which again are adequately explained by our models which include the effect of each satellite's response function. Some of this effect will cancel in practice, provided that the calibration correction applied to the satellite ranging is determined by ranging to a calibration target at the same return level as the satellite ranging. There will be a residual effect due to

the reflection point of the detected photon moving on average towards the nearest point of the satellite, which can be corrected if the return level is known. The problem is that it is difficult to determine the return level when it is higher than single photons, and so it is difficult to make this correction to the reflection point, and also to ensure that satellite and calibration ranging are at the same return levels. Hence we conclude that provided calibration ranging and satellite ranging continue to be carried out at a strictly single–photon level, our normal practice, then range bias is minimal, at the expense of some loss of single–shot precision. A further effect is the choice of reference point from the data distribution from satellite and calibration ranging. At Herstmonceux the peak is adopted, and we have shown that in this case the appropriate CoM correction for Lageos is within a few mm of the recommended standard value.

# Chapter 4

# Orbit Determination Package for SLR Data Analysis

## 4.1 Introduction

The Royal Greenwich Observatory SLR analysis package 'SATAN' consists of two major components. Program ORBIT numerically integrates the equations of motion of the satellite and the variational equations to compute a set of satellite positions and velocities and partial derivatives with respect to a chosen set of parameters. The program computes a sum of forces on the satellite at each step of the integration, based on the IERS(1992) Standards [20], which includes the Earth's irregular gravity field, third-body attractions and non-conservative forces. The second major program RGODYN uses the predicted position of the satellite as computed by ORBIT and for each observation from a given tracking station computes the predicted range to the satellite, and forms the difference of the measured range from this prediction. The program computes the partial derivatives of range with respect to a set of parameters which includes the initial state vector of the satellite, coefficients of the empirical models of the non-conservative forces, the coordinates of the tracking stations and Earth rotation parameters. The program forms and solves the normal equations and computes corrections and their errors to the initial estimates of these parameters. The solution is then iterated by recomputing the orbit based upon the new values of the parameters of interest.

Program ORBIT was written at RGO by Dr A.T. Sinclair, and program RGODYN

by this author. The programs were designed to be developed according to the needs of particular investigations, and have been implemented and modified by several UK research groups. For instance, at RGO, Sinclair has included in the package his short arc method for the computation of station coordinates and baselines by attempting to remove the inevitable residual orbit error due to incomplete knowledge of the force model. The method uses simultaneous observations of a short arc of the satellite orbit from at least two different stations in a solution for the station coordinates and for corrections to the computed orbit in the radial, across-track and along-track directions. Many such short arcs are combined to form a final set of corrected station coordinates. The method was used in a study of the inter-site baselines between six SLR stations in Europe using initially seven [25] then ten [26] years of Lageos tracking data.

During the present study modifications to both these computer programs have been carried out, including expansion of the parameter set, accommodation of the latest gravity field models etc. In this Chapter we give an overview of programs ORBIT and RGODYN, and describe the additions that were carried out as part of the current research.

## 4.2 Program ORBIT

### 4.2.1 Introduction

We begin our description of the main functions of ORBIT with a brief introduction to satellite motion. The motion of an artificial satellite around the Earth is initially treated as a classical two-body problem and described by the following second-order differential equations

$$\ddot{\mathbf{r}} = \frac{-G(m_s + m_e)}{r^3}\mathbf{r}, \tag{4.1}$$

where $\mathbf{r}$ is the vector from the centre of mass of the Earth to the centre of mass of the satellite, $G$ is the universal constant of gravitation and $m_e$ and $m_s$ are the masses of the Earth and the satellite. Since we can ignore $m_s$, we have

$$\ddot{\mathbf{r}} = \frac{-Gm_e}{r^3}\mathbf{r} \tag{4.2}$$

Now the satellite undergoes perturbations by the non-uniform gravity field, by third-body attractions and tidal forces and by non-conservative forces acting on its surface. Thus

we add to (4.2) the sum of the instantaneous accelerations $\ddot{\mathbf{r}}_p$ due to these perturbative forces and also change the notation for $Gm_e$ to $GM$, giving

$$\ddot{\mathbf{r}} = \frac{-GM\mathbf{r}}{r^3} + \ddot{\mathbf{r}}_p = \mathbf{F}, \, say \tag{4.3}$$

For precise work such as for computing orbits for geodetic purposes, numerical integration has superceded analytical solutions because of the much greater ease of inclusion into the equations of motion the large number of forces that significantly affect the motion of the satellite. If we now integrate numerically these three second-order differential equations, we can obtain the predicted position of the satellite at each integration step. The six constants of integration required are the initial state vector of the satellite, $\mathbf{x_0}$ and $\dot{\mathbf{x}}_\mathbf{0}$, or equivalently the initial Keplerian elements $\mathbf{e_0}$.

### 4.2.2 Numerical integration

The numerical integration scheme used is the Gauss-Jackson 8th order process, a multi-step process. The use of a higher-order process would have meant that a larger integration step size could have been used to reach a given accuracy, but for the integration of the equations of motion of an Earth-satellite we need a fairly short step size in order not to under-sample the accelerations due to the high-order terms in the gravity field. The multi-step method is an iterative process of integration using a predictor-corrector scheme whereby formulae are used to progress from an initial position, $s_0$, to a new approximation, $(s_{k+1})$. When an nth order multi-step method is used, the predicted (k+1)th position, say $(s_{k+1})_1$ is obtained by a predictor formula making use of the previous $(n+1)$ values. This value is now used along with the previous $n$ positions to compute using a corrector formula an improved position, say $(s_{k+1})_2$. If the difference between this latest position and the previous estimate exceeds a certain limit, the corrector formula is re-applied using the most recent value of $(s_{k+1})$. It is clear that in order to start this process of integration, the first $(n+1)$ positions must already be available, and so must be computed by a single-step process.

The main advantage of using a multi-step as opposed to a single-step method of integration is that to reach a given accuracy the step-size for a single-step method has to be much smaller than for a multi-step, leading to greater computational effort. This was

confirmed for an integration applied to Lageos by Agrotis [27]. However, a disadvantage is that it is difficult to change the step length during an integration run if that error becomes large or small with respect to some specified criterion. The need for there to be available $(n+1)$ values at intervals of $h$ in order to calculate a new value makes such changes of $h$ inconvenient to program, whereas with a single-step method there would be little problem. If the error is found to be too large for example, we must re-run the whole integration again with a smaller step size.

Along with the integration of the equation of motion of the satellite, we also wish to compute partial derivatives of the satellite coordinates with respect to some parameters of the force model. In order to solve for corrections to initial estimates of a parameter $p$, we need to compute $\frac{\partial x_i}{\partial p}$, for $i = 1, 2, 3$ at each step of the integration. Now

$$\frac{d^2}{dt^2}\left(\frac{\partial x_i}{\partial p}\right) = \frac{\partial F_i}{\partial p} + \sum_{j=1}^{3} \frac{\partial F_i}{\partial x_j}\frac{\partial x_j}{\partial p}, \tag{4.4}$$

where the first term is the explicit partial derivative of the satellite acceleration with respect to the parameter $p$. This system of second order differential equations is called the system of variational equations, and is integrated along with the 3 differential equations of motion of the satellite.

The explicit partial derivative is zero when $p$ is one of the components of $\mathbf{x}_0$ or $\dot{\mathbf{x}}_0$, since $\ddot{\mathbf{x}}$ does not depend explicitly upon the initial position and velocity of the satellite. For other parameters in the force model, such as the coefficient of solar radiation, the explicit partial derivative is computed by differentiation during the evaluation of the acceleration due to that particular force, as outlined in Section 4.3.3. The program currently computes explicit partial derivatives, and hence forms and integrates the variational equations for initial state vector, empirical drag accelerations including once-per-revolution terms, solar radiation coefficients, the product $GM$ of the Gravitational Constant $G$ with the mass $M$ of the Earth, $GM_{Moon}$ and selected terms in the expansion of the gravity field.

### 4.2.3 Force model

In order to integrate the equations of motion, we must of course evaluate the force model at each integration step. Here we outline the principal forces that are evaluated in ORBIT, which essentially conform to the IERS Standards [20]. We point out additions

to the models that have been implemented during this investigation.

### The Earth's Gravitational Potential

The external disturbing potential $U$ of the Earth's gravity field is usually written in terms of an infinite sum of spherical harmonic coefficients $C_{n,m}$ and $S_{n,m}$ (for example, Heiskanen and Moritz [28]). We have

$$U = \frac{GM}{r}\left[1 + \sum_{n=2}^{\infty}\sum_{m=0}^{n}\left\{\frac{a_e}{r}\right\}^n P_{n,m}(\cos\Theta)(C_{n,m}\cos m\lambda + S_{n,m}\sin m\lambda)\right], \tag{4.5}$$

where $a_e$ is the equatorial radius of the Earth, $r$, $\Theta$ and $\lambda$ the geocentric distance, co-latitude and longitude of the satellite. $P_{n,m}$ is the associated Legendre function of degree $n$ and order $m$ given by

$$P_{n,m} = \frac{\sin^m\Theta}{(2^n)n!}\left\{\frac{d}{dP}\right\}^{m+n}(\cos 2\Theta - 1)^n.$$

The Legendre functions are known as zonal harmonics when $m = 0$, tesseral harmonics when $m < n$, and sectorial harmonics when $m = n$, and can be computed by recurrence relationships, for example for the zonals as

$$P_{n,0} = \frac{1}{n}\left[(2n-1)\cos\Theta P_{n-1,0} - (n-1)P_{n-2,0}\right],$$

with

$$P_{0,0} = 1$$

and

$$P_{1,0} = \cos\Theta.$$

The perturbing acceleration $\ddot{\mathbf{R}}$ experienced by the satellite is given by the gradient of the potential field at the satellite. That is

$$\ddot{\mathbf{R}} = \nabla U \tag{4.6}$$

For example the component of acceleration $\ddot{x}_g$ along the x-axis in an Earth-fixed reference frame and due to the $n, m$ harmonic is given by

$$\ddot{x}_g = \frac{\partial U_{nm}}{\partial x_g} = \frac{\partial U_{nm}}{\partial r}\frac{\partial r}{\partial x_g} + \frac{\partial U_{nm}}{\partial\Theta}\frac{\partial\Theta}{\partial x_g} + \frac{\partial U_{nm}}{\partial\lambda}\frac{\partial\lambda}{\partial x_g}, \tag{4.7}$$

where, from (4.5)

$$\frac{\partial U_{nm}}{\partial r} = -GM\frac{a_e^n}{r^{n+2}}(n+1)P_{nm}(\cos\Theta)(C_{nm}\cos m\lambda + S_{nm}\sin m\lambda) \tag{4.8}$$

$$\frac{\partial U_{nm}}{\partial \Theta} = -GM\frac{a_e^n}{r^{n+1}}P'_{nm}(\cos\Theta)\sin\Theta(C_{nm}\cos m\lambda + S_{nm}\sin m\lambda) \tag{4.9}$$

$$\frac{\partial U_{nm}}{\partial \lambda} = -GM\frac{a_e^n}{r^{n+2}}mP_{nm}(\cos\Theta)(-C_{nm}\sin m\lambda + S_{nm}\cos m\lambda) \tag{4.10}$$

Here $P'_{nm}(\cos\Theta)$ represents the derivative of the associated Legendre function with respect to the argument $\cos\Theta$. The partial derivatives of range $r$, co-latitude $\Theta$ and longitude $\lambda$ with respect to the Earth-fixed x-axis $x_g$ of the satellite are given by partial differentiation of the following simple relationships.

$$r = (x_g^2 + y_g^2 + z_g^2)^{\frac{1}{2}},$$

$$\Theta = \tan^{-1}\left[(x_g^2 + y_g^2)^{\frac{1}{2}}\right],$$

$$\lambda = \tan^{-1}\left[\frac{y_g}{z_g}\right].$$

The total component of acceleration along the x-axis is then the sum of such terms up to the degree and order of the particular gravity field that is being used. The accelerations $\ddot{y}_g$ and $\ddot{z}_g$ along the y and z-axes are treated similarly. Then the resultant acceleration vector $\ddot{\mathbf{R}}$ in the Earth-fixed coordinate system is given by

$$\ddot{\mathbf{R}} = \ddot{x}_g\mathbf{i} + \ddot{y}_g\mathbf{j} + \ddot{z}_g\mathbf{k}$$

At this point, we can consider the effect of the ocean tides on the external gravity field. The oceans respond dynamically to the tidal forces exerted by the Sun and Moon. The tides raised have a direct effect on the gravity field, and also cause periodic loading of the solid Earth. This loading causes deformation, which further affects the gravity field. The ocean tidal potential is usually considered as a time-varying component of the solid-Earth potential, and added to the Legendre coefficients prior to evaluating the accelerations $\ddot{\mathbf{R}}$ on the satellite.

Now, in order to compute the acceleration in the inertial frame realised by the J2000 system, $\ddot{\mathbf{R}}$ is transformed from the body-fixed frame to J2000 at each step of the integration. In practice this means that at every step of the integration the position of the

satellite is first transformed to the terrestrial reference frame, in which frame the acceleration due to the gravity field is evaluated. Then the acceleration is transformed back into the J2000 inertial fame where the integration step is carried out. If $\mathbf{X}_I$ is a position vector in the J2000 frame, and $\mathbf{X}_g$ is the position vector in the Earth-fixed frame, then

$$\mathbf{X}_g = S.N.P.\mathbf{X}_I,$$

where $S$ is the sidereal time and polar motion transformation matrix, $N$ the Nutation transformation and $P$ the precession transformation matrices. Here we note that we apply to the conventional IAU precession and nutation the offsets $\delta\Psi$ and $\delta\epsilon$ in longitude and in obliquity as given at five-day intervals in the IERS Bulletin-B series. These corrections are of the order of a few tens of milli-arcseconds (mas).

### The JGM Gravity Field Models

There are in current use several expansions of the geopotential which have been derived by analyses of satellite tracking data, altimetry data and terrestrial gravity measurements. These 'gravity fields' consist of the spherical harmonic coefficients $C_{n,m}$ and $S_{n,m}$ usually given in their normalized forms, denoted $\overline{C}_{n,m}$ and $\overline{S}_{n,m}$. The relationship between a coefficient and its normalized form is

$$C_{n,m} = N_{n,m}\overline{C}_{n,m},$$

where

$$N_{n,m} = \left[\frac{(n-m)!(2n+1)(2-\delta_{0m})}{(n+m)!}\right]^{\frac{1}{2}},$$

and where $\delta_{0m}$ is the Kronecker delta defined by

$$\delta_{0m} = \begin{cases} 1 & \text{for } m = 0 \\ 0 & \text{for } m \neq 0. \end{cases}$$

The gravity field used in the analysis, JGM-3, is the most recent in the series of Joint Gravity Models computed by GSFC and the University of Texas [29]. The models are derived from analysis of SLR, TRANET Doppler, DORIS Doppler and optical tracking data of a large number of satellites, altimeter data from GEOS 3, Seasat and Geosat, and surface gravity data, and is complete to degree and order 70. All the coefficients of the model are normalised. Associated with the gravity field is an extensive ocean tidal

model, being an expanded version of the GEM-T3 tide model, and contains terms for 12 major tidal frequencies. In order to implement correctly the JGM models in ORBIT, several additions to the original model were required. The changes and additions to the force model that we have implemented in order to retain compatibility with the gravity field model are as follows [29]:

$GM$ value of 398600.4415 $km^3s^{-2}$, based on Lageos analyses with a Lageos CoM correction of 251mm [30].

Mean equatorial radius of the Earth of $a_e = 6.3781363Mm$

The gravity field model has an associated epoch of 1986, and rates of change of $C_{2,1}$ and $S_{2,1}$ which must be evaluated. The $\dot{C}_{2,1}$ and $\dot{S}_{2,1}$ terms model the secular motion of the pole due to post-glacial rebound. Also modelled is the secular change $\dot{J}_2$ in the principal zonal coefficient, as identified by Yoder *et al* [31] and Eanes [32] from analysis of the apparent acceleration of the node of Lageos.

Relativistic effects have been applied when generating the JGM models, since at the cm level of accuracy the equations of motion of the satellite should be modified to include the effects of General Relativity. The relativistic effects used in the model are discussed by Huang *et al* [33], from which reference we have extracted the equations to apply to our force model to maintain compatibility with the geopotential model. The relativistic effects include correction to the equations of motion and to the measurement model, which includes a correction to the calculated light time. (We discuss the light-time correction when considering the analysis program RGODYN, below). The two coordinate systems normally used for satellite orbit determination are the solar system barycentric coordinate system and the geocentric system. The barycentric system is usually used for lunar laser ranging, VLBI and the dynamics of the solar system, while the geocentric system can be expressed as one of two different systems, inertial or non-inertial. The relativistic equations of motion are different depending on whether the barycentric or geocentric reference systems are used, but lead to geodetic solutions which are equivalent at least at the few cm level [34]. The introduction of a non-inertial geocentric reference system satisfies the convention that the amount of geodesic precession of the Earth predicted by General Relativity is included in general precession [35]. This reference system retains the merits of the inertial geocentric system, namely that the scales of time and length

are to high precision unchanged, but because it is non-inertial, the effect of geodesic precession must be included in the equations of motion of the satellite. This effect is due to precession of the inertial geocentric reference system with angular velocity $\mathbf{\Omega}$ with respect to the barycentric reference system; it can also be called the relativistic Coriolis acceleration. The effect on the satellite orbit is an average precession of the node of 17.6 mas $\mathrm{yr}^{-1}$, as well as effects on the argument of perigee and on inclination which depend upon the particular orientation of the node [33]. Because the Sun is the only significant contributor to geodesic precession, Huang *et al* [33] found a simple expression for $\mathbf{\Omega}$

$$\mathbf{\Omega} \approx \frac{3}{2}(\mathbf{V}_E - \mathbf{V}_S) \times \left[\frac{-GM_S\mathbf{X}_{ES}}{c^2 R_{ES}^3}\right], \tag{4.11}$$

where $\mathbf{V}_E$ and $\mathbf{V}_S$ are the barycentric velocities of the Earth and Sun, $\mathbf{X}_{ES}$ is the Earth-Sun vector in the same frame, and $R_{ES}$ is its magnitude. Then the geodesic precession acceleration is given by $2(\mathbf{\Omega} \times \mathbf{v})$, where $\mathbf{v}$ is the velocity of the satellite. The other two effects of General Relativity which have been modelled are the Schwarzschild solution (SS) and the relativistic effects caused by the Earth's rotation, the Lense-Thirring (LT) perturbation. Huang *et al* [33] give the following expressions for these accelerations,

$$\mathbf{a}_{SS} = \frac{GM}{c^2 r^3}\left[\left[4\frac{GM}{r} - v^2\right]\mathbf{r} + 4(\mathbf{v}.\mathbf{r})\mathbf{v}\right] \tag{4.12}$$

$$\mathbf{a}_{LT} = 2\frac{GM}{c^2 r^3}\left[\frac{3}{r^2}[\mathbf{r} \times \mathbf{v}][\mathbf{r}.\mathbf{J}] + [\mathbf{v} \times \mathbf{J}]\right] \tag{4.13}$$

In the expression for $\mathbf{a}_{LT}$, the Lense-Thirring acceleration, $\mathbf{J}$ is the Earth's angular momentum per unit mass, with magnitude approximately $9.8 \times 10^8 m^2 s^{-1}$. In the units used by program ORBIT, this value converts to 84.7 $\mathrm{Mm}^2\ \mathrm{day}^{-1}$. Again the effect of this perturbation is a motion of the longitude of the node of the orbit of the satellite.

The expressions above for the relativistic accelerations require barycentric coordinates and velocities of the Earth and the Sun. To supply these quantities to ORBIT, we modified the programs that take the positions and velocities of the Sun, Earth/Moon system and the planets from the JPL ephemerides. These programs compute daily polynomial coefficients for rapid evaluation in order to calculate the third body accelerations.

For short and medium-arc studies of up to a month or so, the omission of these relativistic effects when using the JGM gravitational models will not be serious, and the errors introduced into the force model will be absorbed by solution for initial state vector.

However, for long-arc studies, the subject of the present work, the use of the gravitational model without the relativistic corrections will produce a spurious motion of the node, as well as effects on the inclination and argument of perigee. We consider that such an effect may possibly be the cause of the problem noted by Harwood and Swinerd [36] when using the current SATAN package to analyse a year-long set of Lageos observations to test their theory for long-term orbital variations due to direct solar radiation pressure. They found significant discrepancies in inclination between the theoretical variations and those from their data analysis using the package. The maximum discrepancy in the inclination was approximately 25 mas over the one year interval, which is at the level of the relativistic effects discussed above.

### Solid Earth Tides

The potential at any point $A$ on the surface of the Earth due to either the Moon or the Sun is

$$U_A = \frac{GM_j}{\rho}, \tag{4.14}$$

where $M_j$ is the mass of the Moon or Sun and $\rho$ is the distance between point $A$ and the centre of mass of the perturbing body. We have

$$\rho^2 = r^2 + r_j^2 - 2rr_j \cos z,$$

where $r$ and $r_j$ are the geocentric distances of point $A$ and the centre of mass of the Moon or Sun respectively. Angle $z$ is approximately the zenith distance at point A of the perturbing body. Equation (4.14) is then re-written

$$U_A = \frac{GM_j}{(r^2 + r_j^2 - 2rr_j \cos z)^{\frac{1}{2}}}.$$

This can be expressed as an infinite series in terms of Legendre functions, as

$$U_A = \frac{GM_j}{r_j} \sum_{n=0}^{\infty} \left(\frac{r}{r_j}\right)^n P_n(\cos z). \tag{4.15}$$

We then obtain the tide-raising potential $U_T$ by evaluating (4.15) for $n \geq 2$. However, the only significant effect is that of the second harmonic, $n = 2$, so we have

$$U_T = \frac{GM_j r^2}{r_j^3} P_2(\cos z). \tag{4.16}$$

The Earth responds to this tidal potential by deforming, causing an additional potential at a distance $r$ from the geocentre of the form

$$U = \frac{H}{r}\left(\frac{a_e}{r}\right)^2 P_2(\cos z), \tag{4.17}$$

where $H$ is a constant. On the Earth's surface $r = a_e$, so

$$U_B = \frac{H}{a_e} P_2(\cos z). \tag{4.18}$$

Now the potential on the Earth's surface due to the deformed Earth is also given by equation (4.16) as

$$U_B = k_2 \frac{GM_j a_e^2}{r_j^3} P_2(\cos z), \tag{4.19}$$

where $k_2$ is the Love number with nominal value 0.3. Now equating (4.18) and (4.19) we have

$$H = k_2 \frac{GM_j a_e^3}{r_j^3},$$

and by substitution into (4.17) we have the potential of the tidal bulge at any point given by

$$U = k_2 \frac{GM_j a_e^5}{r^3 r_j^3} P_2(\cos z). \tag{4.20}$$

The Legendre function, $P_2(\cos z)$, is given by

$$P_2(\cos z) = \frac{3}{2}\cos^2 z - \frac{1}{2},$$

with

$$\cos z = \frac{\mathbf{r}.\mathbf{r}_j}{r r_j},$$

and $\mathbf{r}_j$ is the geocentric vector to the Moon or Sun. Then the potential at the satellite of the tidal bulge becomes

$$U = k_2 \frac{GM_j a_e^5}{2r^3 r_j^3}\left[3\frac{(\mathbf{r}.\mathbf{r}_j)^2}{r^2 r_j^2} - 1\right].$$

Then the acceleration $\ddot{\mathbf{R}}$ experienced by the satellite is grad $U$. So

$$\ddot{\mathbf{R}} = k_2 \frac{GM_j a_e^5}{2r^5 r_j^3}\left[-15\frac{(\mathbf{r}.\mathbf{r}_j)^2}{r^2 r_j^2}\mathbf{r} + 6\frac{(\mathbf{r}.\mathbf{r}_j)}{r r_j}\mathbf{r}_j + 3\mathbf{r}\right]. \tag{4.21}$$

This expression is evaluated for both the Moon and the Sun. The Love number $k_2$ is a measure of the response of the Earth to the tidal potential $U_T$, but is not a constant as

it varies depending upon the frequency of the tide being considered. The effects of the frequency dependence of $k_2$ are best included as corrections to the spherical harmonic coefficients of the geopotential expansion. A two-step procedure is therefore used to compute the Earth tidal accelerations on the satellite; in the first step a nominal value of $k_2 = 0.3$ is used along with equation (4.21). Then corrections to $C_{n,m}$ and to $S_{n,m}$ are computed according to the formulation of Eanes *et al* [37] which allow for corrections to $k_2$ dependent on the frequency of the tide being considered.

### Third-body Attractions

The Sun, Moon and planets exert a gravitational attraction on both the satellite and on the Earth, and the resultant acceleration on the satellite, in the direction of the third body, must be modelled. The acceleration of the Earth arising from the attraction of the third body is given by the gradient of the potential due to that body, and can be written

$$\ddot{\mathbf{r}}_E = -\frac{Gm_j}{(r_E - r_j)^3}(\mathbf{r}_E - \mathbf{r}_j), \tag{4.22}$$

where $m_j$ is the mass of the third body, $\mathbf{r}_E$ and $\mathbf{r}_j$ are the geocentric position vectors in an inertial reference frame (J2000) of the Earth and of the $j^{th}$ body. Similarly, the acceleration of the satellite relative to the third body is given by

$$\ddot{\mathbf{r}}_s = -\frac{Gm_j}{r - r_j^3}(\mathbf{r} - \mathbf{r}_j), \tag{4.23}$$

Now the origin of the coordinate system is the geocentre, so $\mathbf{r_E}$ is the zero vector. The acceleration vector $\ddot{\mathbf{r}}_{tb}$ of the satellite relative to the Earth is the difference of these two accelerations, and is given by $\ddot{\mathbf{r}}_{tb} = \ddot{\mathbf{r}}_s - \ddot{\mathbf{r}}_E$, or

$$\ddot{\mathbf{r}}_{tb} = -Gm_j\left[\frac{(\mathbf{r} - \mathbf{r}_j)}{(r - r_j)^3} + \frac{\mathbf{r}_j}{r_j^3}\right] \tag{4.24}$$

We currently include third body attractions from the Sun, Venus, Moon, Mars, Jupiter and Saturn, with masses taken from IERS Standards [20].

### Indirect Oblateness

We have added to the third-body force model the indirect oblateness acceleration due to the effect of principally the Earth's $J_2$ coefficient on the Moon; the force exerted on

the Moon is matched by an equal and opposite force by the Moon on the Earth, causing an additional acceleration which should be applied to the model of accelerations on the satellite to better refer these accelerations to the centre of the Earth [38]. The indirect oblateness acceleration $\ddot{\mathbf{r}}_{ob}$ is given by Merson and Odell [39] and Sinclair and Taylor [40] as follows.

$$\ddot{\mathbf{r}}_{ob} = \frac{M_{moon}}{M_{Earth}} \nabla \mathbf{r}, \tag{4.25}$$

where

$$\nabla \mathbf{r} = A\mathbf{r}_m + B\mathbf{k}, \tag{4.26}$$

with $\mathbf{r}_m$ the geocentric position vector of the Moon, $\mathbf{k}$ the unit vector in the z-direction, and

$$A = \frac{GM}{r_m^3} J_2 \frac{a_e^2}{r_m^2} P'_3 \left(\frac{z_m}{r_m}\right),$$

$$B = -\frac{GM}{r_m^2} J_2 \frac{a_e^2}{r_m^2} P'_2 \left(\frac{z_m}{r_m}\right),$$

and as before $P'(s)$ is the derivative of the Legendre polynomial in $s$.

We find from the above that the geocentric components of the acceleration on the satellite are

$$\ddot{x} = \frac{15}{2} E x_m - \frac{3}{2} F x_m,$$
$$\ddot{y} = \frac{15}{2} E y_m - \frac{3}{2} F y_m,$$
$$\ddot{z} = \frac{15}{2} E z_m - \frac{5}{2} F z_m,$$

where

$$E = \left(\frac{GM_{Moon}}{r_m^7} J_2 a_e^2 z_m^2\right)$$

and

$$F = \left(\frac{GM_{Moon}}{r_m^5} J_2 a_e^2\right).$$

Tests on the implementation in ORBIT of the indirect oblateness effect showed that its magnitude is about $1.4 \times 10^{-11} ms^{-2}$, which is an order of magnitude greater than typical drag-like accelerations on high-orbiting geodetic satellites. The effect is satellite-independent, and the computed magnitude agrees very well with that estimated by Milani, Nobili and Farinella [41].

### Direct solar radiation pressure and the shadow problem

The acceleration $\ddot{\mathbf{r}}_R$ on a spherical satellite due to direct solar radiation pressure is given by (for example Smith *et al* [38]),

$$\ddot{\mathbf{r}}_R = -\nu C_R \left[\frac{A}{M}\right] P_s \hat{\mathbf{r}}_s, \tag{4.27}$$

where $\nu$ is the eclipse factor allowing for shadowing of the satellite by the Earth or Moon, $C_R$ is the satellite radiation pressure coefficient, $A$ is the effective cross-sectional area of the satellite of mass $M$, $P_s$ is the direct solar radiation pressure at the satellite and $\hat{\mathbf{r}}_s$ is the geocentric vector pointing towards the Sun. The quantity $P_s$ is specified by its mean value at a distance from the Sun of 1AU, and scaled to the instantaneous distance of the satellite from the Sun through a term $(r_s/r_{1AU})^2$. Now $P_s = s/c$, where $s$ is the mean output energy of the Sun, approximately 1.38 $\times 10^{10}$ erg m$^{-2}s^{-1}$ [11]. The parameter $C_R = 1 + \rho_s$, where $\rho$ is the specular reflectivity of the satellite surface, and where $C_R$ is a solve-for quantity in the orbit-determination process, and we find $C_R \approx 1.2$ for the Etalon satellites. For these satellites, with $[A/M] \approx 9.3 \times 10^{-4}$m$^2$ Kg$^{-1}$, the acceleration due to direct solar radiation pressure is approximately $\ddot{r}_R = 5 \times 10^{-9}$m s$^{-2}$. The eclipse factor $\nu$ is represented in ORBIT as a sinusoidal function running from a value of 1 with the satellite in full sunlight to zero when the satellite has fully passed through the penumbra into the umbra of the shadow.

Whilst carrying out our preliminary analysis of observations of the Etalon satellites, we discovered that it is necessary to use an integration step length short enough that a few steps are computed within this modelled penumbral region of the shadow. Initially an integration step length of 5 minutes was used, and an orbital fit to over 60 days of SLR data yielded a residual rms of 12 cm. However, upon the onset of a season of eclipses of the satellite, the rms immediately rose to 25 cm. This change was traced to the introduction of errors into the computed orbit when the modelled solar radiation force was in effect instantaneously switched on or off; a more gradual change in the force at the shadow boundary not only more closely represents the reality of the situation, but would also prevent numerical instability in the integration of the equations of motion. Reducing the step length to 0.5 min restored the 12 cm rms of fit. This sensitivity of the orbital model to the way in which the shadow effect is handled prompted further investigation,

both into the way that ORBIT models the eclipse effect, and also into the phenomenon itself.

It was decided initially to compare the computed circumstances of an eclipse with that observed photometrically. The SLR system at Herstmonceux has been used to make photometric observations of such satellites as rocket bodies, and the author has shown [42] that the observations are useful for deriving rotation period and direction of spin axis. Modifications by the SLR team to the operational software have further made it possible to obtain photometric observations of satellites whilst ranging is being carried out, and several such observations of the geodetic satellites have been made including some instances of the satellites entering or emerging from the Earth's shadow. We have as yet been unable to obtain an observation of an Etalon satellite undergoing a shadow passage, mainly because the satellites appear very faint. A typical example of a shadow passage is shown by the dotted curve in Fig 4.1, which is of Lageos-2 emerging from the shadow during a pass on 1994 March 11. The graph shows as a function of time a measure of the observed intensity of sunlight reflected from the satellite, expressed as the number of events recorded by the photomultiplier every 200 milli-seconds. The number of counts obtained before the satellite emerges from the shadow represents the sky background. We see from the observations that the emergence from the shadow is a gradual phenomenon, lasting some 20 seconds.

From these observations of Lageos-2 we have derived the observed time and duration of shadow boundary passage. We take as the time of start of the eclipse an estimate of the half-light time during the penumbral passage, that is at a time of about 2626 seconds read from the graph.

We now wish to use ORBIT to investigate the computed eclipse time and duration, by looking at the calculated eclipse factor $\nu$. It was found initially that within ORBIT the penumbral region had been artificially magnified five times to ensure that at least a few integration steps did occur within the modelled penumbra, so that a smooth sinusoidal increase or decrease of the solar radiation force could be applied to the force model. This magnification meant that the computed duration of penumbral passage was of course much larger than that observed. It was also considered likely that 'extra' eclipses would be predicted to occur within such a large shadow region. Thus the five times magnification

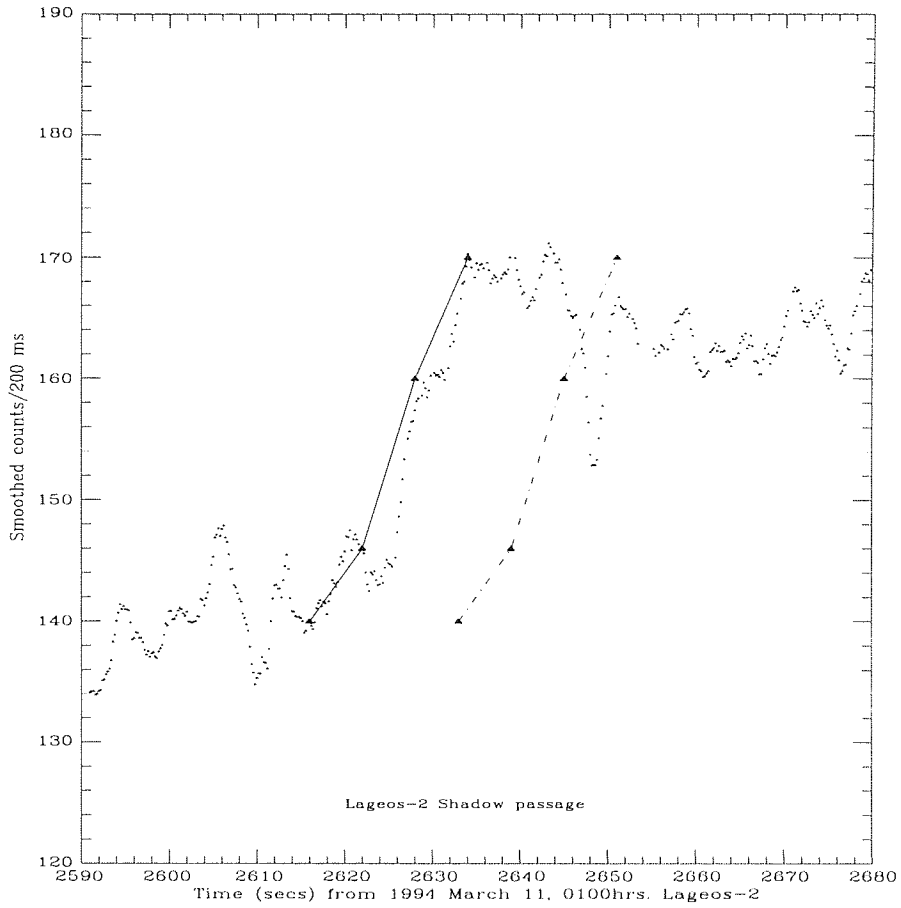


Figure 4.1: Photometric Observations of Lageos-2 during Emergence from the Earth's Shadow.

factor was removed, and the penumbral passage time and duration again computed.

We have plotted these predicted times of shadow passage as given by program ORBIT for the Lageos-2 pass in Figure 4.1, where we have scaled the computed values of $\nu$ from their initial range of from zero to one, to run from 140 to 170, the range of the observed photomultiplier counts. The points are plotted as filled triangles, and are joined by dashed lines.

We immediately see that the predicted time of emergence from the shadow is some 18 seconds later than observed, but that the duration of penumbral passage is predicted fairly accurately. The implications are that the radius of the shadow used in the computations is bigger than the true radius. We find that during this eclipse passage the satellite is moving at 4.6 km $s^{-1}$ relative to the shadow boundary, and that therefore the observations imply a correction to the assumed shadow radius of about 82 km.

The shadow radius used by ORBIT is 6.356752*1.02 Mm, the factor 1.02 presumably being used to model the Earth's atmosphere, giving a radius of 6.483887 Mm. However the IERS recommended value is 6.402000 Mm [20], some 80 km smaller. Using this IERS value in the computations changed the computed time of shadow passage by nearly 18 seconds, so that the computed times now agree to within a few seconds of the observations. The results of these modifications for the pass of Lageos-2 are shown by the continuous line in Figure 4.1.

We now return to the question of the choice of integration step-length required to ensure the smooth transition of the modelled solar radiation force from full sunlight to shadow conditions. The angular extent of the penumbra equals the apparent diameter of the Sun, about 0.5 degrees. Thus we calculate the time taken for the satellites to move through this angle along their orbits, and choose some fraction of this time as the optimum step-length. Such a value for the duration of shadow passage will of course be a minimum for the given satellite, as we are assuming that the impact angle of entry into the penumbra is a right angle. For smaller impact angles, the duration will be longer than calculated here. The calculations were carried out for a variety of satellites, as shown in Table 4.1. To calculate the step length, we required that 3 integration steps are carried out within the penumbral region.

| Satellite | Penumbra | Step | Step |
|---|---|---|---|
| | s | s | s |
| ERS-1 | 8 | 3 | 30 |
| Topex | 9 | 3 | 30 |
| Lageos | 20 | 6 | 60 |
| Etalon | 56 | 18 | 180 |

Table 4.1: Computed Penumbral Passage Times and Recommended Integration Step-Lengths.

For precise work during eclipse seasons a short integration step-length should ideally be used, and use of the values in Table 4.1 should ensure that no such problems arise. However, using a short step throughout the orbit integration would be prohibitably time

consuming and lead to a large accumulation of rounding errors. Further, the multi-step integration process is not easy to modify to allow a change of step-length during an orbit computation. So we reverted to the original scheme of enlarging the modelled penumbra region by now a factor of ten, and to remove the occurrence of 'false eclipses' we first identified the true start and end dates and times of the eclipse seasons, and then only 'allowed' eclipses that fell within these seasons. The revised step-lengths based upon the enlarged penumbra region are also given in Table 4.1. It may prove beneficial to review this process in the future. It is also believed that the photometric observations reported here are the first such recorded for satellites whose orbits are so precisely known, and we suspect that they may prove useful in other shadow boundary problems. In particular, we expect such observations to contain information about the cross-section shape of the shadow cone, which in ORBIT is modelled as a cylinder, but in reality must closely follow the oblate shape of the Earth. Theoretical models of the eclipse problem for artificial satellites are now beginning to take into account the non-cylindrical nature of the shadow [43] and our observations may contribute to such work. We have now implemented in program ORBIT the IERS value for the shadow radius, and the enlarged penumbral region. With these modifications we find that we can safely use the integration step size of 180 seconds given in Table 4.1 for the preliminary analysis of Etalon data, with no loss of precision during shadow passages.

### Earth-reflected radiation

The model of Earth reflected radiation used in ORBIT is that developed by McCarthy and Martin [44]. However our implementation of the model is valid only up to a satellite height of 2000 km, and simple extrapolation created values that were in error by several orders of magnitude, when checked using estimated values. An approximate calculation suggests that at the height of the Etalon satellites, the pressure due to Earth reflected radiation is about 100 times less than the direct solar radiation pressure, giving rise to an acceleration of about $5 \times 10^{-11}$m s$^{-2}$ [45]. This is a significant acceleration, and we consider it important to extend McCarthy and Martin's model to make it applicable at the height of the Etalon satellites. We first summarize their development, and then explain the extension.

The albedo $\gamma$ of the Earth is defined as the fraction of the total incident radiation which is reflected back into space. If the incident solar flux is $F_s$ and the optical re-emitted flux is $F_{OP}$, then

$$F_{OP} = \gamma F_s \tag{4.28}$$

The total power incident on the Earth must equal the total power re-emitted in order to maintain thermal equilibrium, so

$$F_s = F_{OP} + F_{IR}, \tag{4.29}$$

where $F_{IR}$ is the infra-red re-emitted flux. Therefore

$$F_{IR} = (1 - \gamma)F_s \tag{4.30}$$

The average value of the albedo is approximately 0.3 [46]. This implies that $F_{OP} \approx 0.3F_s$ and $F_{IR} \approx 0.7F_s$. The optical emission of the Earth can be sub-divided into specular and diffuse reflection. The specular component is however much smaller than the diffuse component, because only calm water and smooth ice surfaces reflect specularly.

The optical flux is emitted only by the daylight side of the Earth, and will depend upon the local incidence angle of the Sun to each element of the Earth's surface. The acceleration on the satellite will have components in radial, along-track and across-track directions, the radial component being maximum when the satellite is above the centre of the daytime hemisphere, and the across-track component is maximum when the satellite is above the terminator. The IR component of the reflected radiation is not solar-angle dependent, depending only on the mean temperature of the Earth's surface, which varies only slowly with the seasons. The IR flux therefore has little effect on the along-track acceleration of the satellite.

The force on the satellite can in principle be calculated by integrating the force from each element of surface area visible to the satellite. Each element of surface area $\delta a$ has incident upon it solar energy $F_i$ given by

$$F_i = F_s \cos\Theta_s \delta a,$$

where $\Theta_s$ is the angle between the surface normal and the Sun. If the distance from the satellite to the surface element is $r$ and with the satellite cross-sectional area $A$, the

satellite subtends a solid angle $\delta\Omega$ when viewed from the surface element, and

$$\delta\Omega = \frac{A}{r^2}$$

Then the power received by the satellite from the surface element $\delta a$ is

$$\delta F_0 = \frac{1}{\pi}\gamma(a)F_i \cos\alpha\delta\Omega \tag{4.31}$$

or

$$\delta F_0 = \frac{1}{\pi}\gamma(a)F_i \cos\alpha\frac{A}{r^2} \tag{4.32}$$

where $\alpha$ is the angle between the surface normal and the satellite and $\gamma(a)$ is the albedo of the surface element. If we divide $\delta F_0$ by $A$ and by the speed of light, we have an expression for the radiation *pressure* $\delta P_a$ on the satellite from one surface element $\delta a$.

$$\delta P_a = \frac{\gamma(a)F_s \cos\Theta_s \cos\alpha}{c\pi r^2}\delta a. \tag{4.33}$$

So the total pressure is

$$P_a = \frac{F_s}{\pi c}\int_\omega \frac{\gamma(a)\cos\Theta_s \cos\alpha}{\Omega^2}da, \tag{4.34}$$

where $\omega$ is the part of the Earth's surface visible to the satellite.

Then by multiplication of $P_a$ by $\left[\frac{A}{M}\right]$, we have the acceleration $\ddot{\mathbf{r}}_a$ on the satellite due to reflected radiation, which can be compared to the effect of the direct solar radiation acceleration $\ddot{\mathbf{r}}_R$.

The calculation of the albedo pressure and from it the acceleration to add to the force model could be calculated by evaluating the integrals in equation (4.34). However, the procedure would be time-consuming and difficult to carry out if any of the true variation of albedo across the surface of the Earth is to be represented by the variable $\gamma$. The approach adopted by McCarthy and Martin [44], and implemented in ORBIT, is as follows. At each position in the orbit at which the albedo pressure is to be computed, a set of $i$ locations on the visible Earth is calculated. Associated with each location is an element of surface area $\delta a_i$. For each location, the interpolated albedo and the incident solar radiation are determined, and the vector of the pressure on the satellite due to that element is computed. The program uses 13 area elements at present. The first step in the evaluation is to calculate the viewing angle of the satellite, which determines the amount

of the Earth's surface visible to the satellite. For a given satellite height $h$, the maximum area visible to the satellite is enclosed in a cone of half-angle $\Theta_m$, where

$$\Theta_m = \arcsin\left[\frac{a_e}{a_e + h}\right] \tag{4.35}$$

The elements of area, at which the albedo values are calculated, are located at the intersections of the Earth's surface and a set of rays emanating from the spacecraft. The set of rays includes the radius vector of the satellite, and two rings of rays whose angles from the radius vector are fixed fractions of $\Theta_m$. Each ray is a vector along which the albedo pressure is applied to the satellite. After the location of the surface element has been determined, the albedo and incident radiation at this spot are computed and then the magnitude of the albedo pressure $\delta P(i)_a$ on the satellite due to the $i^{th}$ surface element is calculated, as in equation (4.33). The total pressure vector on the satellite is then

$$\mathbf{P}_a = \sum_{i=1}^{n} \delta P(i)_a \hat{\mathbf{r}}_i \tag{4.36}$$

where currently $n = 13$ and $\hat{\mathbf{r}}_i$ is the unit vector of the $i^{th}$ ray.

To enable the calculation of the pressure for satellites above the original 2000 km, we derived polynomial functions with argument satellite height which preserved the relationship between the angle $\Theta_m$ and the angles between the radius vector and the two rings of rays. The modified program accepts satellite heights up to the geostationary distance. We carried out a test to check the computed albedo accelerations on an Etalon satellite. At each integration step we output the magnitude of the acceleration due to Earth-reflected IR and optical flux, and have plotted against time the separate values, as well as their sum, in Figure 4.2. We see that the acceleration due to the IR flux (dotted line) varies as expected very little throughout the day, but that the acceleration due to the optical flux (dashed line) is periodic with a minimum of zero and maximum of 120 $pms^{-2}$, with a period of about 700 minutes. This is the expected behaviour, as during each orbit the satellite will be above alternately a fully-lit and a completely dark Earth. The average value of the optical acceleration is about 60 $pms^{-2}$, in reasonable agreement with the estimate of Lucchesi [45].

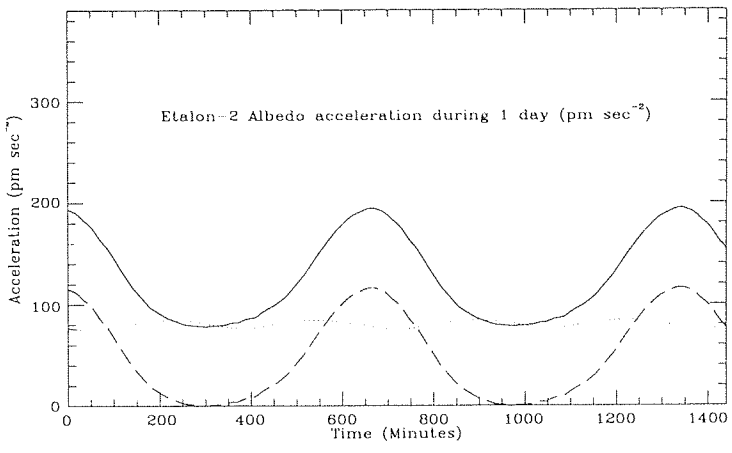


Figure 4.2: Computed Albedo acceleration on Etalon-2; dotted line is due to IR, dashed line due to optical; full line the sum.

### Empirical Drag

Acceleration on the satellite due to a drag force is modelled in ORBIT in two ways; one by evaluation of the density of the atmosphere using a model of the variation of density with height, solar activity and position of the Sun; two by treating the drag as an empirical acceleration acting in the opposite direction to the motion of the satellite. The first method, in which an atmospheric model such as Jachia72 [47] is used to estimate the drag, is appropriate for satellite heights of up to about 1000km. Above this other effects such as thermal drag dominate, and an empirical treatment is initially more appropriate. In this work, we use only the second method, and will not consider further the atmospheric density models. If the empirical acceleration on the satellite has magnitude $E$, then in vector form the acceleration can be written

$$\ddot{\mathbf{r}}_d = E\frac{-\dot{\mathbf{r}}}{\dot{r}} \tag{4.37}$$

The explicit partial derivative of the acceleration with respect to the drag $E$ is then simply equal to $\frac{-\dot{\mathbf{r}}}{\dot{r}}$. Piecewise continuous values of the empirical acceleration are applied at intervals throughout the integration under the control of a series of epochs and values read in at the start of the integration run. We have added to this scheme the computation of once-per-revolution empirical drag terms, of the form $a_1 \sin(\bar{M} + \omega) + a_2 \cos(\bar{M} + \omega)$. Explicit partial derivatives are formed as for the drag terms, and a series of accelerations $a_1$ and $a_2$ are read in by the program.

## 4.3 Program RGODYN

### 4.3.1 Introduction

For each range observation $R_{obs}$ being processed, RGODYN uses the position of the satellite calculated by ORBIT to compute the expected range $R_{calc}$ at the time of the observation. The program forms the difference $R_{obs} - R_{calc}$, and forms an observational equation of the form

$$\sum_{i=1}^{n} \left( \frac{\partial R}{\partial p_i} \Delta p_i \right) = R_{obs} - R_{calc} + \nu, \tag{4.38}$$

where $\nu$ is the least squares residual which we will seek to minimise. The $p_i$ are the parameters to which we will obtain corrections during the process. In this Section, we will discuss the computation of the range, the partial derivatives, and the corrections to the parameters.

### 4.3.2 Computed Range

The observations consist of an epoch (UTC) and a measured 2-way time-of-flight $\tau$ expressed in pico-seconds, as well as supplementary meteorological data and an observing station code. The position of the satellite calculated by ORBIT for the observational instant is expressed as geocentric position $\mathbf{x}$ in mega-meters and velocity $\dot{\mathbf{x}}$ in mega-meters day$^{-1}$ with respect to the J2000 reference frame. The initial station coordinates and horizontal velocities are taken from the ITRF 1993, for epoch 1993.0 and are expressed as geocentric rectangular coordinates. The coordinates frequently refer to a marker near the laser ranging system, and information from local surveys is used to give the 3-dimensional offset of the marker from the invariant point of the tracking system. Sets of these offsets, or eccentricity vectors, are stored in NASA's data centre CDDIS along with the dates during which a particular set applies. At each observational instant we compute from the station velocity its horizontal displacement due to plate motion and apply it and the eccentricity to the station coordinates.

If the Earth-fixed rectangular coordinates of the station are given by $\mathbf{x}_g$, then we must rotate them to the J2000 frame in order to compute the topocentric range. Then

$$\mathbf{x}_{st} = N^T P^T S^T \mathbf{x}_g + \mathbf{x}_{tid}, \tag{4.39}$$

where $S$ the sidereal angle and polar position rotation matrix refers the station coordinates first to the instantaneous axis of rotation of the Earth via the polar motion series, and then to the true equator and equinox of date via the sidereal angle. In more detail, since we shall need matrix $S$ when computing partial derivatives with respect to the Earth rotation parameters, we form matrix $S$ as the product of three rotation matrices. First, we rotate about the y-axis by $-x_p$, then about the x-axis by $-y_p$, where the $x_p, y_p$ are the instantaneous values of the polar coordinates with respect to the IERS reference pole. We then rotate about the z-axis by the Greenwich Apparent Sidereal Time (GAST) to refer coordinates to the true equinox of date. GAST is defined as $GAST = GMST +$ equation of the equinoxes, where Greenwich Mean Sidereal Time is given as a function of UT1 by the standard expression of Aoki *et al.* [48]. Then, by multiplying these three rotation matrices, we find

$$S^T = \begin{pmatrix} \cos x_p \cos\Theta - \sin x_p \sin y_p \sin\Theta & -\cos y_p \sin\Theta & -\sin x_p \cos\Theta - \cos x_p \sin y_p \sin\Theta \\ \cos x_p \sin\Theta + \sin x_p \sin y_p \cos\Theta & \cos y_p \cos\Theta & -\sin x_p \sin\Theta + \cos x_p \sin y_p \cos\Theta \\ \sin x_p \cos y_p & -\sin y_p & \cos x_p \cos y_p \end{pmatrix},$$

where $\Theta = GAST$ expressed in radians. $NP$, the nutation-precession matrix, then refers the station coordinates to the mean equator and equinox of J2000. $\mathbf{x}_{tid}$ is the displacement of the station due to the solid tide effects of the Sun and Moon, as detailed in IERS Standards 1992 [20]. Then, for the moment ignoring the motion of both the satellite and the station during the light-time to the satellite, the predicted one-way range to the satellite at the observational instant is just

$$R = \left[(x - x_{st})^2 + (y - y_{st})^2 + (z - z_{st})^2\right]^{\frac{1}{2}} \tag{4.40}$$

In practice, we iterate the time-of flight calculation in two stages. First we compute from (4.39) the position of the station at the observational instant, and for the same instant the position of the satellite. Then equation (4.40) gives the calculated one-way range, and hence an estimate of the time at which the laser pulse reaches the satellite. The process is iterated until there is no further improvement in this time, and hence in the one-way calculated range. A similar process is carried out for the return of the pulse to the observing station, where now we converge on a time of return, and hence from (4.39) the position of the station at that time. We then have from (4.40) the one-way

return range. The sum of the two parts of the range constitutes the calculated two-way time-of-flight to the satellite. This quantity is then corrected for the large tropospheric delay that the measurement will be subject to, using the model of Marini and Murray [49] and the local meteorological measurements. We also apply a small relativistic correction, which arises through space-time curvature near a massive body. For near-Earth satellites when we work in the geocentric reference frame, the only body that need be considered is the Earth [34]. The correction in seconds is given in IERS Standards 1992 [20] as $\Delta\tau$, where

$$\Delta\tau = \frac{2GM}{c^3} \ln\left(\frac{R_1 + R_2 + R}{R_1 + R_2 - R}\right),$$

and $R_1$, $R_2$ are the distances from the centre of the Earth to the beginning and end of the light path respectively. We find for Etalon, $\Delta\tau \approx 4 \times 10^{-11} s$, equivalent to about 1 cm in range.

We then form the difference $R_{obs} - R_{calc}$, and need to compute range partial derivatives in order to form the equation of condition (4.38). For the calculation of approximate partial derivatives, we now take the 'range' $R$ to be the one-way distance to the satellite at the observational instant, equal to half the computed time-of-flight multiplied by the speed of light.

### 4.3.3 Partial Derivatives

The partial derivatives fall into two categories. Those that depend upon parameters of the force model are computed by numerical integration of the variational equations, as outlined in section (4.2.2). Parameters in this category include the initial state vector of the satellite $\mathbf{x}_0, \dot{\mathbf{x}}_0$, empirical drag and solar radiation coefficients, $GM_{Moon}$, and gravity field coefficients. Those range partial derivatives that do not depend on parameters in the force model are computed analytically within RGODYN. These include station coordinates and Earth rotation parameters (ERPs). In principle the ERPs do affect the force model, since a correction to these parameters changes the orientation of the gravity field, and hence the acceleration on the satellite. However in practice the corrections are so small that the orientation change has negligible effect on the satellite.

### Partial derivatives of range with respect to parameters of the force model

We outline the calculation of the range partial derivatives with respect to one of the elements of the initial state vector of the satellite, as an example of the calculation of all partials with respect to parameters of the force model. The partial derivative of range with respect to element $x_0$ of the state vector is

$$\frac{\partial R}{\partial x_0} = \frac{\partial x}{\partial x_0}.\frac{\partial R}{\partial x} + \frac{\partial y}{\partial x_0}.\frac{\partial R}{\partial y} + \frac{\partial z}{\partial x_0}.\frac{\partial R}{\partial z} \tag{4.41}$$

Now from the integration of the variational equations, program ORBIT computes the partial derivatives of each element of the satellite rectangular coordinates with respect to each element of the initial state vector $\mathbf{x}_0, \dot{\mathbf{x}}_0$. Thus we need only compute in RGODYN the partial derivatives $\frac{\partial R}{\partial \mathbf{x}}$. From the basic range equation (4.40) by differentiation, we have for example

$$\frac{\partial R}{\partial x} = \frac{(x - x_{st})}{R},$$

and analogous values for $\frac{\partial R}{\partial y}$ and $\frac{\partial R}{\partial z}$. We can therefore evaluate (4.41), and similar equations for all parameters of interest.

### Partial derivatives of range with respect to non-force-model parameters

In this section, we outline the calculation of the range partial derivatives with respect to the tracking station coordinates and Earth rotation parameters.

#### Station Coordinates

The coordinates of the stations are expressed as longitude $\lambda$, geodetic latitude $\Phi$ and height $H$ with respect to an ellipsoid with $a_e = 6378137.0m$ and $1/f = 298.2570$. These coordinates are input to the program, and converted to geocentric rectangular coordinates $\mathbf{x}_g$, with magnitude $r$. In order to correct these initial values of the geodetic coordinates, we require the partial derivatives of range with respect to those coordinates. Now

$$\frac{\partial R}{\partial \lambda} = \frac{\partial R}{\partial x_g}.\frac{\partial x_g}{\partial \lambda} + \frac{\partial R}{\partial y_g}.\frac{\partial y_g}{\partial \lambda} + \frac{\partial R}{\partial z_g}.\frac{\partial z_g}{\partial \lambda} \tag{4.42}$$

and similarly for $\frac{\partial R}{\partial \Phi}$ and $\frac{\partial R}{\partial H}$.

Now ignoring the distinction between geodetic and geocentric latitude in the approximate calculation of the partials, we have

$$\begin{aligned} x_g &= r\cos\Phi\cos\lambda \\ y_g &= r\cos\Phi\sin\lambda \\ z_g &= r\sin\Phi \end{aligned}$$

Hence

$$\begin{aligned} \frac{\partial x_g}{\partial\lambda} &= -r\cos\Phi\sin\lambda \\ \frac{\partial y_g}{\partial\lambda} &= +r\cos\Phi\cos\lambda \\ \frac{\partial z_g}{\partial\lambda} &= 0 \end{aligned}$$

and

$$\begin{aligned} \frac{\partial x_g}{\partial\Phi} &= -r\cos\lambda\sin\Phi \\ \frac{\partial y_g}{\partial\Phi} &= -r\sin\lambda\sin\Phi \\ \frac{\partial z_g}{\partial\Phi} &= +r\cos\Phi \end{aligned}$$

and since

$$\frac{\partial \mathbf{x}_g}{\partial H} \equiv \frac{\partial \mathbf{x}_g}{\partial r},$$

$$\begin{aligned} \frac{\partial x_g}{\partial H} &= \frac{x_g}{r} \\ \frac{\partial y_g}{\partial H} &= \frac{y_g}{r} \\ \frac{\partial z_g}{\partial H} &= \frac{z_g}{r} \end{aligned}$$

We then require $\frac{\partial R}{\partial \mathbf{x}_g}$. We refer to equation (4.39), and for the calculation of partial derivatives ignore the small contribution from $\mathbf{x}_{tid}$. Then

$$\mathbf{x}_{st} = N^T P^T S^T \mathbf{x}_g, \tag{4.43}$$

or, abbreviated by replacing matrices $N^T$, $P^T$ and $S^T$ by their product matrix $A$,

$$\mathbf{x}_{st} = A\mathbf{x}_g, \tag{4.44}$$

Then from the range equation (4.40)

$$R = \left[(x - x_{st})^2 + (y - y_{st})^2 + (z - z_{st})^2\right]^{\frac{1}{2}},$$

we find by substitution from (4.44) for $\mathbf{x}_{st}$ and by partial differentiation,

$$\frac{\partial R}{\partial x_g} = \frac{1}{R}\left[-A(1,1)(x - x_{st}) - A(2,1)(y - y_{st}) - A(3,1)(z - z_{st})\right],$$

$$\frac{\partial R}{\partial y_g} = \frac{1}{R}\left[-A(1,2)(x - x_{st}) - A(2,2)(y - y_{st}) - A(3,2)(z - z_{st})\right]$$

and

$$\frac{\partial R}{\partial z_g} = \frac{1}{R}\left[-A(1,3)(x - x_{st}) - A(2,3)(y - y_{st}) - A(3,3)(z - z_{st})\right],$$

Then we have all the partial derivatives required to evaluate (4.42), and the equivalent expressions for the partial derivatives with respect to geodetic latitude $\Phi$ and height $H$.

### Measurement Bias

As we have seen, SLR observations consist of the measured two-way time of flight of the laser pulse, and an epoch of emission of the pulse. We considered in Chapter 3 the small system and energy dependent bias in the measured range that can occur if proper provision is not taken to avoid it. In addition to these small effects, there is always the potential for introduction of systematic bias due to some oversight, or failure to apply all known corrections to the raw data, or due to some undetected problem with a component of the ranging system. We thus wish to to be able to solve for range and epoch bias for a given set of data from a given station, and require partial derivatives of range with respect to these two parameters. For a range bias $R_b$, we have simply

$$\frac{\partial R}{\partial R_b} = 1.0$$

For a time bias, $T_b$, we use the predicted range iteration scheme outlined in section 4.3.2 to numerically estimate the change of satellite range with change of time of emission of the laser pulse at the station. This is a good estimate of the partial derivative $\frac{\partial R}{\partial T_b}$.

### Earth Rotation Parameters

We wish to calculate the partial derivatives of range with respect to the polar motion values $x_p$, $y_p$ and $UT1$. From equation (4.39) we take the matrix $S^T$, and since the polar motion values are always small ($x_p$, $y_p \leq 0.5$ arcsec), we make the approximations that $\cos x_p = 1$ and $\sin x_p = x_p$. Then $S$ becomes

$$S^T = \begin{bmatrix} \cos\Theta - x_p y_p \sin\Theta & -\sin\Theta & -x_p\cos\Theta - y_p\sin\Theta \\ \sin\Theta + x_p y_p \cos\Theta & \cos\Theta & -x_p\sin\Theta + y_p\cos\Theta \\ x_p & -y_p & 1 \end{bmatrix}$$

Then from equation (4.43) we have again $\mathbf{x}_{st}$, to place into the range equation (4.40), which may now be differentiated to form $\frac{\partial R}{\partial x_p}$, $\frac{\partial R}{\partial y_p}$ and $\frac{\partial R}{\partial \Theta}$. Since $\Theta$ is a function of UT1, we shall use the partial derivative of range with respect to $\Theta$ to solve for corrections to the initial series of values of UT1-UTC.

## 4.4 Conclusion

We have outlined the computation of the predicted orbit of the satellite, and the predicted range from the observing stations, which may be directly compared to the measured range. We have formed the partial derivatives of range with respect to both force-model and 'geodetic' parameters, and can thus form the observational equations (4.38). The parameters of interest can be chosen at run time from the full set for which partial derivatives have been computed. From the final set of observational equations we form the normal equations, and hence parameter corrections and their standard errors. The solution is iterated until convergence is obtained, as measured by no further significant change to any of the parameters.

In the next Chapter we describe our use of the package to carry out first a preliminary analysis of SLR observations of the two Etalon satellites, followed by long-arc solutions.

# Chapter 5

# Orbit Determination of the Etalon Satellites.

## 5.1 Introduction.

In previous Chapters we have considered in detail the technique of Satellite Laser Ranging, with particular emphasis on the single-photon system at Herstmonceux. We have used experimental results and models to derive centre-of-mass corrections for Lageos and Etalon appropriate to the single-photon level of return, and we have also considered potential return-level-dependent bias in the range measurements. We have discussed the SLR analysis package developed at the Royal Greenwich Observatory, which is used to fit orbits to the range observations from the stations in the international network.

In this and subsequent Chapters, we carry out an extended analysis of such observations of the two Etalon geodetic satellites. Our goal is to determine their usefulness in a variety of potential applications, including long-term maintenance of the terrestrial reference frame, evaluation of and comparison with Lageos of non-gravitational perturbations and possible corrections to selected terms in the expansion of the Earth's gravity field. We begin this work with a preliminary analysis of a few month's observations, and move on to determine long-arc orbits by fitting to 2.5 years of range measurements.

## 5.2 Preliminary Analysis.

As a starting point for this work we undertook to assess the potential use of the data, in particular to compute station coordinates and Earth rotation parameters and to compare the results from the two satellites. We used Etalon quicklook normal points for the period 1992 June 1 to November 30. The initial station coordinates and velocities were taken from ITRF93 and were used to form a set of station coordinates for epoch 1993.0. The Earth rotation parameters were taken from the IERS Bulletin B 5-day series. The average number of normal points obtained each month was about 600, compared to about 6000 which are regularly obtained from the Lageos satellites. Hence longer orbital arcs were used to improve the stability of the solutions. The strategy adopted was to use two independent arcs of duration 90 days. Within each orbital arc we estimate the initial state vector of the satellite, a single coefficient of solar radiation pressure, an empirical along-track acceleration, corrections to the station coordinates at epoch 1993.0, and corrections at 10-day intervals to the IERS Earth rotation parameters. In such a solution where we solve for station coordinates and ERPs there are 3 unconstrained degrees of freedom, namely rotations about the Earth-fixed x, y and z-axes. The arbitrary origin of station longitudes is responsible for the degree of freedom about the z-axis, since a small change to all the longitudes of the tracking stations or a constant correction to the series of UT1-UTC values would in the dynamical adjustment be accommodated by an opposite rotation of the orbital plane of the satellite. Similarly, constant changes to the components of the polar motion series, equivalent to rotations about the y and x axes, would be accommodated by changes to the latitude and longitude of the stations. To constrain an otherwise singular solution, we adopted the method of Smith *et al* [38], namely to fix at their a-priori values the longitude and latitude of one station and the latitude of a second station separated in longitude from the first by about $90^o$. We chose to fix in this way the coordinates of Herstmonceux, UK (station 7840) and Greenbelt, USA (7105).

The rms of the post-fit residuals for the 90–day arcs for each satellite varied between 10-15 cm. At the final iteration of each solution the normal matrix was saved, and the individual arcs were combined using the Helmert–Wolf technique [50] in a solution for the station coordinates. This was done separately for each satellite. In this way, two sets

of station coordinates for epoch 1993.0 were formed. There were 11 stations in common to both the Etalon data.

### 5.2.1 Station Coordinate Solutions.

We compared the two sets of geocentric rectangular station coordinates to detect possible satellite-dependent systematic biases, and also compared them to the a-priori ITRF93 set. In each comparison, we used pairs of station coordinates to solve for the coefficients of a rigid- body mapping of one set onto the other. The parameters solved-for in the adjustment were three orthogonal translations, three orthogonal rotations and a scale factor. We found that in all cases the parameters describing the rotations of one set of coordinates onto the other and the scale factor were insignificant. Displacements in the X and Y directions are also small. The largest displacement, that in the z direction between the results from the two Etalons, $\Delta z = 4.52 \pm 4.05$ cm, is fairly large, but also poorly determined.

### 5.2.2 Solutions for UT1-UTC.

Analysis of SLR data does not give an absolute value of UT1-UTC since there is no precise link between the dynamical reference frame defined by the satellite orbit and the inertial stellar reference frame. However in our analysis the first two values in the series of UT1-UTC are held fixed at the IERS Bulletin B values, and continuity between the two orbital arcs is ensured by fixing the first value of UT1-UTC of the second arc to that derived from the first arc. Additionally we may expect to see a secular departure of our series from that deduced with reference to an inertial stellar reference frame due to unmodelled forces acting on the node of the satellite's orbit, in particular errors in the zonal terms of the gravity field and the effect of $\dot{J}_2$ [31], although in the recent JGM gravity field models, a model for this effect has been included. We also expect that the Etalon satellites would be affected less than Lageos by such gravity-field effects, because of their greater height. The two series of corrections to the IERS UT1-UTC values deduced from the Etalon analyses are presented in Figure 5.1.

The results show a clear systematic feature of semi-amplitude about 1 ms. This signature is much clearer and less noisy in the results from Etalon-I than from Etalon-II.

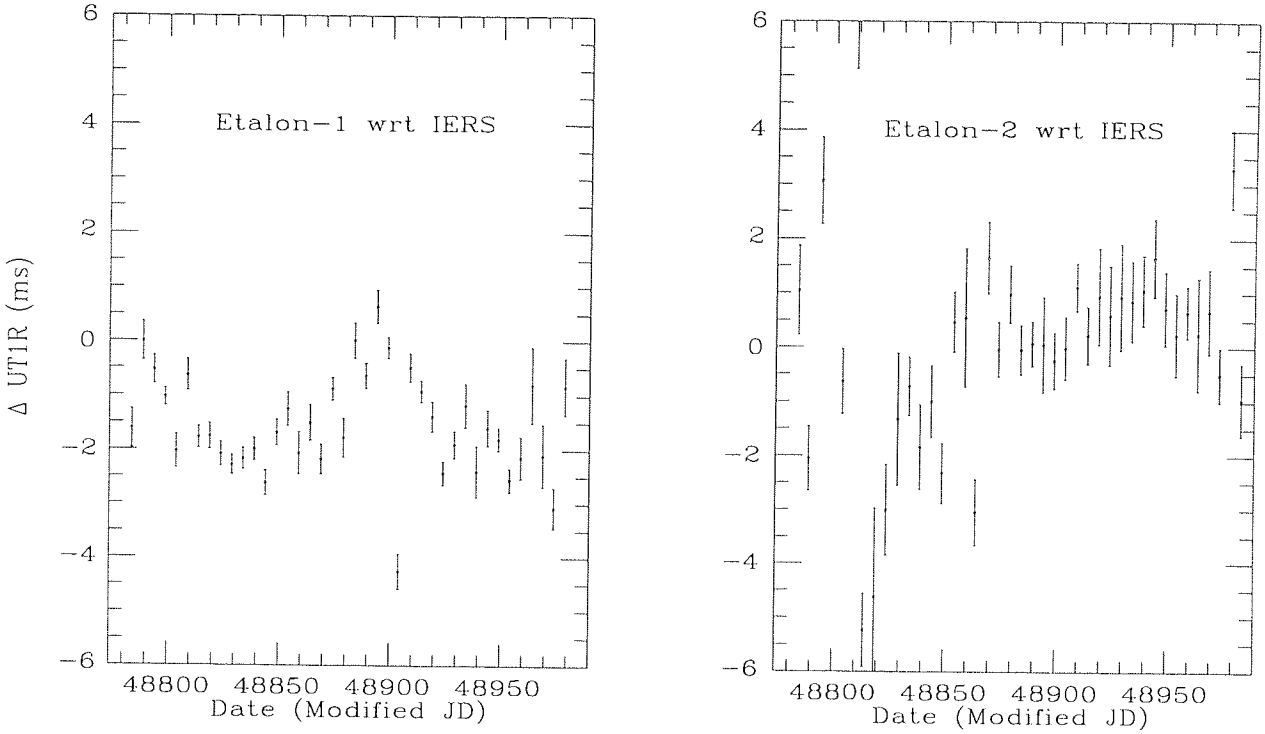


Figure 5.1: Differences between UT1-UTC derived from Etalon analyses and IERS values.

However, there is little evidence in the results from either satellite of any secular run-off of values over the 6-month period with respect to the IERS results, which suggests that the Etalon data may be useful in defining a stable reference frame for Earth rotation studies.

### 5.2.3 Conclusions

The results of this short preliminary investigation into the Etalon data may be summarised as follows. The differences between the two sets of station coordinates are rather large, particularly in the z-component, possibly because only a limited number of stations routinely track the satellites. The derived values of UT1-UTC show significant systematic signatures, which are clearer in the Etalon-I results. However there is little evidence of secular run-off of the values with respect to the IERS results. The conclusion is that a longer period of data should be analysed, with the specific aim of determining a stronger terrestrial reference frame, and making a better determination of the signatures in the deduced series of UT1–UTC, with a view to explaining the systematic behaviour. We also wish to use the long–arc solution to solve for the coordinates of some stations

which only occasionally track the satellites.

Since the systematic variation in the values of UT1-UTC appears to have a period of several months, we decided that analysis of at least 2 years of tracking data for each satellite would be required for a good determination. In fact we took 900 days of data from 1992 June 1 to 1994 December 31. In order partly to overcome the potential problems for continuity of reference frame of sparsity of tracking data if the analyses were carried out over short (few months) orbital arcs, we further decided to fit the entire 2.5 year sets of data with single orbits. We also wish to use the data to solve for corrections to some of the coefficients of the gravity field and to check whether we can determine a significant correction to the IERS(92) value of $GM_{Moon}$.

## 5.3 Orbital Characteristics of the Etalon Satellites.

As a preliminary stage to the long–arc analysis, we consider some of the objectives for the use of the Etalon tracking data defined by Dunaev and Tatevian [3] in particular for the determination of low order terms in the Earth's gravity field, and for improvement of the value of $GM_{Moon}$.

The orbital periods of the satellites are 11.25 hours, close to half the rotational period of the Earth (23.97 hours). We may therefore expect there to be some conditions of resonance of the orbital period with low degree and order terms in the gravity field, analysis of which might indicate which terms principally effect the motions of the satellites and thus would be most readily recoverable from the tracking data. This analysis has recently been carried out by Lucchesi and Nobili [51], who used the approach of Kaula [52] to show that the main resonant terms are $J_{3,2}$, $J_{2,2}$, $J_{4,4}$, $J_{5,2}$, and $J_{6,4}$, where the $J_{l,m}$ are the magnitudes of the harmonic coefficients $C_{l,m}$ and $S_{l,m}$ in the expansion of the geopotential. (see Chapter 4)

We now look at the effects of luni-solar perturbations on the long-term dynamical evolution of the node and inclination of the 2 satellites, using the work by Sinclair [53] on the motions of the satellites of Mars. This work on the behaviour of the Etalons was summarised in Appleby [54].

We used SLR observations of the Etalons to compute a precise continuous orbit for

each satellite by fitting to 180 days of data for the period 1992 June 1 to 1992 November 30. The initial conditions at epoch 1992 June 1 were taken from the 90-day orbits used in the preliminary analysis discussed in section 5.2 above. As before we solved for corrections to the initial state vector, and for a single along–track empirical acceleration and solar radiation coefficient. The station coordinates were held fixed at the ITRF93 values, and we used Earth rotation parameters taken from the IERS Bulletin B series. Post fit residual rms values were near 50 cm for each satellite. To extend the orbits to beyond a year, essential for an investigation into luni-solar perturbations, we simply ran the integrations ahead by a further 200 days, without a further fit to observations. Geocentric rectangular coordinates and velocities were output at 120 minute intervals in the J2000 reference frame. The coordinates were converted to instantaneous orbital elements using the procedure outlined in Appendix A.

### 5.3.1 Evolution of $I$ and $\Omega$

Using this procedure, we converted our 400–day series of geocentric vectors to osculating orbital elements. The resulting values of $I$ and $\Omega$ are plotted in Figure 5.2. To obtain a reasonable scale for plotting the $\Omega$ values, we have subtracted from the values of $\Omega$ for each satellite the linear terms $3.305 \times 10^{-2}\text{day}^{-1}$

Several periodic features are evident in the plots. The very fine structure is a periodic variation of the elements with half the orbital period (340 minutes), which is caused by the oblateness of the Earth. The 14-day and 6-month periods are the well-known luni-solar perturbations. The interesting feature of the plots is the different overall slopes between the values of the Etalon-I and Etalon-II elements. These slopes are due to the so-called secular perturbations of the orbits by the oblateness, the Moon and the Sun, as investigated for the satellites of Mars by Sinclair [53]. The secular perturbations due to the Earth's oblateness cause the orbital plane to precess around the equator, while remaining at a constant mean inclination to the equator. However, the secular effects of the Moon and Sun cause the satellite orbital plane to precess around the plane defined by the instantaneous mean of the lunar and solar orbital planes, and retain a constant inclination to this mean plane. The combined effect is that the inclination of the satellite orbital plane to the equator will not be constant and the nodal precession rate will vary,

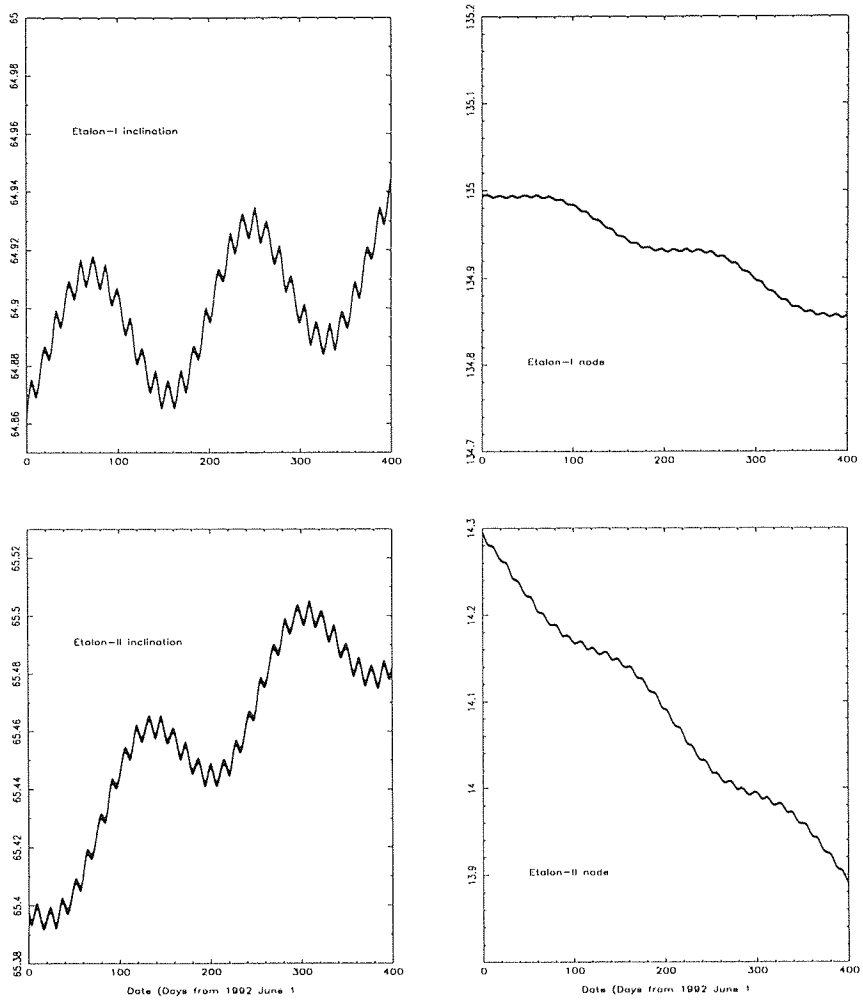


Figure 5.2: Etalon Orbital Elements evolution

the variations being of a size depending upon the relative sizes of the lunar and solar effects to that of the Earth's oblateness. The effects would be expected to be different for the two satellites, which are in different orbital planes, and thus in different configurations with respect to the orbital planes of the Sun and Moon.

Such a prominent signature in the orbits of the satellites due to the Lunar perturbations lends strength to the proposal that long-term tracking of these satellites could lead to a good determination of the lunar gravitational constant.

## 5.4 Long–Arc Orbit Determination.

Using the initial state vector $x_0$, $\dot{x}_0$ derived from the 180 day fits discussed in Sections 5.2, we attempted to fit continuous orbits to the 2.5 year data sets by gradually increasing the time span over which the fits were carried out. Initially we again solved for a limited

parameter set; initial state vector, empirical along–track acceleration and single solar radiation coefficient. Station coordinates and velocities were taken as before from ITRF93 and the Earth rotation parameters from IERS Bulletin B. Convergence with post fit residual rms of size about 50cm was achieved for arc lengths of up to about 250 days. Upon increasing this time span to 300 days, fairly large corrections of several meters and m $sec^{-1}$ to the initial conditions were indicated by the analysis program RGODYN, but the predicted post–fit rms remained small. These corrections were applied and the integration repeated, but the fit of the data to the orbit was found to be worse than for the previous iteration. Large systematic variations in the sizes of the post-fit residuals were seen.

Such behaviour indicated that there existed either an error or important omission in the force model or in the computation of the partial derivatives, such that the indicated corrections to the parameters were erroneous. It was considered unlikely that any large error should exist in the force model, since a very acceptable fit to the observations had been achieved up to the 250 days, and any deficiency, for example the lack of a complete non-gravitational force model, would tend to be absorbed into the empirical along–track acceleration parameter. Thus a series of experiments was undertaken to check the accuracy of the partial derivatives. We first replaced the partial derivatives with those computed by a finite difference scheme, and repeated the 300-day fits, as follows.

### 5.4.1 Accuracy of Partial Derivatives

The instantaneous position of the satellite, $x, y, z$, may be considered to be a non–linear function of the initial state vector $\mathbf{x_0}, \dot{\mathbf{x}}_\mathbf{0}$ and of a series of force model parameters $\mathbf{p}$. Expressed in full for the x component, we can write

$$x = f(x_0, y_0, z_0, \dot{x}_0, \dot{y}_0, \dot{z}_0, \mathbf{p})$$

If we apply a small increment $h$ to one of the arguments of $f$, then by Taylor series expansion,

$$f(x_0+h, y_0, z_0, \dot{x}_0, \dot{y}_0, \dot{z}_0, \mathbf{p}) = f(x_0, y_0, z_0, \dot{x}_0, \dot{y}_0, \dot{z}_0, \mathbf{p}) + \frac{h\partial x}{\partial x_0} + ... + \frac{h^n}{n!} \times \frac{\partial^n x}{\partial x_0} + ...$$

So to first order,

$$\frac{\partial x}{\partial x_0} = \frac{f(x_0+h, y_0, ...) - f(x_0, y_0, ...)}{h}$$

Thus in order to compute by finite differences the matrix of partial derivatives $\frac{\partial \mathbf{x}}{\partial param}$ for the eight parameters $\mathbf{x_0}$, $\dot{\mathbf{x}_0}$, empirical along–track acceleration and solar radiation coefficients, we must run the integration procedure an additional 8 times for each iteration step, where we increment in turn each of the initial conditions. Some care was taken with the choice of the values of the increment for each parameter, it being found that the ideal situation for maximum stability in the subsequent solutions was for the increments to be such that their effect on $\mathbf{x}$ was similar for all the parameters. By experiment we chose increments of 1m to $\mathbf{x_0}$, 1 m sec$^{-1}$ to $\dot{\mathbf{x}}_0$, $1.0 \times 10^{-14}$m sec$^{-1}$ to the empirical acceleration and 0.05 to the coefficient of solar radiation.

A scheme was developed whereby an initial integration was carried out using the current best set of initial conditions, followed automatically by a series of 8 additional incremented integrations. A final step computed the 24 partial derivatives $\frac{\partial \mathbf{x}}{\partial \mathbf{x_0}}$, $\frac{\partial \mathbf{x}}{\partial \dot{\mathbf{x}}_0}$, $\frac{\partial \mathbf{x}}{\partial accel}$ and $\frac{\partial \mathbf{x}}{\partial solrad}$ from the finite difference formula and placed their values in their correct locations in the initial ephemeris file.

In this way a 300–day arc for Etalon–1 was computed and compared to the range data. The solution was found to converge after 3 iterations with a post–fit rms of 65 cm. This clearly demonstrated that the previous lack of convergence had been due to a problem with the partial derivatives computed from the variational equations. However, despite the automation developed to carry out the iteration procedure, the scheme was time consuming and laborious, and would have become impossibly so with the intended expansion of the parameter set. Thus having identified the cause of the earlier lack of convergence, we decided to investigate the apparent problem with the partial derivative computation.

During the process of replacing the integrated partial derivatives with the finite difference ones, we also computed and saved their differences. A plot showing values of

$\frac{\partial x}{\partial x_0}$ computed from both methods, and the difference between them, is shown for a time span of 300–days in figure 5.3. The figure shows in the top plot the values of the partial derivatives computed by the finite–difference scheme (FD), in the centre plot the partials computed by integrating the variational equations, and the bottom plot gives the difference between them, equivalent to the error in the integrated values.

The agreement between the two sets of partial derivatives is good for the first 50 days, but there is a subsequent rapid increase in the differences. On the assumption that the finite difference values are correct, after 120 days the integrated partials are in error by a factor of 2, and after the 300 days by a factor of 5. Similar errors were seen in all the partial derivatives.

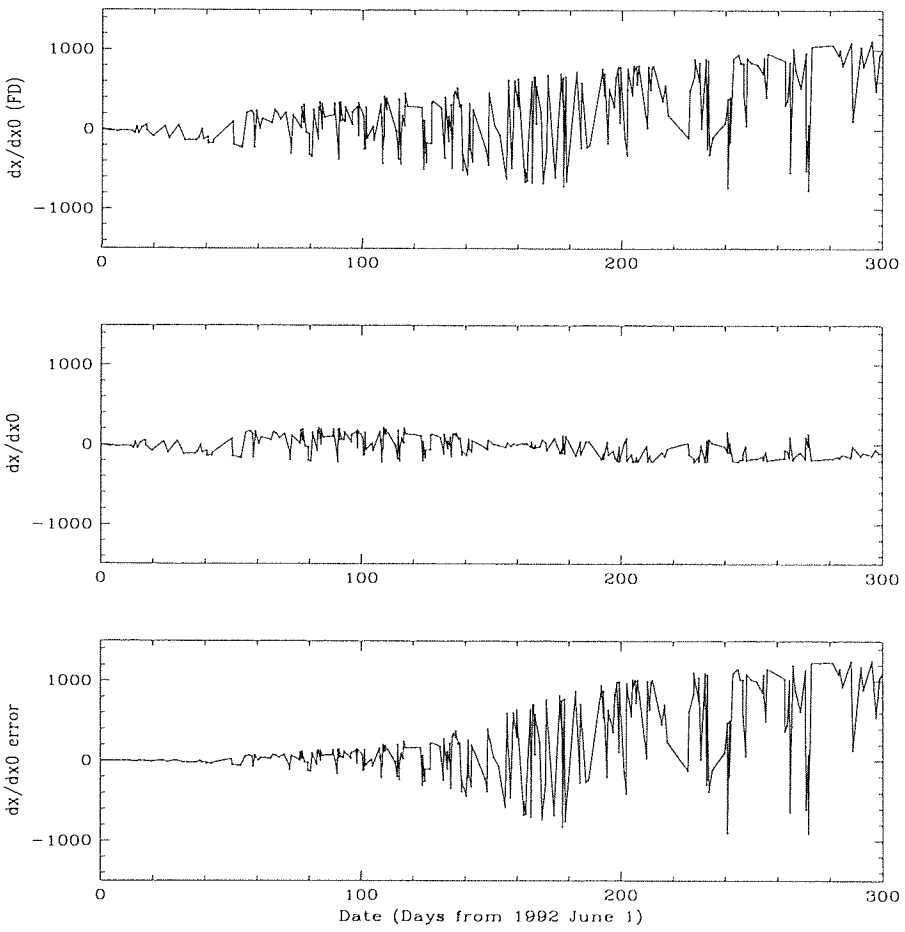


Figure 5.3: Partial Derivatives from integration and finite-diffs.

We carried out an investigation to determine the source of error in the computation

of the partial derivatives within the ORBIT program. To recap on the description of the partial derivatives given in Chapter 4, we look more closely at the computations. In order to solve for corrections to initial estimates of a parameter $p$, we need to compute $\frac{\partial x_i}{\partial p}$, for $i = 1, 2, 3$ at each step of the integration. Now

$$\frac{d^2}{dt^2}\left(\frac{\partial x_i}{\partial p}\right) = \frac{\partial F_i}{\partial p} + \sum_{j=1}^{3} \frac{\partial F_i}{\partial x_j}\frac{\partial x_j}{\partial p}, \tag{5.1}$$

where the first term is the explicit partial derivative of the satellite acceleration with respect to the parameter $p$. The explicit partial derivative is zero when $p$ is one of the components of $\mathbf{x}_0$ or $\dot{\mathbf{x}}_0$, since $\ddot{\mathbf{x}}$ does not depend explicitly upon the initial position and velocity of the satellite. This system of second order differential equations is called the system of variational equations, and is integrated along with the 3 differential equations of motion of the satellite. However, we need not evaluate the variational equations to high accuracy, since we are linearizing a non–linear system and assuming that the initial estimates of the parameters are close to the true values, such that convergence is fairly rapid. It is common therefore in the interests of speed of computation to restrict the force model used in the variational equations to just the major terms, and inspection of the coding showed that the part of the force model used for the variational equations contained the central force and a restricted set of zonal and tesseral terms of the gravity field. That is

$$\ddot{\mathbf{x}} = -GM\frac{\mathbf{x}}{r^3} + \text{gravity field terms} \tag{5.2}$$

This approximation has proved entirely adequate for arcs of up to 30 days, the usual length of Lageos arcs for example, and appears from the above comparisons to be a good approximation for up to about 50 days, but is clearly causing problems in the current long–arc work. The major forces that have been left out of the model are 3rd–body (Sun and Moon) gravitational attractions, and the non–gravitational forces of along-track acceleration and solar radiation pressure.

To test the relative sensitivity of these forces on the calculation of the partial derivatives, we suppressed each in turn from the force model used in the integration of the equations of motion. We again computed partial derivatives by finite differences, and compared them to the integrated values. Suppression in the force model of the non–

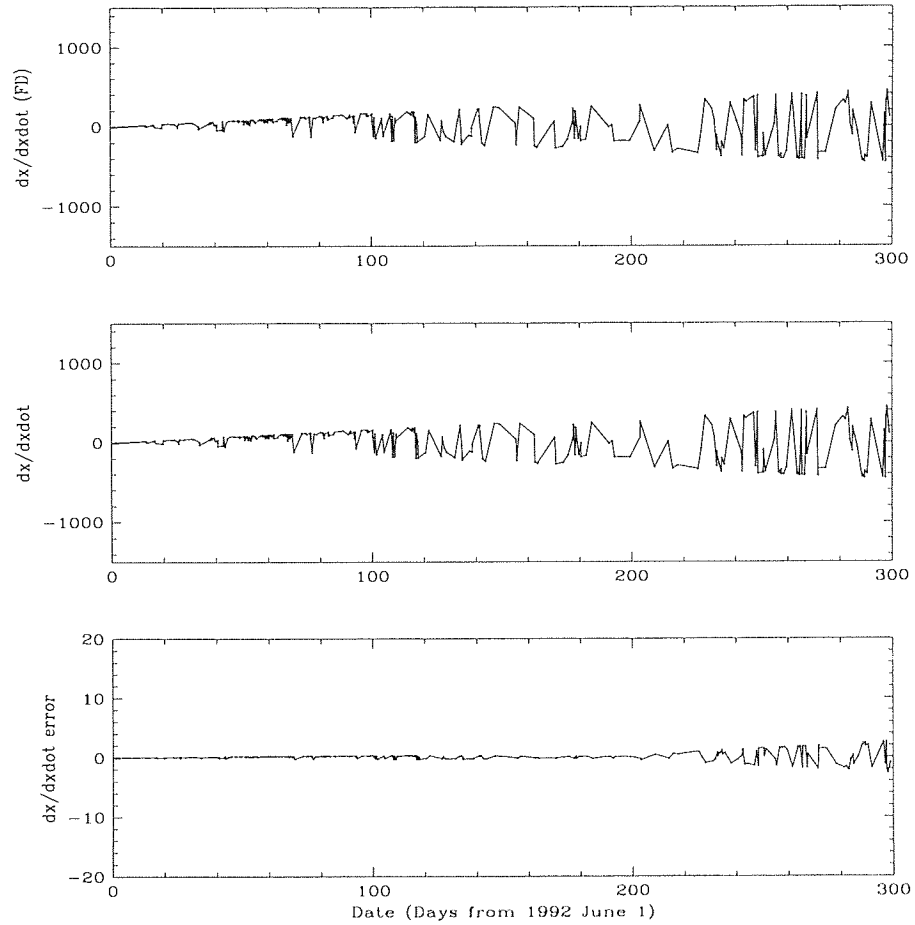


Figure 5.4: Partial Derivatives with restricted force model.

gravitational forces had little effect on the integrated partial derivatives; they were still very different from the 'correct' finite difference values. However by removing the Luni-Solar 3rd body attractions from the force model, the integrated partials agreed almost exactly with their equivalent finite difference values, over the entire 300-day span. A plot of the comparisons for 1 particular partial derivative $\frac{\partial x}{\partial \dot{x}_0}$ is shown in Figure 5.4, where the plot of the errors is now given on a greatly expanded scale.

### 5.4.2 Improvement of Force Model for Partial Derivatives

We now wish to add the luni-solar third body attractions to the variational equations to improve the accuracy of the partial derivatives. We look at the implementation of the equations as they currently appear in program ORBIT. Expanding equation (5.1) for a

coordinate $x_i$ where $\ddot{\mathbf{x}}$ is the central force term given by equation (5.2), and considering the parameter $p$ to be one of $\mathbf{x}_0$ or $\dot{\mathbf{x}}_0$, so that the explicit partial $\frac{\partial \ddot{x}_i}{\partial p}$ is zero, we have

$$\frac{d^2}{dt^2}\left(\frac{\partial x_i}{\partial p}\right) = \sum_{j=1}^{3} \frac{\partial}{\partial x_j}\left(\frac{-GMx_i}{r^3}\right)\frac{\partial x_j}{\partial p},$$

So for all $i$,

$$\frac{d^2}{dt^2}\left(\frac{\partial x_i}{\partial p}\right) = \frac{GM}{r^3}\sum_{j=1}^{3}\left(\frac{3x_i x_j}{r^2} - \delta_{ij}\right)\frac{\partial x_j}{\partial p},$$

where

$$\delta_{ij} = \begin{cases} 1 & \text{for } i = j \\ 0 & \text{for } i \neq j \end{cases}$$

This is the form in which the variational equations are programmed. We are now in a position to add the Luni–Solar perturbations to the truncated force model of equation (5.2). From the explanation in Chapter 4 of the 3rd body attractions, equation (5.2) then becomes

$$\ddot{\mathbf{x}}_\mathbf{i} = \frac{-GMx_i}{r^3} - GM_\odot\left(\frac{x_i - x_{is}}{\Delta_s^3} + \frac{x_{is}}{r_s^3}\right) - GM_\bullet\left(\frac{x_i - x_{im}}{\Delta_m^3} + \frac{x_{im}}{r_m^3}\right), \tag{5.3}$$

where $\mathbf{x}_s = (x_{1s}, x_{2s}, x_{3s})$ and $\mathbf{x}_m = (x_{1m}, x_{2m}, x_{3m})$ are the geocentric vectors of the Sun and Moon, with moduli $r_s$ and $r_m$, and $\Delta_s$ and $\Delta_m$ are the moduli of the vectors $\mathbf{x} - \mathbf{x}_s$ and $\mathbf{x} - \mathbf{x}_m$.

The coding was tested as before by computing partial derivatives by the finite difference method, and comparing them to the integrated values, over the time span of 300 days.

A plot showing the two sets of values of $\frac{\partial x}{\partial x_0}$ and their differences is given in figure 5.5, where now of course we are using the full force model in the integration of the equations of motion. The agreement is now very good, confirming the source of the initial discrepancy and its correct resolution.

We are now in a position to generate 2.5 year orbits and compare them to observations.

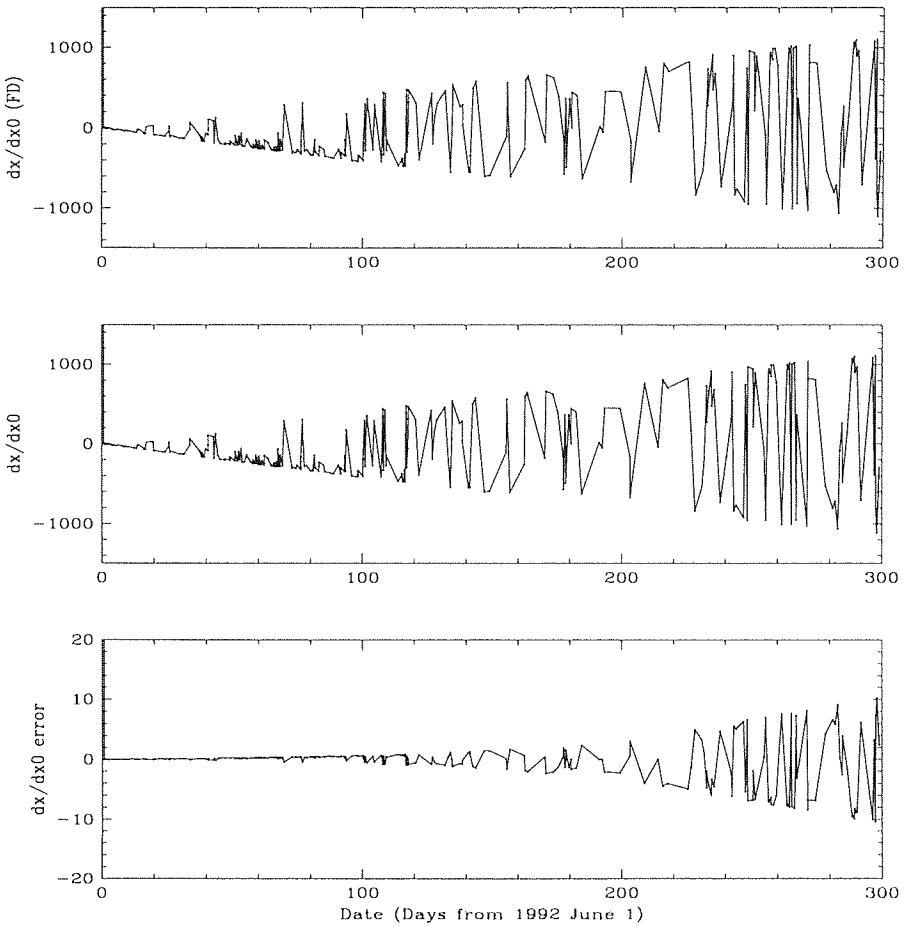


Figure 5.5: Partial Derivatives with full force model.

## 5.5 Long–Arc Solutions.

We fitted initial long arc orbits to 900 days of observations for each satellite, starting from the values of the state vectors determined from the 200–day fits, that is beginning on 1992 June 1. System dependent values for the centre-of-mass corrections were used as discussed in Chapter 3. For SPAD systems we use CoM = 582 mm and for MCP and PMT systems we use CoM = 612 mm. Table 5.1 lists the stations involved in tracking the satellites during the 900 days and includes the detector types and the number of normal points used for each satellite. For some of the stations we do not have reliable coordinates, and for a few stations the data appeared to contain range biases. At this stage in the analysis, the observations from these problem stations were not used. These stations are marked with a $\star$ in the detector column of the Table.

One of the aims of the analysis is to determine a consistent set of tracking station coordinates for all the stations, and we will at that stage attempt to include these stations, and investigate the range biases.

Initially we adjust only the satellite state vector, a coefficient of empirical along–track acceleration and a solar radiation coefficient. This is in order not to over-parameterise the solution until we are able to quantify possible model errors and seek to improve them. The post–fit residual rms values for each satellite are shown in Table 5.2.

It is interesting to note that the orbital fit is much better for Etalon-II than for Etalon-I, and that there is a significant difference between the solar radiation coefficients for the two nominally–identical satellites. For a spherical satellite, the solar radiation coefficient $C_R$ is related to the diffuse albedo $\gamma_D$ by

$$C_R = 1 + \frac{4}{9}\gamma_D$$

The values of $C_R$ in Table 5.2 imply that for Etalon-1 $\gamma_D = 0.56$ and for Etalon-2 $\gamma_D = 0.65$, a difference of nearly 15% in the reflective properties of the two satellites.

The post–fit range residuals for each satellite show systematic departures from the best–fit orbit of up to 5 meters, and carry information on the deficiencies in the force model, such as possible errors in and variations of the coefficients of the gravity field, unmodelled non–gravitational forces, tracking station coordinate and systematic errors, and errors in the a-priori Earth rotation parameters.

### 5.5.1 Solutions for corrections to long-arc orbit

As a guide to identifying the force–model errors, we wish to use the residuals from the long arc solution to solve for corrections to the instantaneous orbital elements of that long–arc. We will solve for such corrections over intervals of a few days, and thus effectively form corrections to the mean elements over that interval, with a subsequent loss of short–period information. We set up the following equation of condition to solve for corrections to the mean values of those elements within each interval.

$$\frac{\partial R}{\partial \mathbf{e}} \Delta e = \Delta R + \epsilon \tag{5.4}$$

where $R$ is the topocentric range to the satellite at the observational instant, $\Delta R$

| Station | Name | Det | Numb Et-I | Numb Et-II | Longitude Degs | Latitude Degs | Height m |
|---|---|---|---|---|---|---|---|
| 1863 | Maidan-I | pmt * | 64 | 60 | 66.9431809 | 38.6857557 | 2713.782 |
| 1864 | Maidan-II | pmt * | 220 | 204 | 66.9431790 | 38.6848939 | 2713.655 |
| 1869 | Balkhash | pmt * | 23 | 0 | 66.9431715 | 38.6857267 | 2713.243 |
| 1873 | Simeiz | pmt | 13 | 0 | 33.9910412 | 44.4131863 | 364.659 |
| 1884 | Riga | pmt * | 7 | 0 | 24.0591628 | 56.9485492 | 31.099 |
| 1893 | Katzively | pmt | 40 | 91 | 33.9702131 | 44.3931729 | 68.431 |
| 7080 | Mcdonald | mcp | 271 | 208 | 255.9848968 | 30.6802669 | 2004.320 |
| 7090 | Yarragad | mcp | 2701 | 2719 | 115.3468381 | -29.0464997 | 241.245 |
| 7105 | Greenbelt | mcp | 417 | 481 | 283.1723998 | 39.0206047 | 19.252 |
| 7109 | Quincy | mcp | 770 | 339 | 239.0553953 | 39.9750010 | 1106.443 |
| 7110 | Mon. P. | mcp | 1673 | 1347 | 243.5774242 | 32.8917373 | 1839.073 |
| 7210 | Haleakala | mcp | 515 | 555 | 203.7441818 | 20.7072172 | 3067.583 |
| 7237 | Changchun | pmt * | 191 | 166 | 125.4435458 | 43.7905091 | 275.019 |
| 7403 | Arequipa | mcp | 2 | 5 | 288.5071349 | -16.4657174 | 2488.859 |
| 7502 | Sutherland | pmt * | 72 | 29 | 20.8030761 | -32.3784666 | 1728.628 |
| 7805 | Metsahovi | pmt | 11 | 10 | 24.3946407 | 60.2173074 | 78.228 |
| 7835 | Grasse | pmt | 26 | 2 | 6.9212158 | 43.7546933 | 1322.980 |
| 7837 | Shanghai | pmt | 64 | 57 | 121.1918325 | 31.0975420 | 27.957 |
| 7839 | Graz | spa | 604 | 540 | 15.4934521 | 47.0671348 | 539.455 |
| 7840 | Herstmon. | spa | 640 | 590 | 0.3362139 | 50.8673799 | 75.441 |
| 7843 | Orroral | mcp | 471 | 509 | 148.9394033 | -35.6362538 | 1349.865 |
| 8834 | Wettzell | spa * | 734 | 606 | 12.8781050 | 49.1444151 | 664.891 |

Table 5.1: Etalon Tracking Stations. Those marked $\star$ not at present used in analysis.

| Satellite | Number | rms | Drag | Solrad |
|---|---|---|---|---|
| | | m | pm $s^{-2}$ | |
| Etalon-I | 8205 | 2.80 | 0.138 ±0.002 | 1.252 ±0.001 |
| Etalon-II | 7466 | 1.18 | 0.102 ±0.002 | 1.289 ±0.001 |

Table 5.2: Statistics of long–arc solutions.

is the residual of the SLR range observation from the long–arc solution, $\epsilon$ is the least–squares residual that we wish to minimise, and $\mathbf{e}$ is the vector of orbital elements, $\mathbf{e} = (a, e, I, M + \omega, \omega, \Omega)$. We choose the linear combination $M + \omega$ because for small $e$, $M$ is ill–defined. Values of $\mathbf{e}$ are computed at each observational instant by the procedure detailed in Appendix A.

Now,

$$\frac{\partial R}{\partial \mathbf{e}} = \frac{\partial R}{\partial x_1}\frac{\partial x_1}{\partial \mathbf{e}} + \frac{\partial R}{\partial x_2}\frac{\partial x_2}{\partial \mathbf{e}} + \frac{\partial R}{\partial x_3}\frac{\partial x_3}{\partial \mathbf{e}}$$

And $R = \mid \mathbf{x_T} \mid$, where $\mathbf{x_T} = \mathbf{x} - \mathbf{x_s}$, where $\mathbf{x_s}$ is the geocentric vector to the observing station, and as before $\mathbf{x}$ is the satellite geocentric vector. So in full

$$R = \left((x_1 - x_{s1})^2 + (x_2 - x_{s2})^2 + (x_3 - x_{s3})^2\right)^{\frac{1}{2}}$$

So

$$\frac{\partial R}{\partial x_1} = \frac{(x_1 - x_{s1})}{R} = \frac{x_{T1}}{R}$$

and similarly for $\frac{\partial R}{\partial x_2}$ and $\frac{\partial R}{\partial x_3}$

Now the instantaneous coordinates of the satellite $\mathbf{x}$ are related to the orbital elements by

$$\mathbf{x} = r\mathbf{A},$$

where

$$r = a(1 - e\cos E),$$

and

$$\mathbf{A} = \begin{pmatrix} \cos u \cos\Omega & - & \cos I \sin u \sin\Omega \\ \cos u \sin\Omega & + & \cos I \sin u \cos\Omega \\ \sin I \sin u & & \end{pmatrix},$$

where $E$ is the eccentric anomaly and $u$, the argument of latitude is close to $M+\omega$ for small $e$

So for example,

$$x_1 \simeq a(1-e\cos E)(\cos(M+\omega)\cos\Omega - \cos I \sin(M+\omega)\sin\Omega) \tag{5.5}$$

So, again for example,

$$\frac{\partial x_1}{\partial I} \simeq a(1-e\cos E)[\sin I \sin(M+\omega)\sin\Omega],$$

or,

$$\frac{\partial x_1}{\partial I} \simeq \sin\Omega \times x_3$$

And

$$\frac{\partial x_1}{\partial \Omega} \simeq a(1-e\cos E)[-\cos(M+\omega)\sin\Omega - \cos I \sin(M+\omega)\cos\Omega]$$

or,

$$\frac{\partial x_1}{\partial \Omega} \simeq -x_2$$

To calculate $\frac{\partial x_1}{\partial(M+\omega)}$, we have to take into account that $E$ is related to $M$ through Kepler's equation $E = M + e\sin E$. So extracting from equation (5.5) $r = a(1-e\cos E)$, then

$$\frac{\partial r}{\partial(M+\omega)} = +ae\sin E \frac{\partial E}{\partial(M+\omega)},$$

and by differentiating Kepler's equation

$$\frac{\partial E}{\partial(M+\omega)} - e\cos E \frac{\partial E}{\partial(M+\omega)} = 1$$

Therefore

$$\frac{\partial E}{\partial(M+\omega)} = \frac{1}{(1-e\cos E)},$$

and

$$\frac{\partial r}{\partial(M+\omega)} = \frac{+ae\sin E}{(1-e\cos E)} \tag{5.6}$$

So by differentiating (5.5) and using (5.6), we have

$$\frac{\partial x_1}{\partial(M+\omega)} = \frac{-ae\sin E}{(1-e\cos E)}[-cos(M+\omega)\cos\Omega + \cos I \sin(M+\omega)\sin\Omega]$$

$$+ a(1-e\cos E)[-sin(M+\omega)\cos\Omega - \cos I \cos(M+\omega)\sin\Omega]$$

### 5.5.2 Solutions for orbital elements.

By experimentation we found that about 25 days is the shortest interval of time that will 'support' the solutions, this being dependent on the numbers of observations within the intervals throughout the 2.5 year orbital solution. We thus partition the range residuals into intervals of 25 days and for each observational instant we convert the satellite geocentric coordinates and velocities $\mathbf{x}$, $\dot{\mathbf{x}}$ to osculating elements as described in Appendix A. We then set up the equation of condition (5.4), and carry out the solutions.

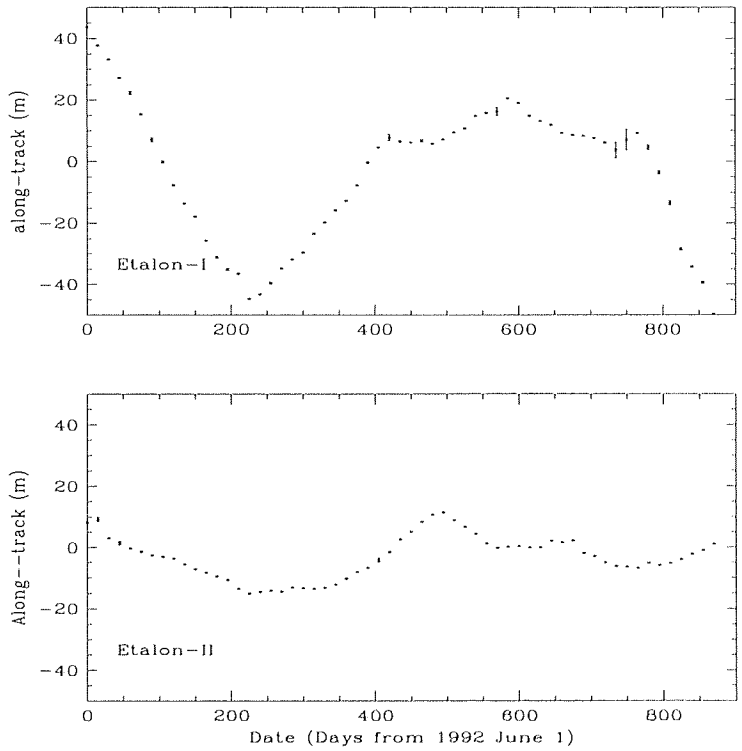


Figure 5.6: Along-track residuals at 25-day intervals.

Within each 25-day interval we found that the post–solution predicted residual rms reduced to an average 15 cm, with some intervals reaching 6cm rms. The resulting time series of corrections $\Delta\mathbf{e}$ were found to be dominated by the series of $\Delta(M+\omega)$, which represents along–track departures of the satellites relative to the long–arc orbits, which were not absorbed by the single empirical drag coefficient. The values of $\Delta(M+\omega)$ were initially expressed in angular measure (radians) and were converted to meters, to zero

order in the eccentricity, by multiplying by the orbital semi-major axes, $25.5 \times 10^6$. The $\Delta(M + \omega)$ series are shown in Figure 5.6, where the error bars are 1 $\sigma$ values determined during the least squares solutions.

### 5.5.3 Along–track errors

To investigate these series further, and to compare the values with the empirical long–arc mean drag accelerations of each satellite and with published results from the Lageos satellites, we note that the series represent the integrated effects of variable drag accelerations. Thus those accelerations may be deduced by computing the second time–derivatives of the values of $\Delta(M + \omega)$. To carry out the differentiation of the series, we use a method

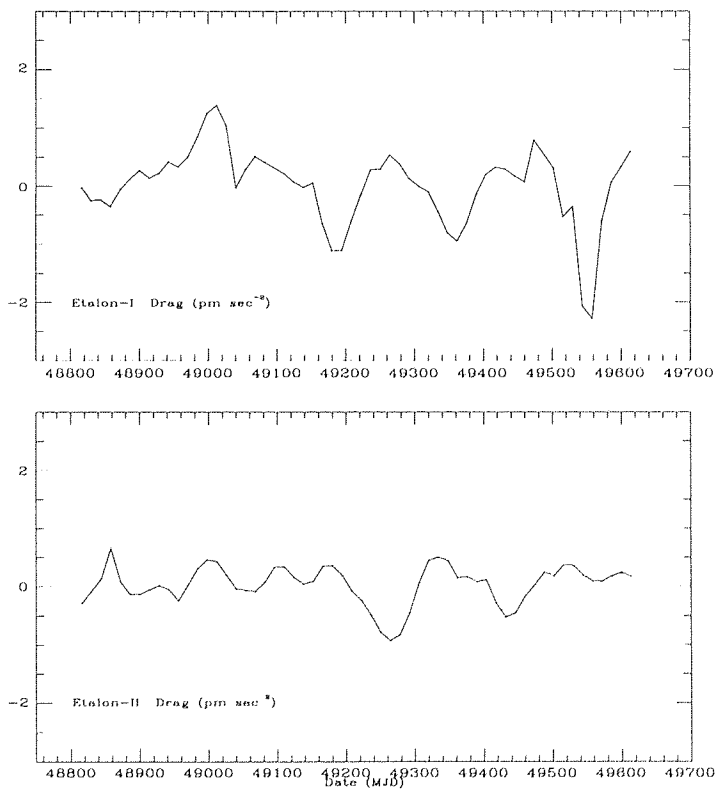


Figure 5.7: Along-track accelerations at 25-day intervals.

developed by Savitzky and Golay [55] for smoothing and differentiating data by simplified least squares. The method smooths subsets of the data by convolving with a weighting function which generates a smoothed point at the centre of the range of data. To generate

derivatives of the original data set, the weighting function has been differentiated before application. The procedure is presented by Savitzky and Golay as a series of coefficients to carry out smoothing or differentiation, and by experimentation we chose a 7–point quadratic weighting function to generate 2nd derivatives of the series. The procedure is applied to the first seven points of the series by multiplying by the equivalent seven weighting coefficients of the convolute and dividing by a given normalising value to compute a new central value which represents the best fit 2nd derivative at that point. We then step through the data by one point, and generate the next value in the new series. We lose 3 original data points from each end of the $\Delta(M+\omega)$ series. The resulting sets of accelerations are converted to pico-m $s^{-2}$, and are shown for each satellite in Figure 5.7. The plots show that the accelerations are of the order of $\pm$ 2 pico-m $s^{-2}$, and that strong periodicities exist. The mean values of each series are as expected insignificantly different from zero (-1.1$\times 10^{-2}$ and 3.8$\times 10^{-2}$ pico-m $s^{-2}$ respectively), since 900–day mean values were determined during the long–arc solutions.

A periodogramme analysis was carried out on the acceleration series, using a program which allows interactive selection and identification of significant peaks in the spectrum. The resulting spectra are shown in Figure 5.8, where the labels next to the selected peaks in the spectra give the identified periods in days. The strong, broad peaks in the spectra are at or near semi–annual frequencies. The presence of these periods in the acceleration series strongly suggest that the perturbing forces are solar related, non–gravitational thermal thrust forces similar to those acting on Lageos. A great deal of research has been carried out on these forces using the Lageos results. We will review some of that work, and carry out an investigation into the Etalon results, in Chapter 6.

Thus in summary, we find that the along–track accelerations of the satellites have long–term averages of some 0.1 pico-m $s^{-2}$, upon which are superimposed semi–annual terms with amplitudes of up to 2 pico-m $s^{-2}$. There exist interesting signatures in the residual series of other orbital elements, which we investigate in Chapter 7.

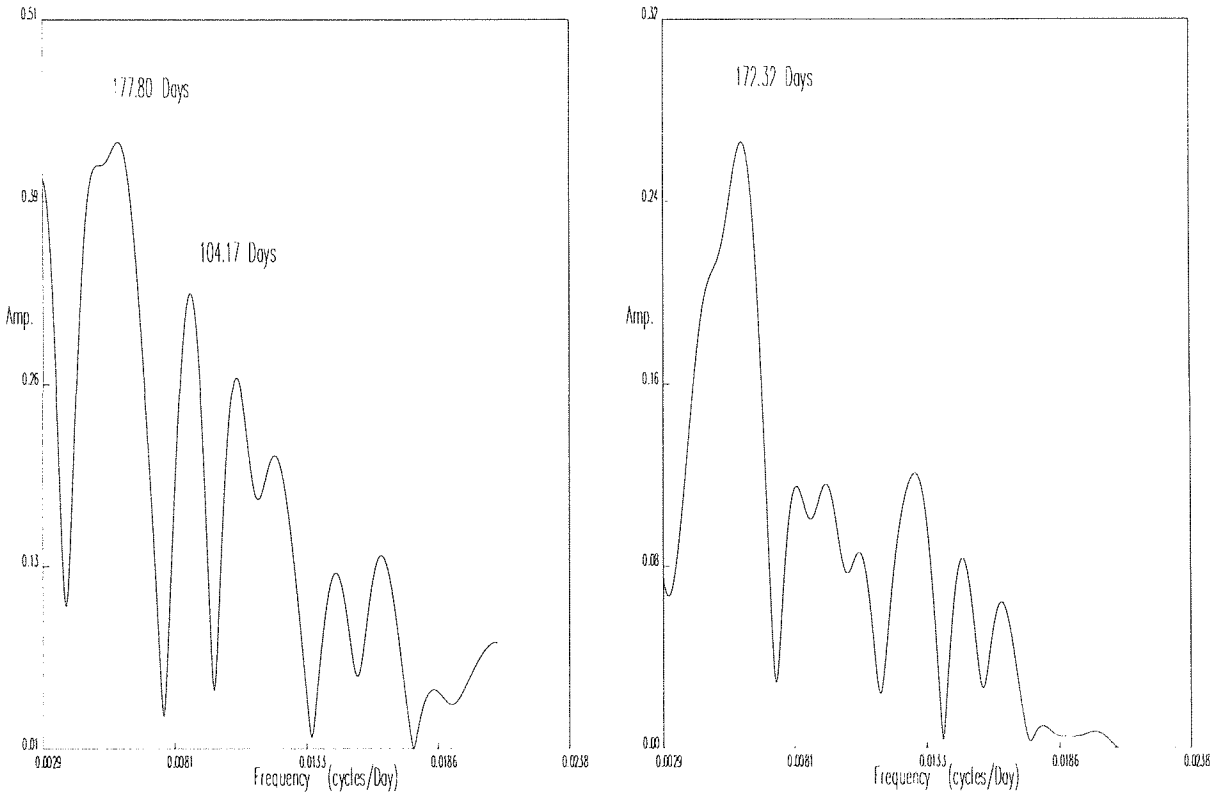


Figure 5.8: Spectra of Etalon-I and Etalon-II along–track accelerations.

# Chapter 6

# Modelling of Thermal Forces on the Etalon Satellites.

## 6.1 Introduction

In the previous Chapter we described our method of fitting single continuous orbital arcs of 2.5 years duration to SLR observations of the two Etalon satellites. We solved for a minimal parameter set comprising initial state vector, a single empirical along-track drag term and a single coefficient of solar radiation. We obtained post-solution residual rms values of 2.80 and 1.18 m for Etalon-1 and Etalon-2 respectively. From the range residuals we then solved for a series of equivalent corrections to mean orbital elements over 25-day intervals in order to investigate potential deficiencies in our force models. We found that the series of corrections to orbital elements was dominated by that of the argument of latitude $(M + \omega)$, and we double-differentiated this series to derive a set of along-track acceleration residuals. In this chapter we set out our analysis of both these un-modelled along-track accelerations and of the 2.5-year average along-track acceleration determined from the empirical drag term. We first review the current theories that have been developed to explain similar effects observed with the Lageos satellite, and then move on to modify and test these theories in our model of the behaviour of the Etalon satellites.

## 6.2 Thermal Force Theory

As an introduction to our study of the measured along-track accelerations experienced by the satellites and determined from the residuals from the long-arc orbits, we consider the results and theoretical models regarding similar phenomena for Lageos. The Etalon satellites are the only other satellites that are likely to be suitable to provide a test of the models established for Lageos. For lower satellites other drag effects dominate, and for higher satellites (e.g. GPS and Glonass) the forces on their large solar panels dominate. We wish to test whether the theories can explain both the small average along-track accelerations and the rapid fluctuations seen throughout the 2.5 year period.

Soon after launch in 1976, orbital fits to laser range observations of Lageos indicated that the satellite was experiencing an along-track acceleration of mean value about -3.3 pico-meters $s^{-2}$ (pm $s^{-2}$) [56], which is equivalent to an orbital decay of some 1.2 mm per day. Superimposed on this mean acceleration were found both smooth periodic fluctuations and spikes which could reach a similar magnitude. Several mechanisms have since been proposed to explain both the mean acceleration and the fluctuations and spikes, and we review the current models, considering at first the mean acceleration. Initially a combination of charged and neutral particle drag was thought to be responsible, with the neutral particles accounting for only about 10% of the effect [57, 58, 59]. A more recent analysis by Rubincam [60], indicates that neutral and charged particle drag on Lageos are of similar magnitude, but together account for only about 30% of the observed along-track acceleration. Rubincam [61, 62] proposed that the Yarkovsky effect [63, 64, 57], which is the asymmetric thermal response of Lageos to Earth-emitted infra-red radiation (IR), could account for about 70% of the observed mean along-track acceleration, by the following mechanism. For simplicity at first it is assumed that Lageos' spin axis lies in the plane of the orbit. IR radiation is absorbed, and since Lageos is spinning rapidly, with a rotation period of about 20s in 1988 according to the model of Bertotti and Iess [65], the heat distribution is uniform longitudinally, but not latitudinally. This creates a temperature imbalance between Lageos' northern and southern hemispheres, generating a thrust along the spin axis when the heat is re-radiated. The thrust is away from the hotter pole, and therefore the satellite is accelerated along the direction of the cooler axis. Now if the satellite had no thermal inertia, then a hemisphere would be hottest

when the Earth is directly over its pole. In this case the net along-track component of the force is zero because of cancellation when averaging over one orbit, since during the orbit alternate hemispheres face the Earth. However, since the satellite, and in particular the retro-reflectors, do possess thermal inertia, there is a delay in re-radiation relative to the time of maximum temperature, during which the satellite moves along its orbit. Subsequent re-radiation will then have a component opposite to the along-track direction, and act as a drag force. The situation is shown in Figure 6.1.

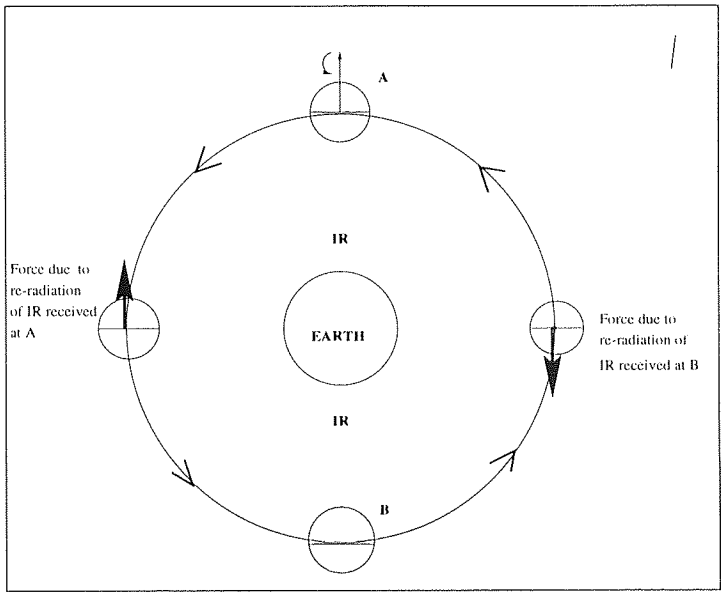


Figure 6.1: Yarkovsky drag on a satellite due to thermal heating from the Earth. The satellite spin axis is in the plane of the orbit, and the thermal lag angle is taken to be 90 degrees for illustration only.

To model this effect, Rubincam [62] develops a model for the thermal inertia of the satellite which includes the radiative heat transfer between the retro-reflectors, their mounting rings and the aluminium cavities in which the reflectors are housed. By using energy balance arguments and engineering data, Rubincam computes the temperatures of the retro-reflectors, of the mounting rings and of the aluminium shell, subject to solar and Earth-reflected heating. In the earlier work, Rubincam [61] showed that the effect of the retro-reflectors dominated the model for the satellite acceleration, so now Rubincam [62] uses his improved model of their temperatures and thermal inertia to compute the average thermal acceleration, or drag, on the satellite. He finds that an

acceleration of -2.33pm $s^{-2}$ can be explained by this mechanism.

Following and extending this development, Scharroo *et al* [66], deduce that the Yarkovsky effect can cause an acceleration of -3.08pm $s^{-2}$, again if the spin axis of Lageos lies in the orbital plane. The increase in the acceleration accounted for in the model of Scharroo *et al* is said to be due to their use of engineering data for the thermal model, rather than the theoretical energy balance work of Rubincam [62].

Now if the spin axis is tilted with respect to the orbital plane, the thermal drag decreases as the tilt increases, and finally vanishes when the axis is normal to the plane, provided that the satellite has a reasonably fast spin rate. In such an orientation, there is no temperature imbalance between the northern and southern hemispheres, as the Earth is over Lageos' equator. If the inclination of the spin axis to the orbital plane is denoted by $\beta$, (where $\beta = 0$ if the spin axis lies in the orbital plane), then the temperature gradient on the satellite decreases as $\beta$ increases, and in addition the along-track component of the acceleration will decrease with increasing angle $\beta$. Each effect introduces a dependence on $\cos\beta$, and so the actual along track acceleration $s$ will be related to the maximum possible value $s_{max}$ by

$$s = s_{max} \cos^2 \beta. \tag{6.1}$$

On the assumption that the spin axis is fixed in inertial space, precession of the orbital node along the Earth's equator will cause a periodic variation of the angle $\beta$, and thus a slow variation in the amplitude of the along-track acceleration. In this way the model predicts periodic variations about the mean with frequencies of once and twice per nodal revolution of the Lageos orbit, that is with periods of 1050 and 525 days, which are indeed seen in the observed accelerations. Scharroo *et al* [66] further speculate that the gradual decrease in the observed amplitudes of the periodic variations in the acceleration series may be caused by a slow alignment of the spin axis of Lageos with the Earth's axis, from its initial offset of 22 degrees which was set during the launch in 1976. Such an alignment is considered likely under the interaction between the Earth's magnetic field and charged-particle-induced eddy currents in the satellite.

Scharroo *et al* [66] propose that the angle between the spin axes of the satellite and of the Earth is decreasing exponentially, and find that their model of Yarkovsky thermal drag fits the observed mean acceleration and long-period variation well, but does not

explain the rapid spikes in the data. To address this behaviour, Scharroo *et al* combine two further thermal thrust effects, namely the Yarkovsky-Schach effect and anisotropic reflection of sunlight caused by an hypothesised hemispheric albedo difference.

The Yarkovsky-Schach effect is caused by direct solar heating, as opposed to heating from the Earth. If the satellite spin axis has only a small motion in inertial space during one orbital period, then again a hemispheric temperature gradient will be set up, and an acceleration along the cooler spin axis away from the hotter pole will result. The effect will be a maximum if one of the poles faces the Sun, and will vanish if the Sun is over the satellite equator. The acceleration along the spin axis will of course have components in the along-track, across-track and radial directions. If we consider the along-track effect, it is clear that during one orbital period there will be no net acceleration because the thrust will alternately be in the direction of satellite motion, and half an orbital revolution later, opposing the motion, as for the Yarkovsky effect. However, the effect will give rise to once-per-revolution accelerations.

Now if the satellite undergoes eclipse by the Earth (or Moon), the solar radiation will be cut off, and the thrust will vanish for the duration of the eclipse. In this situation, the along-track acceleration will not average to zero during one revolution, and a net acceleration will occur. Whether this acceleration acts with or against the direction of motion depends upon the Sun-orbit geometry and upon the direction of the satellite spin axis. Thermal inertia again is an important contributor to the effect, as the temperature gradient and hence the thrust does not instantaneously vanish at the onset of an eclipse, nor is it instantaneously restored at the end of an eclipse. Thus the magnitude of the effect depends upon the duration of a given eclipse; for a short eclipse the satellite may not have time to cool to an equilibrium temperature before moving back into sunlight, and the net acceleration will be small. For an eclipse long with respect to the thermal inertia, the equilibrium temperature may be maintained for some time before solar heating gradually restores the temperature gradient, and a large net acceleration will result. During an entire eclipse season of some weeks, both short eclipses at the onset and end of the season, and long-duration eclipses mid-season will occur.

This is the Yarkovsky-Schach (Y-S) effect which was successfully applied by Scharroo *et al* [66], to explain some of the spikes in the observations of Lageos' along-track acceler-

ation. They found that the Y-S effect did not explain all the acceleration spikes however, and they invoked a further effect, namely anisotropic reflection of sunlight caused by a possible hemispheric difference in reflectivity. They find that an albedo difference of only 5% between the two hemispheres would, when taken in addition to the Y-S effect, adequately explain the observed pattern of acceleration spikes. However, Smith *et al* [38], point out that the prediction capability of the models does appear to degrade after 1989. All authors point out the crucial importance to the models of a knowledge of the direction of the satellite spin axis.

We now apply the above thermal models to our along-track acceleration residuals from the long-arc solutions of the two Etalon Satellites.

## 6.3 Application to Etalon results

### 6.3.1 Average along-track acceleration

To evaluate fully the thermal drag on the Etalons due to Earth emitted IR radiation, we need detailed engineering data on the structure of the satellites, and a knowledge of the direction of their spin axes. The engineering data available is restricted to basic information on satellite size and mass, and size and number of retro-reflectors [3]. The spin axes directions are not known [67]. However, despite these problems, we can make reasonable estimates of the forces on the satellites by analogy to the results for Lageos, by substituting such information that is available for the Etalons. We shall assume initially that the spin axes of the satellites lie in their orbital planes, and hopefully modify this if required by the observations.

We know that every surface with a non-zero temperature $T$ radiates energy in the form of photons, and since these photons carry away momentum, the emitting surface will recoil. If the surface has an area $\Delta A$ and emissivity $\epsilon$, and emits radiation diffusely according to Lambert's cosine law, then the surface will be subject to a force

$$\Delta F = (2\epsilon\sigma T^4/3c)\Delta A \tag{6.2}$$

acting along the normal to the surface, where $\sigma$ is the Stefan-Boltzmann constant and $c$ is the speed of light. Scharroo *et al* [66] integrate this expression for $\Delta F$ over the surface of

the spherical satellite, noting that all components of the force perpendicular to the spin axis cancel. Then by dividing by the mass $M$ of the satellite, they obtain the following expression for $s$, the acceleration along the spin axis.

$$s = \frac{-4(\epsilon A)\sigma T_0^3}{9Mc}\Delta T_0 \cos\Theta_r \tag{6.3}$$

Here $T_0$ is the mean surface temperature and $\Delta T_0$ is the maximum temperature difference that could occur across the satellite if one pole faces directly towards the radiation source. $\Theta_r$ is the angle between the satellite spin axis and the direction to the source of radiation, in this case the surface of the Earth, and $(\epsilon A)$ is the effective emitting surface area of the satellite. Now both Rubincam [62] and Scharroo *et al* [66] argue that the aluminium surface of a satellite plays no significant role in the thermal effects, based on the following arguments. The high conductivity of the aluminium surface will rapidly tend to reduce any asymmetry in the temperature distribution across the satellite. By contrast the retro-reflectors, which in the case of Lageos at least, are insulated from the satellite surface and hence from each other will allow a temperature asymmetry to build up. In addition the emissivity of aluminium is only one third that of silica, which further reduces the effect of the satellite surface. Thus we can take $A$ in the above expression as just the total surface area of the reflectors. We take from Mironov *et al* [18] the information shown in Table 6.1

| Satellite | | Retro-reflectors | | | |
|---|---|---|---|---|---|
| Diameter (mm) | Mass (Kg) | Width (mm) | Depth (mm) | Number (silica) | Number (germanium) |
| 1294 | 1415 | 27.0 | 19.1 | 2140 | 6 |

Table 6.1: Etalon Characteristics.

From this data, we compute the front-face area $a_f$ of each hexagonal retro-reflector as $a_f = 631\text{mm}^2$. For the 2146 retro-reflectors, this leads to a total area $A$ of $1.355 \times 10^6\text{mm}^2$, compared to a total surface area of the satellite of $4\pi r^2 = 5.26 \times 10^6\text{mm}^2$, that is the retro-reflectors cover some 26% of the satellite surface. We take emissivity $\epsilon = 0.9$ for silica from Rubincam [62].

We must estimate $\Delta T_0$, given that for Lageos the quoted value is $8.^o1$K from NASA engineering data [66]. Now the radiance of IR from the sub-Earth point is given by [68]

$$F_{IR} = 232(a_e/a)^2 \ Wm^{-2},$$

with $a_e$ the radius of the Earth and $a$ the orbital semi-major axis. So for Lageos, with $a = 12400$ km, $F_{IR} = 66.5Wm^{-2}$ and for Etalon, with $a = 25500$ km, $F_{IR} = 14.5Wm^{-2}$. We now scale the temperature difference $\Delta T_0$ for Etalon relative to the value of $8.^o1$K for Lageos in proportion to the ratio of these radiance values, and estimate $\Delta T_0 = 1.^o9$K for Etalon.

Now due to thermal inertia in the retro-reflectors, we must replace $\Theta_r$ by $\Theta_r - \Phi$, where $\Phi$ is the phase lag, which is a function of the mean orbital motion $n$ of Etalon and the thermal response time $\tau$ of the retro-reflectors. From Scharroo *et al* [66] we have

$$\tau = \frac{mC_p}{4\epsilon a_f \sigma T_0^3},$$

where $m$ is the mass of a retro-reflector, and $C_p$ is the specific heat of silica. $T_0$ is the mean temperature of a retro-reflector, which we take from the estimate of Lucchesi [45] who has $T_0 = 316^oK$. Again we do not have a value for the retro-reflector mass $m$, so must estimate it from the available data. From scale drawings shown in Mironov *et al* [18], we estimate the volume of the retro-reflector to be $7.21 \times 10^{-6}$ m$^3$, and given the density of silica, 2200 kg m$^{-3}$ [61] we have that $m = 1.6 \times 10^{-2}$ kg. The equivalent value for a Lageos retro-reflector is $3.9 \times 10^{-2}$ kg, [62]. Then finally we have

$$\tau = 2567 \text{ s}$$

We convert this response time to orbital phase lag $\Phi$ by multiplication by the satellites' mean motion, $n = 2.13$ revs day$^{-1}$. This gives

$$\Phi = 0.40 \text{ radians} = 22.^o7$$

Then for the case when the spin axis lies in the orbital plane, Scharroo *et al* [66] finally give the maximum along-track acceleration by averaging over one revolution, when of course $\Theta_r$ averages to zero. They obtain

$$s_{max} = \frac{-\epsilon A \sigma T_0^3}{9Mc} \Delta T \sin 2\Phi \tag{6.4}$$

The dependence of $s_{max}$ on $\sin 2\Phi$ shows the absolute dependence of this effect on the thermal inertia of the satellite; if there were no inertia, the effect would disappear. Then substituting the values that we have for the Etalon satellites, we obtain $s_{max} = -0.46$ pm s$^{-2}$

This value is some six times smaller than the equivalent value for Lageos of $-3.08$pms$^{-2}$, both by virtue of the reduced IR flux at the altitude of Etalon, and due to the smaller phase lag $\Phi$.

Now, as we have seen, if the spin axis does not lie in the orbital plane the thermal lag will vary as $\cos^2\beta$, where $\beta$ is the inclination of the spin axis to this plane. For instance, if the satellite's axis is aligned with the Earth's axis, then $\beta = 90 - i$, where $i$ is the inclination of the orbital plane to the Earth's equator, and $i = 65^o$. So in this orientation we expect $s = s_{max}\cos^2 25 = -0.38$pm s$^{-2}$.

In addition, even if the spin axis does remain fixed in space, the angle $\beta$ will vary due to the precession of the orbital plane under the influence of, principally, $J_2$. From Kaula [52], we have

$$\dot{\Omega} = \frac{-3nJ_2a_e^2}{2(1-e^2)^2a^2}\cos i,$$

which for Etalon with $e \sim 0$, leads to a value of $\dot{\Omega} = -3.^o2 \times 10^{-2}$day$^{-1}$, and a precession period of $> 30$ years. Thus we cannot expect to observe any periodic effects due to thermal Yarkovsky thrust during the relatively short 2.5 year interval of our investigation. This is in contrast to the results for Lageos [66] where the relatively short precession period of 2.9 years leads to variations of $s$ with the same period. These periodic variations in the Lageos results are both seen in the data and accurately predicted by the model.

Thus, in conclusion, Yarkovsky thermal drag on the Etalon satellites predicts a secular along-track acceleration of between -0.46 and -0.38 pm s$^{-2}$, depending on whether the spin axis lies in the orbital plane or is aligned with the Earth's axis, and we expect no significant periodic variations over the 2.5 year span of our analysis.

### Comparison with Observations.

From our analyses summarised in Table 5.2, we have observed *drag* values of +0.138 and +0.102 pm s$^{-2}$ for the two satellites, which are equivalent to along-track accelerations of minus those quantities. Thus the modelled acceleration of -0.46 pm s$^{-2}$ is an over-

estimate of that observed, and suggests that on average over the 2.5 year span the spin axes are not aligned with the orbital plane nor with the Earth's axis, but are rotated further out of the orbital plane. Of course, if the axes were perpendicular to the plane, the Yarkovsky effect would disappear. The observed accelerations imply that on average over the 2.5 years the spin axis of Etalon 1 was inclined at 56 degrees to the orbital plane, and that of Etalon 2 at 62 degrees.

### 6.3.2 Acceleration Spikes

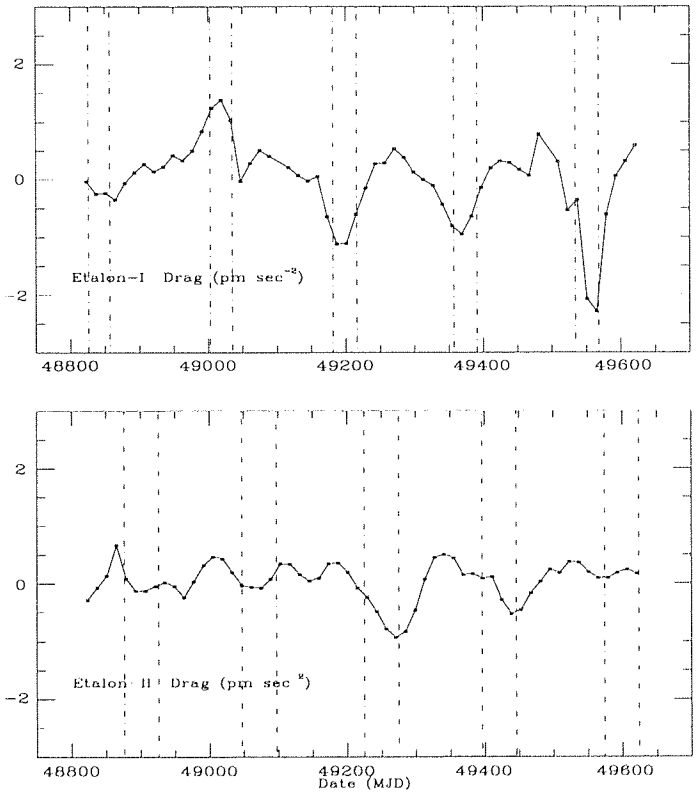


Figure 6.2: Along-track accelerations and eclipse seasons

The Yarkovsky effect considered above, as we have seen, cannot account for the 'spikes' in the acceleration residuals, which are seen in the plots in Figure 6.2. The figure shows the same results as those plotted in Figure 5.7 in Chapter 5, but we now also show within the pairs of vertical dotted lines the time zones during which the satellites enter the Earth's shadow during each orbit.

Several features are apparent when we compare the results for the two satellites. The Etalon-1 results in the upper plot show acceleration spikes with considerably higher

amplitude than the Etalon-2 spikes, which immediately explains the poorer fit of the Etalon-1 long-arc solution to the observations (see Table 5.2). We also see that most of the spikes, particularly for Etalon-1, occur during the eclipse seasons, and reach their maximum amplitude at mid-season. Not all eclipse seasons do produce spikes, however, and there are some spikes that are not associated with eclipses. However, the frequent occurrence of the spikes during the eclipse seasons is similar to that found for the Lageos results [66] and suggests that the Yarkovsky-Schach (Y-S) mechanism may be a contributing factor, which requires further investigation. As an initial step, we introduce the Y-S effect into our force model by reference to equation (6.3), where now $\Theta_r$ is the angle between the satellite spin axis and the direction of the Sun as seen from the satellite. That is the acceleration along the spin axis is

$$s = s_{max} \cos \Theta_r, \tag{6.5}$$

where from (6.3)

$$s_{max} = \frac{-4\epsilon A \sigma T_0^3}{9Mc} \Delta T_0 \tag{6.6}$$

where now $\Delta T_0$ is the temperature difference between a retro-reflector directly facing the Sun and one facing in the opposite direction. Thus now $s_{max}$ represents the maximum acceleration along the spin axis if that axis points directly towards the Sun. Scharroo *et al* [66] have used the time series of Lageos along-track accelerations to estimate $s_{max}$, and find $s_{max} = -89 pms^{-2}$. Lucchesi [45] has estimated the acceleration for the Etalons by a theoretical determination of $\Delta T_0$, and finds $s_{max} = -65$pm s$^{-2}$. We initially take Lucchesi's value for $s_{max}$. Without prejudicing our aim to use the observations of the acceleration spikes to deduce the behaviour of the directions of the satellites' spin axes, we find at this stage that it is helpful for the explanation and development if we assume that the spin axes **sp** are inclined to the orbital planes by angles $\beta$ such that the axes are aligned with the Earth's axis. Approximately then, $\beta = 90 - \iota \approx 25^o$.

Then at each integration step we compute $s$ from (6.5), where $\cos \Theta_r = \hat{\mathbf{x}}_a . \widehat{sp}$, where $\mathbf{x}_a$ is the vector from the satellite to the Sun.

We note here that if the spin axis *is* aligned with that of the Earth, then angle $\Theta_r$ is given by $\Theta_r = 90 - \delta_s$, where $\delta_s$ is the geocentric declination of the Sun. We also find that the eclipse seasons for Etalon-1 take place near the summer and winter solstices,

when the absolute values of the Sun's declination are high ($\sim 20$ deg), whereas the eclipse seasons for Etalon-2 occur near the equinoxes, with the Sun's declination reaching only a few degrees. These circumstances would explain the larger amplitudes of the spikes in the Etalon-1 acceleration series, since the temperature anomaly on the satellite and hence the magnitude of the Y-S acceleration depends directly upon $\cos\Theta_r$. That the eclipse seasons remain close to these relationships with the Terrestrial seasons during the period of the analysis is again attributable to the very small nodal precession rates of the Etalon orbital planes.

Now in the absence of eclipses, $s$ will average to zero during one revolution of the satellite. Figure 6.3 shows this effect for the Y-S accelerations on Etalon-1 during one day, where we have resolved the acceleration, computed in the direction of the spin axis, into along-track and radial components. For an acceleration $\mathbf{s}$ along the spin axis, the component in the along-track direction is just $\frac{\mathbf{s}.\mathbf{v}}{v}$, and in the radial direction $\frac{\mathbf{s}.\mathbf{x}}{x}$, where $\mathbf{x}$ and $\mathbf{v}$ are the geocentric position and velocity vectors of the satellite.

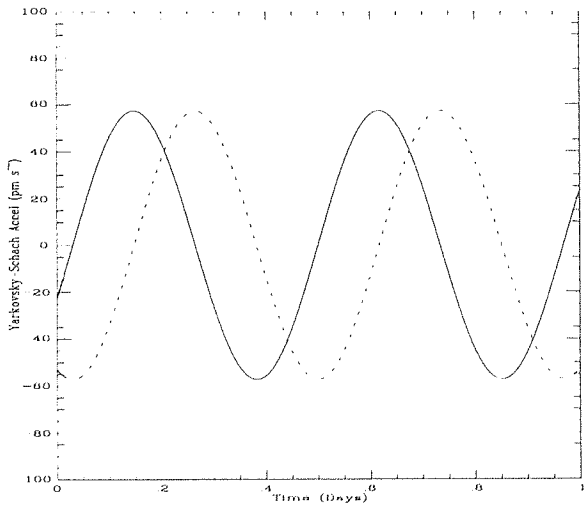


Figure 6.3: Daily Yarkovsky-Schach acceleration in absence of eclipses. Full line is along-track component; dotted line is radial component

The accelerations are seen to be quite large, with semi-amplitude more than 50 pm $s^{-2}$. It is usual in precise orbit determination to solve for empirical once-per-revolution acceleration terms to absorb miscellaneous imperfections in the force model. The thermal force discussed here is seen to be an important contributor to these effects.

During the eclipse seasons we must model the cooling down of the satellite which

begins upon passage through the penumbral region of the shadow, which occurs in a few tens of seconds (see Chapter 4), and the heating up and consequent restoration of the thermal thrust upon emergence from the shadow. We have already computed in Section 6.2.2 the thermal lag angle $\Phi$, and we use it again in this instance. We follow Scharroo *et al* [66], and compute a function $f(u)$ where $u$ is the argument of latitude of the satellite $(M+\omega,)$ and where $f(u) = 1.0$ outside the eclipse zone, and $f(u)$ tends exponentially to zero after the satellite enters the shadow, and tends to 1 again after the satellite emerges into full sunlight. Scharroo *et al* [66] give

$$f(u) = \exp\left(-\frac{u-u_1}{\Phi}\right), \tag{6.7}$$

for $u_1 \leq u \leq u_2$, and

$$f(u) = 1 + \left[1 - \exp\left(\frac{u_2-u_1}{\Phi}\right)\right] \exp\left(-\frac{u-u_1}{\Phi}\right), \tag{6.8}$$

for $u_2 \leq u \leq u_1 + 2\pi$. Here $u_1$ and $u_2$ are the values of $(M+\omega)$ at shadow entry and exit respectively. We included this function in our computation of $s$, from (6.5), which now becomes

$$s = s_{max} f(u) \cos\Theta_r, \tag{6.9}$$

and again generated the resulting along-track and radial accelerations on Etalon-1, for a day during the first eclipse season shown in Figure 6.2.

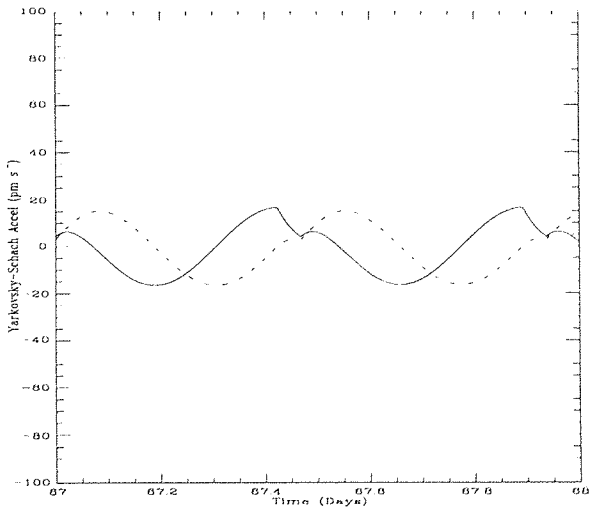


Figure 6.4: Yarkovsky-Schach acceleration during one day of eclipse season. Full line is along-track component; dotted line is radial component.

The plots are shown in Figure 6.4, where now the acceleration is not symmetrical and can be seen not to average to zero during one orbit.

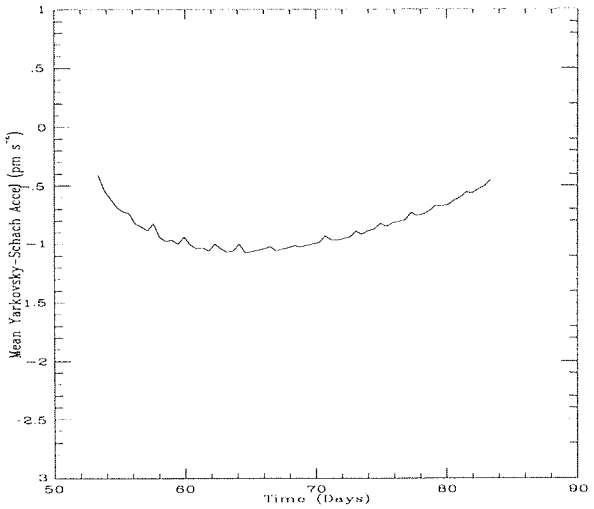


Figure 6.5: Mean Yarkovsky-Schach acceleration during first eclipse season of Etalon-1.

We have numerically averaged over intervals of $0 \leq u \leq 2\pi$ the computed along-track accelerations for the whole 35 days of the first eclipse season and plot the results in Figure 6.5. We find a negative acceleration spike that reaches its minimum value of some -1.1 pm $s^{-1}$ a little before mid-eclipse season. This behaviour is as expected from the general explanation of the Y-S effect given in Section 6.2.1, but the lack of symmetry in the spike is due to the change in declination of the Sun during the eclipse season, with the resulting change in angle $\Theta_r$.

We now carry out this averaging process for the whole span of the analysis, for both satellites. The results are plotted as the full lines along with the observed acceleration series in Figure 6.6.

It is useful to check that the computed spikes have intuitively the correct characteristics, given the circumstances during a particular eclipse season, as we wish to use the agreement or otherwise of the modelled accelerations with the observations to infer modifications to our assumptions about the direction of the satellites' spin axes. For the first two eclipse seasons of the analysis of the Etalon-1 observations, which are centred upon MJD 48825 (1992 July 22) and MJD 49015 (1993 January 28), we have looked in some detail at the circumstances. During the first season the satellite enters eclipse near the descending node of its orbit on the Earth's equator. With our assumption of

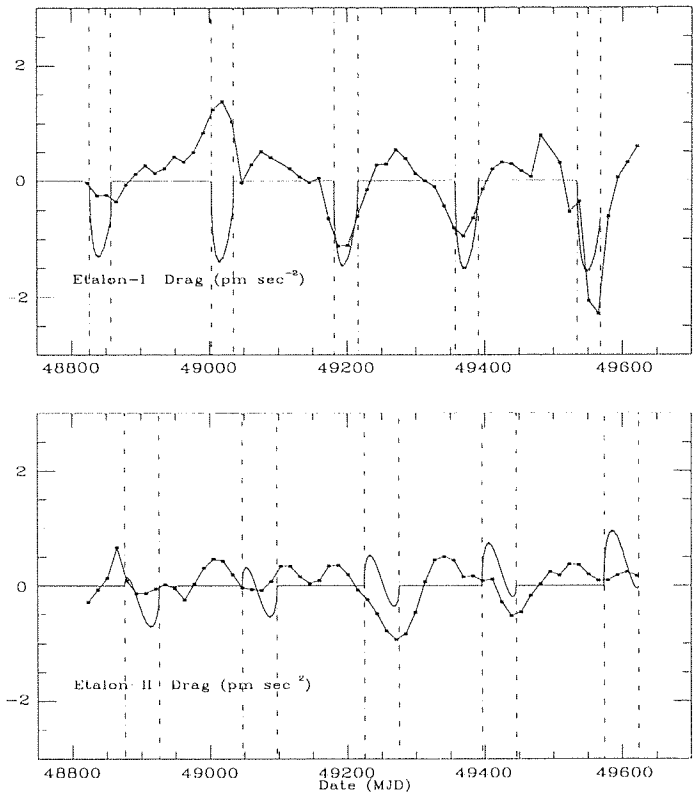


Figure 6.6: Along-track accelerations and Y-S model

a spin axis aligned with the Earth's, we find that the Sun is some 20 degrees north of Etalon's equator, thus the northern hemisphere is hotter than the south, and there is an acceleration in the direction of the southern pole of the satellite, and thus a component of that acceleration in the direction of motion of the satellite.

The situation is shown schematically in Figure 6.7, where the left-hand drawing refers to the July 22 eclipse season, at a moment prior to the satellite entering the eclipse zone, represented by the vertical lines. The Sun is north of the satellite equator, and as a result the thermal thrust acceleration is in the direction of the southern pole, shown by the arrow. Upon entry to the shadow, the thermal thrust tends to zero, and the positive along-track acceleration disappears, so during one orbital period in which an eclipse occurs, there is a net negative along-track acceleration.

The right-hand drawing in Figure 6.7 shows the situation six months later, during the second eclipse season. The satellite is near the ascending node of the orbit, and the Sun is south of the satellite's equator. There is then a thrust towards the northern hemisphere, and again a component in the along-track direction. As before, upon entry into shadow, the acceleration effectively becomes a negative along-track acceleration.

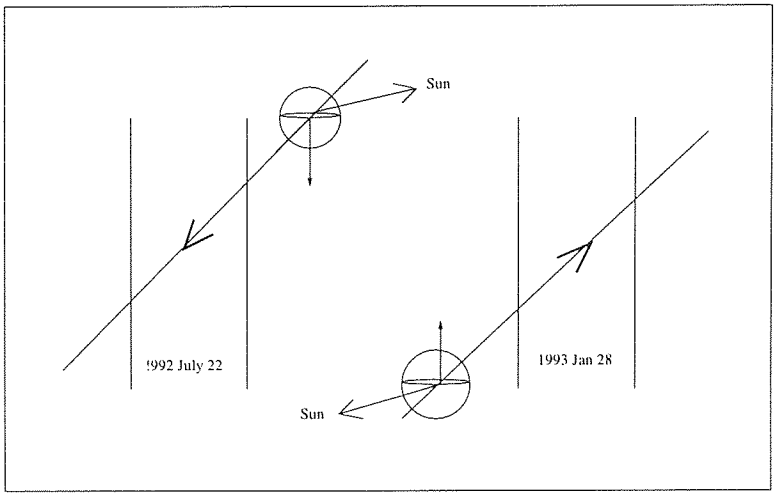


Figure 6.7: Schematic of Yarkovski-Schach effect on Etalon-1 during two eclipse seasons.

Again due to the long nodal precession period, this situation is repeated almost unchanged for the whole of our analysis period, and the series of negative spikes results. The lack of symmetry in the computed spikes for the Etalon-2 eclipse seasons can be traced to the fact that the direction of the Sun relative to the satellite's equator changes by several degrees during each season for these near-equinox eclipses, and thus both the magnitude and direction of the thermal thrust will change significantly during the period.

We now return to the comparison of model with observations, shown in Figure 6.6. We see that for Etalon-1 the computed acceleration spikes do not agree at all with the results during the first two eclipse seasons, but there is reasonable agreement for the remaining three seasons, with the model underestimating the amplitude of the final spike of the series.

For Etalon-2 the modelled spikes have smaller amplitudes, in agreement with the observations, but the overall agreement is equally poor throughout the period. At this point we can quickly discount an additional thrust effect due to an hypothesised asymmetric albedo between the satellite hemispheres as used by Scharroo *et al* [66] to compliment the Y-S effect, and explain most of the Lageos acceleration spikes. If the spin axis remained fixed in space, then an asymmetric albedo would generate a series of alternating negative and positive spikes during the eclipse seasons. A combination of such a series with the Y-S effect thus cannot explain the observations shown in Figure 6.6, and we are led to hypothesize that the spin axis direction may have changed during the period of

the investigation.

To test this hypothesis we carried out the numerical averaging process as described above, but varied in a systematic search pattern the components of the unit spin vector, and visually compared the resulting spikes with those of the observations. We begin with the Etalon-1 results, and note that for the first eclipse season, the lack of a significant acceleration spike suggests that at that time the direction of the spin axis was close to perpendicular to the plane of the orbit, in which configuration an acceleration in the direction of the spin axis would not have an along-track component. For an instant near the middle of the first eclipse season, we compute a unit vector $\mathbf{p}$ perpendicular to the plane of the orbit from

$$\mathbf{p} = \frac{\mathbf{x} \times \mathbf{v}}{xv},$$

and find that $\mathbf{p} = (0.64, 0.64, 0.42)$.

For the second eclipse season, the search found that the unit vector (0.94, 0.00, 0.34) for the spin axis generated an acceleration spike in reasonable agreement with the observations. For the next two eclipse seasons, we found little improvement to the initial hypothesis that the spin axis was aligned with that of the Earth, namely that the unit spin axis vector is (0.00, 0.00, 1.00). However, for the final eclipse season, we find that we can better approximate the larger acceleration spike by allowing the spin axis to move some 20 degrees away from alignment with the Earth's axis.

The results of computing the Y-S acceleration for Etalon-1 using these spin vectors at the appropriate times is shown in Figure 6.8.

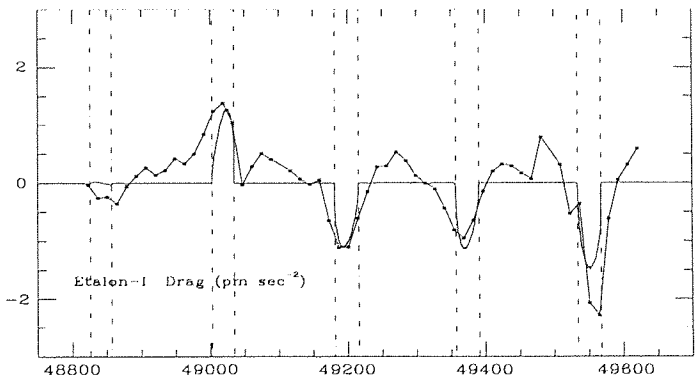


Figure 6.8: Etalon-1 Y-S model with variable spin axis direction.

We see that the model now fits the observations reasonably well, except that it underestimates the magnitudes of the second and last acceleration spikes. Hence these results

suggest that the spin axis direction may have changed dramatically during the analysis period, and that a major change appears to have come about between the first and second eclipse seasons, with a subsequent settling down into alignment with the Earth's axis.

| MJD | $s_x$ | $s_y$ | $s_z$ | $\delta$ | $\alpha$ |
|---|---|---|---|---|---|
| 48841 | 0.64 | 0.64 | 0.42 | 25 | 45 |
| 49019 | 0.94 | 0.00 | 0.34 | 20 | 0 |
| 49198 | 0.00 | 0.00 | 1.00 | 90 | 0 |
| 49374 | 0.00 | 0.00 | 1.00 | 90 | 0 |
| 49551 | -0.34 | 0.00 | 0.94 | 70 | 0 |

Table 6.2: Spin axis evolution for Etalon-1.

The results for the evolution of the axis are shown in Table 6.2, where we give the direction of the spin axis both in vector form with components $s_x, s_y, s_z$, and in terms of a geocentric celestial coordinate system given by solution for $\delta$ and $\alpha$ of the following transformation, where $\delta$ and $\alpha$ are the declination and right ascension of the spin axis.

$$\begin{aligned} s_x &= \cos\delta\cos\alpha \\ s_y &= \cos\delta\sin\alpha \\ s_z &= \sin\delta \end{aligned}$$

The dates (MJD) are those at the mid-time of each eclipse season for which the spin axis values apply. The values of $\delta$ and $\alpha$ in Table 6.2 show that the spin axis direction has undergone a large change during the analysis period.

We carry out the same procedures for the Etalon-2 data, where the absence of any clear peaks during the first, second and last eclipse seasons implies that the spin axis is perpendicular to the plane of the orbit at those times. For the other two eclipse seasons, we find little improvement in our initial hypothesis that the spin axis is parallel to the Earth's axis. The results of computing the Y-S acceleration with this series of spin axis vectors is shown in Figure 6.9

This series of accelerations is much less well fitted by the model than the Etalon-1 results, despite the smaller magnitude of the effect in the Etalon-2 data. Again it appears

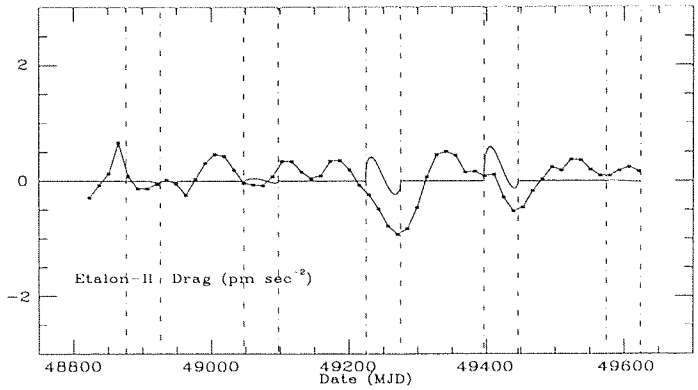


Figure 6.9: Etalon-2 Y-S model with variable spin axis direction.

likely that the spin axis is moving fairly rapidly. The results for the Etalon-2 spin axis solution are shown in Table 6.3

| MJD | $s_x$ | $s_y$ | $s_z$ | $\delta$ | $\alpha$ |
|---|---|---|---|---|---|
| 48901 | 0.22 | -0.88 | 0.42 | 65 | 284 |
| 49072 | 0.22 | -0.88 | 0.42 | 65 | 284 |
| 49250 | 0.00 | 0.00 | 1.00 | 0 | 360 |
| 49421 | 0.00 | 0.00 | 1.00 | 0 | 360 |
| 49599 | -0.21 | -0.89 | 0.41 | 66 | 77 |

Table 6.3: Spin axis evolution for Etalon-2.

### 6.3.3 Discussion

The results using the Y-S theory suggest that the spin axes appear to be undergoing change, which is most dramatic during the first year of the Etalon-1 analysis period. In the six months between the second and third eclipse seasons, the angle between the Earth's axis and that of Etalon-1 appears to have changed by 70 degrees. The spin axis of Etalon-2 appears to move such that at times it is in alignment with the Earth's axis, and at other times apparently perpendicular to the plane of its orbit. Of course through this analysis we are in a position to estimate the directions of the spin axes only during the respective eclipse periods of the two satellites, and can only speculate on possible causes for this apparent behaviour. For the apparently large change in Etalon-1, we might

conjecture that impact by a small body such as a micro-meteorite may have occurred. This may be followed by a damping of the chaotic motion and alignment with the Earth's axis by interaction between the Earth's magnetic field and the induction-charged body of the satellite, as proposed for Lageos by Bertotti and Iess [65]. The Etalon satellites also appear not to be axially symmetric, due to the presence of two small exterior probes used to attach two Glonass spacecraft during the initial phase of the launch of each of the satellites. (The probes are clearly seen near the lower edge of one of the satellites shown in the picture in Figure 1.2 in Chapter 1.) This mass asymmetry may lead to instability and chaotic motion especially as the spin rate decreases due to eddy-current braking, again as proposed for Lageos by Bertotti and Iess [65]. This model is less certain for Lageos however, as there is little evidence for mass asymmetry.

Clearly further work should be done to better understand and model the evolution of the spin axes of these satellites, which would help model the thermal thrust effects and thus test whether or not all the along track acceleration residuals are due to the Y-S effect.

### 6.3.4 Removal of along-track acceleration residuals

We finally carry out a solution in which we model the evolution of the spin axes by adopting in the force model the values of the spin axis vector as shown in Tables 6.2 and 6.3. We compute the Y-S acceleration in the direction of the spin axis using (6.9) and an initial estimate of $s_{max}$ of 65 pm $s^{-2}$. In the solution we solve for initial state vector, an empirical along-track acceleration, a coefficient of solar radiation and a correction to our initial $s_{max}$. However, at this point we encountered a problem which we believe is due to the apparently rapid change in spin axes directions. It was found to be impossible to remove the acceleration spikes from the along-track residuals. The solutions implied only small corrections to the initial value of $s_{max}$, but did not remove the thermal thrust effects.

In order to remove much more of the thermal thrust acceleration signatures, we must therefore include in our model a series of empirical along-track acceleration terms. Thus we carried out a solution for the along-track accelerations at 30-day intervals throughout the 2.5 year periods, and solved simultaneously for initial state vector and the solar

radiation coefficient, where the overall mean empirical along-track acceleration is accommodated in the coefficients of our piecewise-continuous series. In this way we remove most of the effects of the thermal thrust accelerations that our incomplete model could not account for. However, we discovered that a better removal of the systematic effects could be achieved by solving for a series of scale corrections to the model of Earth albedo accelerations, again at 30-day intervals.

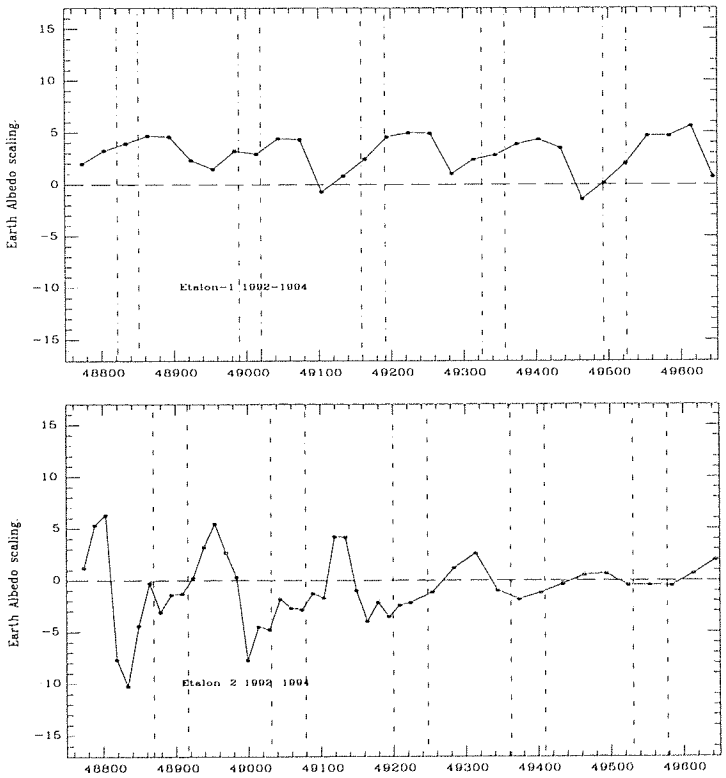


Figure 6.10: Earth Albedo Scaling Factors at 30-day Intervals.

Such a scaling factor will inevitably not only absorb real deficiencies in the albedo model, such as the neglect of specular reflections of sunlight from ocean surfaces, an effect considered important in Lageos analyses [69], but also remove the radial component of the thermal thrust effects that we have been considering. In this way our incomplete knowledge of the spin axes directions is circumvented. The post-solution residual rms values are 15 cm for Etalon-1 and 44 cm for Etalon-2 compared with values of 2.80 and

1.18 m respectively if the thermal effect is not solved for. The series of albedo scaling factors for each of the satellites is shown in Figure 6.10.

We find that the albedo scaling factors derived from the Etalon-1 solution are on average about 2.5, with a clear reduction to near unity midway between the eclipse seasons. This behaviour suggests that our albedo model underestimates the force for small Sun-Earth-satellite phase angles, when during the eclipse seasons the satellite passes in front of the Earth in full phase, some six hours after entering eclipse. A similar explanation has been proposed for anomalous behaviour of GPS satellites during the eclipse seasons. Fliegal and Gallini [70] point out that the Earth back-scatters strongly, and show that as a result at the height of the GPS (and Etalon) satellites the ratio of the acceleration due to Earth radiation pressure to that of direct solar radiation is some ten times that at phase angles of 90 degrees. We checked our albedo model to see whether it broadly agreed with this result of Fliegal and Gallini [70]. We output the magnitude of the albedo acceleration at the time that the satellite crossed the equator for each orbit, over a period of some 100 days near the end of which the satellite was undergoing shadow passages at the ascending node, and experiencing the acceleration from a full-phase Earth at the descending node. During the period of this experiment the phase angle ran from 90 degrees at the start to zero at mid-eclipse season, and the albedo acceleration ranged from about 10 to 100 pm $s^{-1}$. The acceleration due to solar radiation pressure is about 5312 pm $s^{-1}$, so we have that from our model the ratio of the albedo acceleration to that of the Sun is 2% at small phase angles, and 0.2% near 90 degrees. This agrees with Fliegal and Gallini [70] and shows that our albedo model [44] does represent the expected effect, but our observations suggest that the true effect at the height of the Etalons (and GPS) satellites is some 2.5 times greater still.

The results for Etalon-2 are far less regular. Again the scaling factors reach more 'normal' values during the times midway between the eclipse periods, but particularly during the first 18 months of the analysis very large scale factors ranging from -10 to +7 are seen. It appears probable that this behaviour is due to absorption of radial components of the unmodelled Y-S effect, with any true albedo variations being masked. The rapid variation in these results is an indication of the difficulty in modelling these effects for Etalon-2 relative to Etalon-1, and reflects the much poorer final fit to the

observations.

We now use the post solution range residuals to solve again for corrections to instantaneous orbital elements, to check the removal of the along-track acceleration spikes. Shown in Figure 6.11 is the residual along-track acceleration series, formed as described in Chapter 5 by double differentiation of the residual $(M + \omega)$ values, over intervals of 25 days. As we see, nearly all the systematic effects have been removed from the series, and we have a near flat track of residual accelerations.

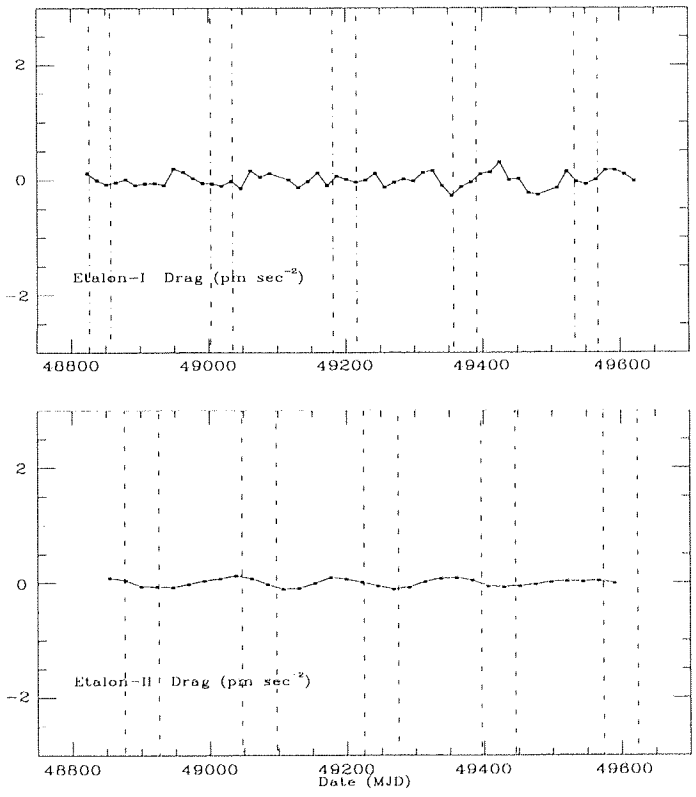


Figure 6.11: Post-solution Along-track Acceleration Residuals.

However the much poorer fit of the Etalon-2 orbit prompts further study, and we consider the residual series in eccentricity for each satellite, since eccentricity residuals can arise from not only gravity field effects but also from mis -modelling of thermal thrust effects.

### Eccentricity Residuals

Figure 6.12 shows the eccentricity residuals for the two satellites, plotted with 1-sigma error bars. The plots for each satellite are clearly different; the Etalon-1 results show a smooth periodic variation with amplitude $\Delta e$ of about $\pm 1.0 \times 10^{-8}$, which corresponds to a maximum radial orbital error of $\Delta r = \pm a \Delta e = \pm 25$ cm. However the results from in particular the first 350 days of Etalon-2 show a large oscillation of $\Delta e = +3$ to -5 $\times 10^{-8}$, equivalent to radial errors of up to 1.3 m, after which the residuals return to levels similar to those of Etalon-1. This behaviour explains the poorer fit of the orbit of Etalon-2 with a post-solution range residual rms of 44 cm compared to Etalon-1 (15 cm).

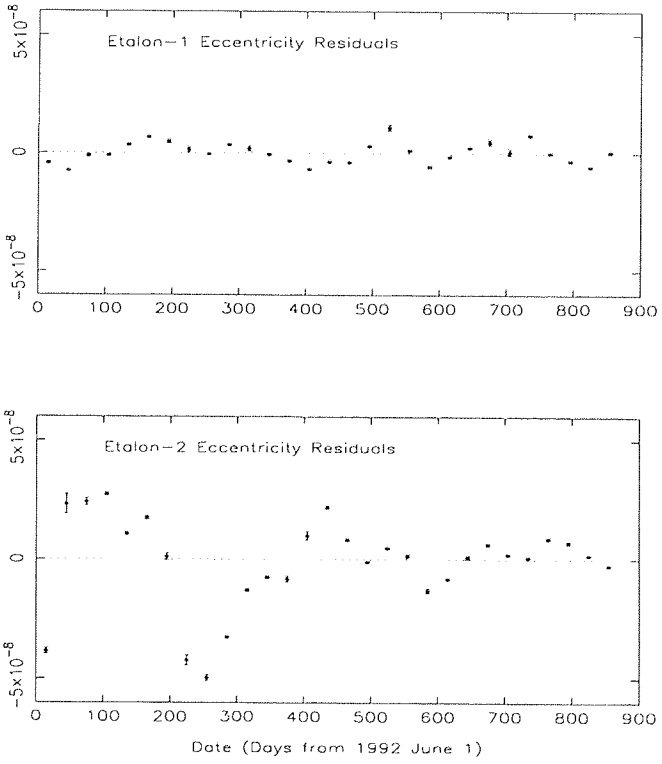


Figure 6.12: Post-solution Eccentricity Residuals.

Besides un-modelled thermal effects, eccentricity residuals are the result of errors in the odd zonal harmonics of the gravity field, both constant errors and variability due to un-modelled ocean tides and meteorological effects. Such gravity field errors should

give rise to the same signatures in the eccentricity residuals of both satellites, so we must conclude that the large excursion in the residuals for the first year of the Etalon-2 results is most likely due to thermal effects on that particular satellite not removed by our empirical acceleration model. Periods of a year or more of anomalous behaviour in the eccentricity residuals from long-arc analyses of Lageos data are well-documented. During 1989 the amplitude of the eccentricity residuals rose to some three times that of the previous 12 years [71] and caused Gegout and Cazenave [72] to exclude that year from their solutions for variability of $J_3$. A further large eccentricity anomaly is also apparent in the Lageos results beginning in mid-1991 [32, 71], which is considered much too large to be explained by odd-degree ocean tide or atmospheric tidal errors. Nerem [73] suggests that this anomalous behaviour may be related to the peak in the 11-year solar activity cycle. However, our current results tend to suggest that the behaviour is satellite-specific, and may cast doubt upon such conclusions.

### Eccentricity vector excitations

We can obtain more information on the characteristics of the residual eccentricity series and particularly on the anomalous results during the first year of Etalon-2 by following the approach of Tapley *et al* [71] and Martin and Rubincam [74] by computing eccentricity vector excitations. This approach also allows us to compare more readily our results with those of Lageos. The method involves examining the functions $e\sin\omega$ and $e\cos\omega$ since for nearly circular orbits this change of variables is better-determined, and defining the eccentricity vector excitation as

$$\Psi_p = \frac{d}{dt}\left[e\cos\omega - ie\sin\omega\right],$$

where $i$ is $\sqrt{-1}$. Then

$$\Psi_p = \left[\cos\omega\frac{de}{dt} - e\sin\omega\frac{d\omega}{dt}\right] - i\left[\sin\omega\frac{de}{dt} + e\cos\omega\frac{d\omega}{dt}\right] \tag{6.10}$$

Instantaneous values of the time derivatives $\frac{de}{dt}$ and $\frac{d\omega}{dt}$ are computed from the residual series of $e$ shown in Figure 6.12 and from that of $\omega$, by numerical differentiation using the method outlined in Chapter 5. Values of $e$ and $\omega$ are arithmetic mean values during each 25-day interval, calculated from the rectangular coordinates and velocities of the satellites. Then for each time interval, we calculate the real and imaginary part of the

eccentricity vector excitations for each satellite from (6.10), and plot the results in Figures 6.13 and 6.14. In the Figures, the scale of the Etalon-2 results is twice that of the Etalon-1 results.

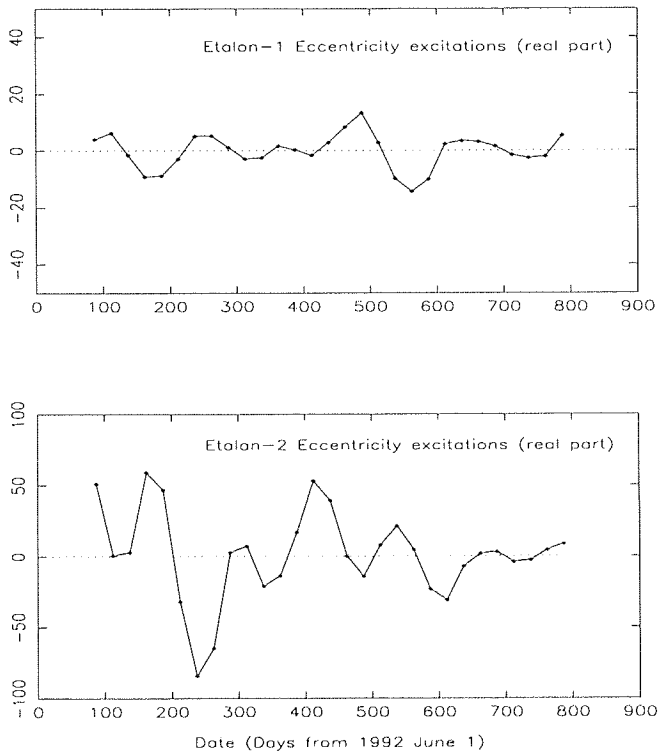


Figure 6.13: Real part of eccentricity excitation vector.

We see that for Etalon-1 both the real and imaginary parts of the excitation vector show a smooth periodic variation with amplitude about 10 mas $y^{-1}$. A periodogramme analysis suggests that annual and semi-annual terms dominate these variations. However for Etalon-2 the real part of the excitation shows a large oscillation during the first 350 days, reaching an amplitude of about 80 mas $y^{-1}$, followed by a smooth variation with an amplitude of about 20 mas $y^{-1}$. The imaginary part of the Etalon-2 excitation shows little of the large variation of the real part, although the amplitude of the oscillations reach levels of about twice those of the equivalent Etalon-1 series. Tapley *et al* [71] point out that errors in the odd degree diurnal and semi-diurnal ocean tide coefficients cause

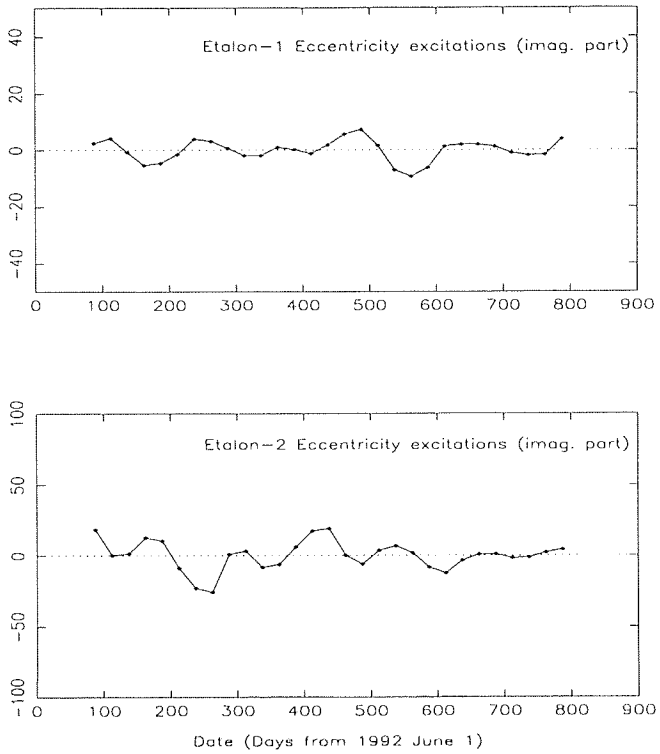


Figure 6.14: Imaginary part of eccentricity excitation vector.

variability in both the real and imaginary parts of $\Psi_p$, whilst variability in the odd zonal harmonics cause variations with the same spectrum in the real part of $\Psi_p$. Their results for the real part of the Lageos eccentricity excitation vector shows an annual periodicity, and for the imaginary part a periodicity of 560 days, or the period of rotation of the Lageos' node with respect to the Sun. As we have seen, the equivalent period for the Etalon satellites is close to one year (353 days). We also see that the amplitude of the Lageos excitations is about 100 mas $y^{-1}$, or ten times that of our Etalon-1 results. This factor of ten may be expected from scaling as $(a_e/a)^3$ for say variations in gravity field or tidal terms of degree 3, with $a_{Lageos} = 12400km$ and $a_{Etalon} = 25400km$ giving a factor of about 9. Thus we consider that the forcing mechanism that we are observing in the Etalon results is the same as that in the results of Lageos, and the similarity in the periods of the real and imaginary series of Etalon-1 suggests that they are caused by errors in

the odd degree diurnal and semi-diurnal ocean tide coefficients. However, as Tapley *et al* [71] point out the implied corrections to the degree 3 tidal terms are un-realistically high, and do not agree with results from Starlette.

For the Etalon-2 analysis, we noted in the previous sub-section the similarity between the first 350 days when the large oscillation in the eccentricity series occurs (Figure 6.13), and the period of anomalous behaviour of the Lageos eccentricity residuals. In their study of that effect, Tapley *et al* [71] show that almost all the variability appears in the real part of the eccentricity excitation, which is exactly the result we have for Etalon-2. The amplitude of the anomaly in the real part of the excitation (Figure 6.13) reaches +50 and -80 mas $y^{-1}$, compared to about +250 and -300 for Lageos, a factor of only three, which would tend to support our contention that the anomalous behaviour is satellite-specific and not a force obeying an $(a_e/a)$ power law.

In recently published work Martin and Rubincam [74] have used a four-year series of satellite-based measurements of reflected light from the surface of the Earth to deduce the effect of albedo radiation on the orbit of Lageos. In their discussion of the effect on the eccentricity excitation vector, they find that albedo radiation could account for more than 50% of the observed fluctuations in the real part of the eccentricity excitations, and nearly all the observed effects in the imaginary part, provided that the sign of the computed excitations is changed. They conclude that some albedo modeling error in previous analyses has forced a corruption of some of the terms in the current ocean tidal models. However, they also show that the measured albedo effect cannot explain the anomalous Lageos excitation during 1987, which supports our claim for Etalon-2 that the anomalous excitation is related to that particular satellite and not to an external force that should also cause similar changes in Etalon-1.

In order to remove these effects from the Etalon-2 eccentricity residuals, we have added to our force model a set of piecewise continuous once-per-revolution empirical radial accelerations. The accelerations were solved for over intervals of time broken by the onset and ending of eclipse seasons. Thus the five eclipse seasons encountered by Etalon-2 during the period of the analysis lead to 11 intervals during which a single once-per-revolution acceleration was solved for. The post solution range residual rms fell from 44 cm to 22 cm after this solution was carried out. Again the range residuals were

mapped into orbital element residuals, and we show in Figure 6.15 the eccentricity series, where the results from Etalon-1 are of course unchanged from those shown in Figure 6.12.

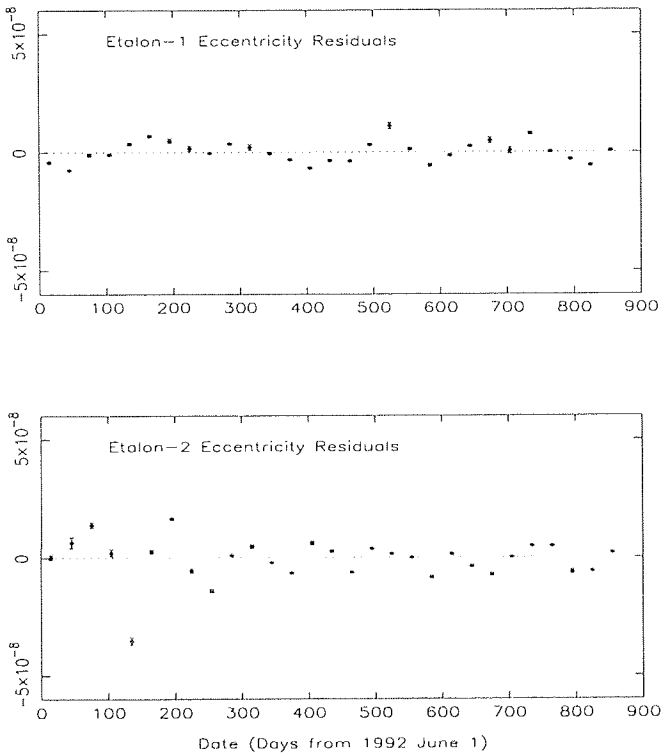


Figure 6.15: Post-solution Eccentricity Residuals - empirical 1-per-rev radial terms removed from Etalon-2.

Most of the anomalous behaviour in the Etalon-2 results has been removed, but unfortunately the small-amplitude periodicity has also been absorbed, when compared to the results in Figure 6.12, and compared to the Etalon-1 data.

### 6.3.5 Conclusion

In this chapter we have investigated the along-track accelerations on the Etalon satellites, as determined both from the single empirical drag coefficients and from the range residuals from the long-arc solutions mapped into along-track accelerations. We find that the average accelerations of some -0.1 pm $s^{-2}$ may be adequately explained by the Yarkovsky

effect, or heating by IR from the Earth, which could account for an acceleration of up to -0.46 pm $s^{-2}$, dependent upon the directions of the satellites' spin axes. There is thus no need to propose any charged or neutral-particle drag.

We find that the large acceleration 'spikes' of some 2 pm $s^{-2}$ associated with eclipse seasons may be modelled using the Yarkovsky-Schach effect, whereby a net acceleration is generated by the cooling and subsequent re-heating of the retro-reflectors during each shadow passage. This effect is sensitive to the direction of the satellites' spin axis, and we propose that both appear to be undergoing change during the period of the analysis, and in particular we speculate that Etalon-1 may be undergoing a dramatic change in the direction of its spin axis. However we find that uncertainty in the evolution of the spin axes directions means that we are unable to remove residual accelerations in the results using the Y-S model alone in the orbit determination process, and we resort to solution of empirical along-track accelerations. We further find that the results imply corrections to our Earth albedo model at small phase angles, although some of these corrections are perhaps absorbing radial force model errors due to the Y-S effect. The final post-solution residual rms values are 15cm for Etalon-1 and 44cm for Etalon-2. Thermal effects on the satellites can also cause un-modelled changes in orbital eccentricity, and we have investigated this effect using the residual eccentricity series from the long-arc solution, and by computing eccentricity excitation vectors from the eccentricity and perigee residual series. The real parts and imaginary parts of the Etalon-1 eccentricity excitations show regular fluctuations at annual and semi-annual periods, and amplitude equivalent to about 25 cm. This appears to be the same effect that is observed in discussions of the Lageos excitations, taking into account the greater height of Etalon-1, but is considered too large to be caused by an error in tidal terms [71]. However, the recent work by Martin and Rubincam [74] does suggest that there may indeed be some corruption of terms in the current ocean tide models due to previous albedo modelling error.

However the Etalon-2 eccentricity residual series shows a large anomalous departure during the first year, equivalent to an orbital error of more than 1.3 m. The real part of the eccentricity excitation shows this anomalous behaviour clearly, but the imaginary part does not. This is exactly the same behaviour as was observed by Tapley *et al* [71] during the anomalous stages of the Lageos orbital solutions of 1987 and 1991. That only Etalon-

2 and not Etalon-1 shows this behaviour strongly suggests that the cause is related to the satellite itself, such as some further thermal effect, and not to an un-modelled external force, which should affect both satellites.

Having tried to account for the effects of the thermal thrust accelerations, we move on in the next Chapter to consider systematic signatures in the node residuals, and expand our parameter set to include possible solution for selected near-resonant terms in the gravity field expansion, station coordinates and Earth rotation parameters.

# Chapter 7

# Geodetic Results from Analysis of Long-arc Orbits

## 7.1 Introduction

We now take our long-arc orbital solutions from which the effects of non-gravitational along-track accelerations have been removed as described in Chapter 6, and again map the range residuals into corrections to orbital elements. We continue the theme of analysis of these orbital element residuals by extending the analysis to the residual series in the node and inclination and then solve simultaneously for corrections to selected terms in the gravity field model, to Earth rotation parameters and to the IERS [20] value for $GM_{Moon}$. The final stage in the analysis is to solve for corrections to the station coordinates and also to systematic measurement errors for those stations left out of the initial solutions because of apparent observational biases.

## 7.2 Nodal residuals and UT1.

### 7.2.1 Introduction.

We wish to evaluate the use of orbit determination of the Etalon satellites for studying changes in the orientation of the Earth, and in particular for determination of UT1. To do this we must examine un-modelled effects on the orientation of the orbit planes that would contaminate any such determination. From analyses of tracking data to Lageos it

has been shown that secular and periodic changes in the zonal harmonics of the gravity field cause perturbations of the orbit and corresponding accelerations in the longitude of the node. These accelerations are indistinguishable from unpredictable changes in UT1, and thus limit the use of Lageos for long-term determination of this quantity. Indeed the effects on the orbit plane have been used in conjunction with an independent UT1 series derived from VLBI to obtain precise estimates of $\dot{J}_2$ [31, 32] consistent with that expected from secular changes in the Earth's polar moment of inertia due to viscous rebound following the last deglaciation, as well as seasonal variations in $J_2$ apparently driven by seasonal atmospheric mass re-distribution [75, 72]. In this section we estimate the theoretical sensitivity of the Etalon satellites to temporal changes in the gravity field, and use our our nodal residual series to decide whether they contain information on the variations that are not so far modelled in our orbit determination process. We also decide whether or not we would expect significant corruption to values of UT1 derived from Etalon analyses.

### 7.2.2 Perturbations due to variations in even zonal harmonics

A satellite's node $\Omega$, argument of perigee $\omega$ and mean anomaly $M$ are particularly sensitive to variations in the even zonal harmonic coefficients. The node may also be affected by un-modelled variations in inclination $I$. Using the linear perturbation theory developed by Kaula [52], and the Lagrange planetary equations we can express the acceleration in $\Omega$ caused by rates of change $\dot{J}_2$, $\dot{J}_4$, $\dot{J}_6$ and $\dot{I}$ by summing the contributions of each of these changing quantities [31].

$$\ddot{\Omega} = \frac{-3n}{2}\left(\frac{a_e}{a}\right)^2 \frac{\cos I}{(1-e^2)^2}\left(\dot{J}_2 + \dot{J}_4 f_4 + \dot{J}_6 f_6 - \dot{I}\tan I J_2\right), \tag{7.1}$$

where the functions $f_4$ and $f_6$ are

$$f_4 = \frac{5}{8}\left(\frac{a_e}{a}\right)^2 (7\sin^2 I - 4)\frac{(1+\frac{3}{2}e^2)}{(1-e^2)^2} \tag{7.2}$$

$$f_6 = \frac{35}{64}\left(\frac{a_e}{a}\right)^4 (8 - 36\sin^2 I + 33\sin^4 I)\frac{(1+5e^2+\frac{15}{8}e^4)}{(1-e^2)^4} \tag{7.3}$$

For the Etalon satellites, we have $I \approx 65^o$, $e \approx 0$, so $f_4 = 0.069$ and $f_6 = 0.002$, which are sufficiently small that they can be ignored. Thus the principal effects on the node are the $\dot{J}_2$ and $\dot{I}$ terms of (7.1), which we can now re-write

$$\ddot{\Omega} \approx \frac{-3n}{2}\left(\frac{a_e}{a}\right)^2 \cos I(\dot{J}_2 - \dot{I}\tan I J_2) \tag{7.4}$$

Thus the acceleration of the node caused by a linear change in $J_2$ is

$$\ddot{\Omega} \approx -0.536 * 365.25(\dot{J}_2 - 2.32 \times 10^{-3}\dot{I})\text{rads yr}^{-2} \tag{7.5}$$

We can estimate the value of un-modelled linear changes $\dot{I}$ from our series of inclination residuals. Figure 7.1 shows the series of inclination residuals for the two satellites. The residuals are shown with 1-sigma error bars, and the full lines are fitted linear functions. The linear terms defining each of the straight lines are $+0.55 \pm 1.03$ mas yr$^{-1}$ and $-1.92 \pm 2.11$ mas yr$^{-1}$ for Etalon-1 and Etalon-2 respectively. The rates of change of $I$ are thus statistically insignificant and may be assumed to be zero, so we conclude that the acceleration of the node $\ddot{\Omega}$ is not corrupted by un-modelled inclination variations. So equation (7.5) may be written

$$\ddot{\Omega} \approx \text{-195.8 } \dot{J}_2 \text{ rads yr}^{-2} \tag{7.6}$$

The value of $\dot{J}_2$ modelled during the computation of the JGM gravity field models is $\dot{J}_2 = -2.6 \times 10^{-11} yr^{-1}$ [73] this being a 'lumped' value since it cannot be separated from possible variations in higher order zonal coefficients. This effect can be appreciated if we evaluate the inclination functions (7.2 and 7.3) using the parameters of Lageos' orbit, when we find $f_4 = 0.37$ and $f_6 = 0.08$. Thus the JGM value of $\dot{J}_2$ is inseparable at the approximately 40% level from possible $\dot{J}_4$ and $\dot{J}_6$ variations [76, 31]. Now for the Etalon analyses we use the JGM value of $\dot{J}_2$ in (7.6) and obtain $\ddot{\Omega} \approx +1.04$mas yr$^{-2}$ which is the secular acceleration effect of $\dot{J}_2$ on the node of the Etalon satellites. We note that the corresponding acceleration of the node of Lageos' orbit is approximately $-14$mas yr$^{-2}$. We now use our series of nodal residuals to determine whether we might expect to be able to use the analyses to improve upon this estimate of $\dot{J}_2$.

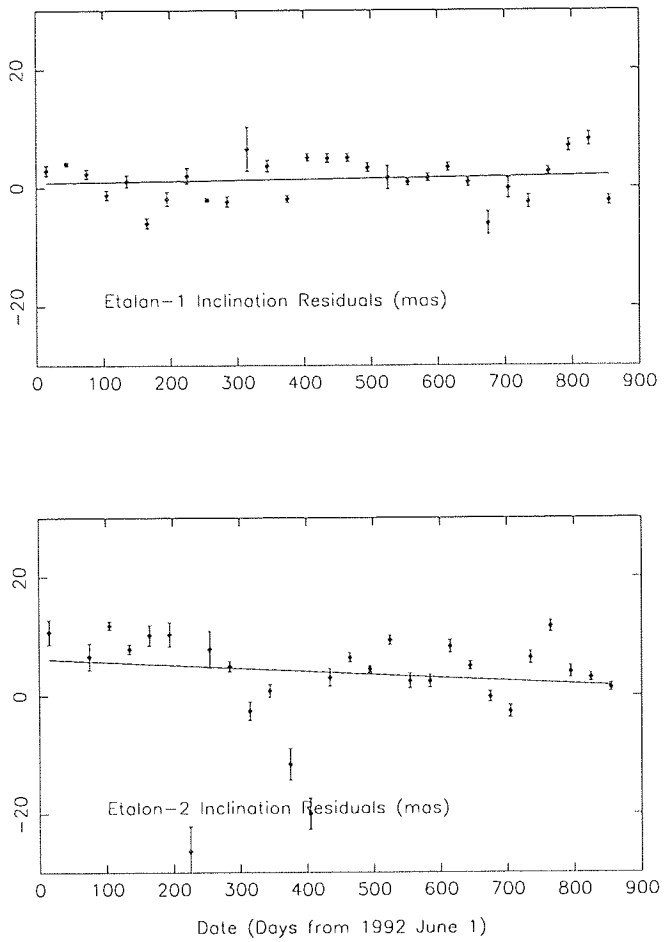


Figure 7.1: Etalon Inclination Residuals

### 7.2.3 Nodal Residuals

In Figure 7.2 are shown the series of nodal residuals for the two satellites, expressed in milli-arc-seconds (mas). Both sets of residuals have a negative slope, the values on average changing by about 10 mas over the 2.5 year period of the analysis. This small slope shows that the Etalon orbital planes very closely approximate an inertial reference system, and that the force model represents very well the gravitational accelerations on the satellite. We have carried out many test solutions while modelling the thermal forces on the satellite, and found that the nodal residuals changed very little, particularly the slope, which remained small.

We carried out a weighted least squares fit of a quadratic curve to the nodal residuals of each satellite that are shown in Figure 7.2. We obtained the following results, where $t$ is expressed in years from the mid-epoch of the analyses and the coefficients and their standard errors are expressed in mas. Such a definition of the origin of time $t$ reduces

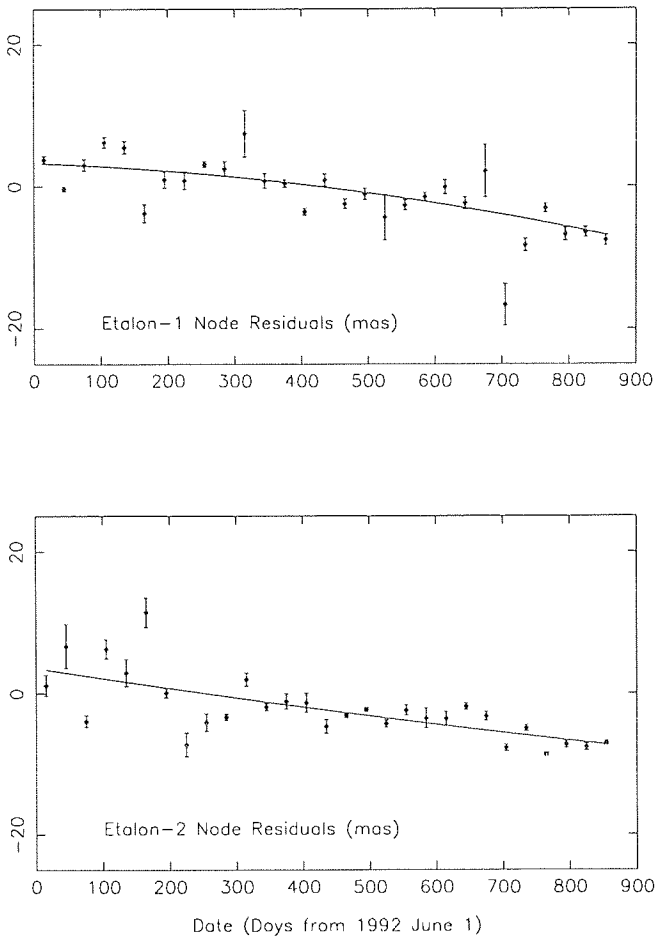


Figure 7.2: Etalon Nodal Residuals

the correlations that exist between the linear and quadratic terms.

$$\Delta\Omega_{et1} = +1.93 \pm 0.90 + (-3.43 \pm 0.88)t + (-2.34 \pm 1.41)t^2$$

$$\Delta\Omega_{et2} = -2.55 \pm 0.98 + (-4.57 \pm 0.96)t + (+0.30 \pm 1.55)t^2$$

The fit to the Etalon-2 residuals was repeated after omitting the first 400 days of values, to avoid the period of most scatter. However this measure had only minimal effect on the coefficients of the fitted curve.

We can emphasise the sensitivity of the nodal residuals to the quality of the gravity field model by experimentally changing it. A convenient test is to 'switch off' the relativistic terms that we discussed in Chapter 4, since they directly affect the precession of the orbital planes. We know that these effects were modelled when the gravity field was generated [29] and we argued in Chapter 4 that our force model must also include the effects in order that we calculate accelerations on the satellite that are compatible with

the coefficients of the field. We now omit the relativistic terms from the force model, and used the Etalon-1 data to fully converge the solution as before, solving for initial state vector and the series of empirical along-track accelerations and albedo scaling factors. The post solution range residual rms was 17.5 cm, compared to 15.0 cm when relativity was modelled. Again we mapped the range residuals into orbital element residuals as before. The nodal residuals from this solution are shown in Figure 7.3, from which

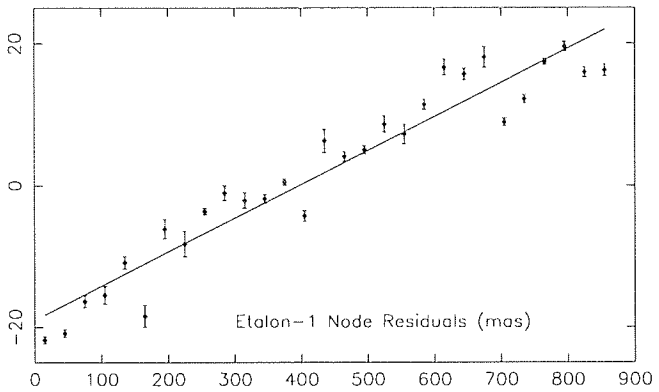


Figure 7.3: Etalon Nodal Residuals - Relativistic terms omitted

we see that there is now a much larger slope in the results. A straight line fit to these residuals has slope $+17.50 \pm 1.04$ mas $y^{-1}$. If we compare this slope to the slope of $-4.93 \pm 1.03$ obtained when we include the relativity terms, we see that the effect on the nodal residuals of leaving out the terms is to impart a slope of $+22.5$ mas $y^{-1}$. Huang *et al* [33] find that geodesic precession is the largest of the relativistic precessional terms, and causes a precession of a satellite's node of $19.2 \cos\epsilon$ mas $y^{-1}$, where $\epsilon$ is the obliquity of the ecliptic ($\approx$ 23.5 degrees). So the geodesic precession effect is approximately 17.6 mas $y^{-1}$, which agrees reasonably well with our change in the slope of the nodal residuals of 22.5 mas $y^{-1}$. The point is that the relativistic effects are not absorbed by adjustment of the initial state vector and along-track accelerations on the satellite. Of course, had we solved for corrections to some of the zonal coefficients of the gravity field we could have removed the slope in the nodal residuals, but our intention here is simply to show that the JGM-3 field and corresponding force model represents very well the accelerations on the satellite, as demonstrated by the small size of the nodal residuals shown in Figure 7.2

This experiment is of course not a test of the theory of the effect of General Relativity on an Earth orbiting satellite. It merely confirms that we have implemented correctly the effects derived by Huang *et al* [33] and which were implemented in the JGM gravity field models. To carry out a true test of the relativistic effects that would be independent of the gravity field model in use, we would need to analyse tracking data from two satellites in supplementary orbits; that is such that $I_{satA} + I_{satB} = 180^o$. For such a system, signatures in the nodal residuals due to errors in the coefficients of the gravity field would be equal and of opposite sign for the two satellites, leading to a separation of the true relativistic effects. The Lageos-III mission was proposed for this purpose [77] and may be launched sometime in the future as a collaboration between NASA and the Italian Space Agency ASI. The results here that demonstrate the stability of the orbital planes of the Etalon satellites suggest that satellites at these heights would be particularly useful for relativity experiments. A third Etalon satellite at an orbital inclination of approximately 115 degrees would be required.

We now return to our Etalon-1 and -2 nodal residuals as shown in Figure 7.2, and the fits of quadratic curves to them. We discuss whether we might be able to obtain a correction to the value of $\dot{J}_2$ that is implicit in the JGM gravity field models, and which was determined from Lageos analyses. Any error in the assumed value of $\dot{J}_2$ would impose a quadratic term onto the nodal residuals. As we have seen, for the Etalons the contribution to such a nodal acceleration of possible secular change in $\dot{J}_4$ and higher degree terms is less than 7% of the contribution of $\dot{J}_2$, since from (7.2) the inclination function $f_4 \approx 0.07$.

The presence of the significant linear terms in the fitted curves suggests that the zonal harmonic coefficients in the gravity field may require revision, which we investigate in a following section. However, the inconsistency and large standard errors associated with the quadratic terms of each curve implies that we do not have the sensitivity to derive a meaningful correction to the adopted value of $\dot{J}_2$. As we have seen, this lumped value of $\dot{J}_2$ would cause an acceleration of the node of the satellites of about $+1.0$ mas $y^{-2}$, and to be of use in contributing to a determination of the value of $\dot{J}_2$ separated from higher-order effects, we would need to determine this acceleration to a precision of about 0.1 mas $y^{-2}$. We see that our standard errors are at least an order of magnitude greater than this. Of

course, the error will reduce and solution stability will improve as we extend the data set, and with quadratic improvement with time should reach a level of about $0.2 \times 10^{-11}\mathrm{yr}^{-1}$, were we to analyse an eight-year data set. For the present analyses however, we cannot obtain a useful check on the important question of the value of $\dot{J}_2$.

However, this insensitivity of the plane of the orbits to gravity field variations is an advantage to our investigation into the use of the data for the determination of UT1.

### 7.2.4 Solution for UT1-UTC

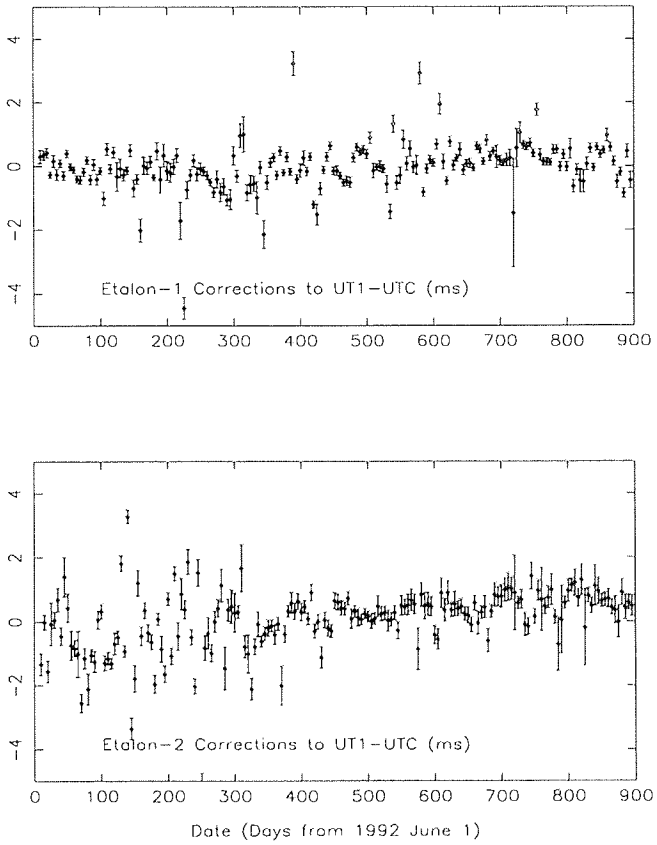


Figure 7.4: Corrections (ms) to IERS values of UT1-UTC

We now carry out a solution for corrections to the IERS series of UT1-UTC, using the partial derivatives in RGODYN as described in Chapter 4. We solve for the corrections at five-day intervals, simultaneously with the other parameters of the force model. The results are shown in Figure 7.4, where each point is shown with error bars of length 1-$\sigma$.

These corrections to the IERS values of UT1-UTC are seen to be fairly scattered about a mean which is close to zero. Most of the scatter is contained within a band of about $\pm$ 1 ms. Again the first year of results from Etalon-2 exhibit much greater scatter, with larger

error bars emphasizing this. It is of course impossible to separate short-term errors in the satellite force model, giving rise to systematic nodal residuals, from true fluctuations in UT1-UTC. However, the quoted uncertainties in the IERS values of UT1-UTC are better than 0.1 ms, and we must therefore assume that most of the occasional large discrepancies are probably due to lack of tracking data during the periods concerned. It is clear however, that as predicted from the small slope in the nodal residuals, the systematic drift-off of the Etalon series of UT1 values from the IERS series is very small. As we have already noted, the long-term stability of the IERS series depends upon VLBI results, as uncertainties in the force model for the Lageos satellites, in particular the sensitivity of their orbital planes to unpredictable atmospheric mass changes, means that in practice the Lageos node exhibits unmodelled drifts of 0.5 ms/month, and UT1 estimates using them have useful accuracy only for periods shorter than about 60 days [78]. We can emphasize the

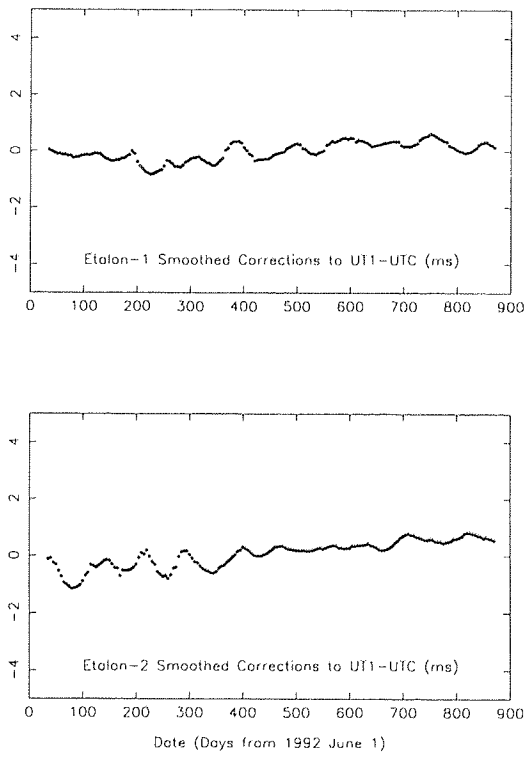


Figure 7.5: Smoothed Corrections (ms) to IERS values of UT1-UTC

stability of the Etalon series of UT1 over the 2.5 year period by smoothing the results shown in Figure 7.4. We carried out a Gaussian smoothing of the two UT1 series whereby we form a moving average by weighting neighbouring points by the ordinate values of a Gaussian of FWHM 40 days. The value of the FWHM was chosen such that the random

scatter is reduced, but any systematic features are retained. The results are shown in Figure 7.5.

The results show clearly that most departures of the values of UT1 from the IERS values are less than 0.5 ms, and that any long-term slope in the values giving rise to a drift-off is at the level of less than 0.1 ms $yr^{-1}$.

We conclude that the Etalon satellites are much better for long-term determination of UT1-UTC than the Lageos satellites.

## 7.3 Solution for coefficients of the gravity field

We now use our long-arc analyses to investigate the possibility of solving for selected terms in the gravity field JGM-3. We noted in the previous Section the presence of significant linear terms in the nodal residuals of both satellites which might imply that some even zonal harmonic terms may need revision. We may expect also to find significant changes to some odd zonal harmonic terms since Nerem *et al* [29] point out that the gravity field coefficients were estimated together with once-per-revolution empirical drag terms for some low satellites, in order to accommodate non-gravitational forces. This procedure tends to absorb errors in the odd zonal coefficients, and we have not estimated once-per-revolution terms in this analysis. We also quoted in Chapter 5 the findings of Lucchesi and Nobili [51] that the Etalon satellites are in close resonance with some of the tesseral terms of the gravity field, namely the $C_{2,2}$, $S_{2,2}$, $C_{3,2}$, $S_{3,2}$ and $C_{4,4}$, $S_{4,4}$ terms. Thus we carried out a solution for corrections to the zonal harmonic terms $J_2$, $J_3$ and $J_4$, along with the above tesseral terms.

However, the results proved to be unsatisfactory, and call into question our strategy of solving for just a few selected terms. Using the two satellites we obtained corrections to several of the coefficients that were significantly different, and we also found that some corrections were un-realistically large when compared to the standard errors of the coefficients of the JGM-3 model quoted by Nerem *et al* [29]; in some cases our corrections were more than an order of magnitude greater that the standard errors. We consider it likely that the coefficients were acting as 'soak–up' parameters, helping to remove remaining force model errors. Thus we do not present any results here, but note that a

better strategy, beyond the scope of the current work, would be to compute the normal equations matrix for a full solution of gravity field coefficients to say degree and order ten, and add it to the JGM-3 covarience matrix. Subsequent inversion would then properly accomodate into the solution the contribution of the Etalon data.

## 7.4 Solution for $GM_{Moon}$

One of the mission objectives of the Etalon satellites is a good determination of the product of the gravitational constant with the mass of the Moon, $GM_{Moon}$ [3]. We showed in Chapter 5 that there exist secular perturbations of the mean inclination and node of the Etalon orbits, and that the effects are different for the two satellites. This behaviour is attributed to the combined effects of the luni-solar perturbations and the Earth's oblateness, and is different for each satellite because of the different configuration of the orbital planes with respect to those of the Moon and Sun. We argued that such a dependence of the orbits on the Lunar perturbations should lead to an estimate of the value of $GM_{Moon}$, which could be compared to the IERS standard value [20].

During the course of the investigation, we carried out many test solutions for corrections to the IERS value of $GM_{Moon}$, where other parameters in the solution were alternately held fixed or solved for simultaneously. In this way we found that the correlation between $J_2$ and $GM_{Moon}$ was as expected very high, since both perturbations cause a precession of the orbital planes of the satellites. During the course of our 2.5-year analysis, the Lunar orbit itself precesses by only $(2.5/18.6) \times 360 = 48$degrees, thus providing only a small variation in the Lunar perturbation and very little separation of the two effects.

We also found that whether or not we applied the IERS-determined corrections $\delta\Psi$ and $\delta\epsilon$ to the nutation values had a large effect on the derived correction to $GM_{Moon}$. For example from the Etalon-1 analysis we have a correction $\Delta\ GM_{Moon} = +0.354 \times 10^8 \pm 0.247 \times 10^7\ m^3\ s^{-2}$ when using un-corrected nutation values, and $\Delta\ GM_{Moon} = -0.481 \times 10^7 \pm 0.251 \times 10^7\ m^3\ s^{-2}$, an order of magnitude smaller, when correcting the nutation series. Using the latter correction, we have for the Earth-Moon mass ratio a value of $0.012300022 \pm 0.000000008$. This ratio is to be compared to the IERS [20] value of the

ratio of 0.012300034, or the IAU(1976) value of 0.01230002, and suggests that the Etalon-1 results are consistent with the currently adopted value of $GM_{Moon}$. The results from Etalon-2 are somewhat larger than those from Etalon-1, but again are only marginally statistically significant.

We conclude that our analysis does not contradict the IERS value of $GM_{Moon}$, but that a more statistically significant result will be forthcoming only after many years of tracking the satellites. Ideally a span of 18.6 years is required to separate the effects of the lunar perturbation from that of the Earth's gravitational field.

## 7.5 Station Coordinates and Observational Bias

### 7.5.1 Introduction

In this Section, we use our long-arc solutions to solve for corrections to the coordinates of the tracking stations, and to deduce corrections to observations that are clearly erroneous, most of which were removed from the analyses at an early stage. We remarked in Chapter 5 that there are only very few occasions when more than one station is tracking the satellites at the same time, so we are unable to use a short-arc technique such as that of Sinclair [81] to improve the initial estimates of the coordinates of the tracking stations. Thus we confine our station coordinate study to a comparison between the reference frame defined by the coordinates deduced from the present analyses and that of the ITRF.

### 7.5.2 Station Coordinates

We have approached the solution of the station coordinates in two ways, neither of which attempts to correct the station velocities which have been determined from long series of laser range and VLBI observations. First we carried out a solution for corrections to the initial set of ITRF-93 station coordinates by solving for corrections to all the coordinates in a simultaneous solution with Earth rotation parameters, using the entire 2.5 year orbits. We found that including station coordinates as parameters in the solutions improved slightly the post-solution residual rms, to 13 cm and 30 cm respectively for Etalon-1 and 2. Second, we carried out the same solutions over consecutive 50-day sections of the data sets, where we found that in most cases the residual rms improved to 5 cm or better. The

results for the corrections to the IERS values of UT1-UTC were reported in the previous Section. Also we found only minor, somewhat noisy corrections to the IERS series of $x_p$ and $y_p$, and do not discuss them further here. For the station coordinate solutions, we have characterised the results by a comparison of the reference frames defined by those coordinates with that implied by the ITRF93, by solving for the coefficients of a seven-parameter mapping of our station coordinates onto those of the ITRF-93 set. The parameters are three orthogonal translations ($\Delta$ X, Y, Z), three rotations, about the X, Y, Z axes and a scale factor. The results for the long-arc solutions are shown in Table 7.1, where it is clear that there are no significant differences between the reference frames defined by our Etalon analyses and that of the ITRF. This is a useful result, providing an independent check at the level of a few cm on the ITRF reference frame which is determined through a combination of analyses of LAGEOS data and results from VLBI and GPS.

| | Etalon-1 | | Etalon-2 | |
|---|---|---|---|---|
| Parameter | | s.e | | s.e |
| $\Delta$ X (cm) | 2.5 | 4.1 | 1.2 | 6.7 |
| $\Delta$ Y (cm) | 4.8 | 4.1 | 3.1 | 6.6 |
| $\Delta$ Z (cm) | 2.2 | 3.8 | 6.6 | 6.2 |
| X Rot (mas) | -1.57 | 1.57 | 0.46 | 2.53 |
| Y Rot (mas) | 1.53 | 1.66 | -0.88 | 2.70 |
| Z Rot (mas) | -0.54 | 1.45 | -0.74 | 2.34 |
| Scale | 0.563D-08 | 0.601D-08 | 0.994E-08 | 0.966D-08 |

Table 7.1: 7-parameter fit of station coordinates onto ITRF93

The results from the 50-day solutions again show no significant scale or rotation relative to the ITRF frame but, unlike the long-arc solutions, do show a significant, varying translation in the Z-direction. This series of 'Z-shift' values is shown in Figure 7.6, where we see that most of the values from the Etalon-1 analysis are within $\pm$ 15 cm of zero, but that some of the Etalon-2 values are much larger, particularly during the first 400 days of results.

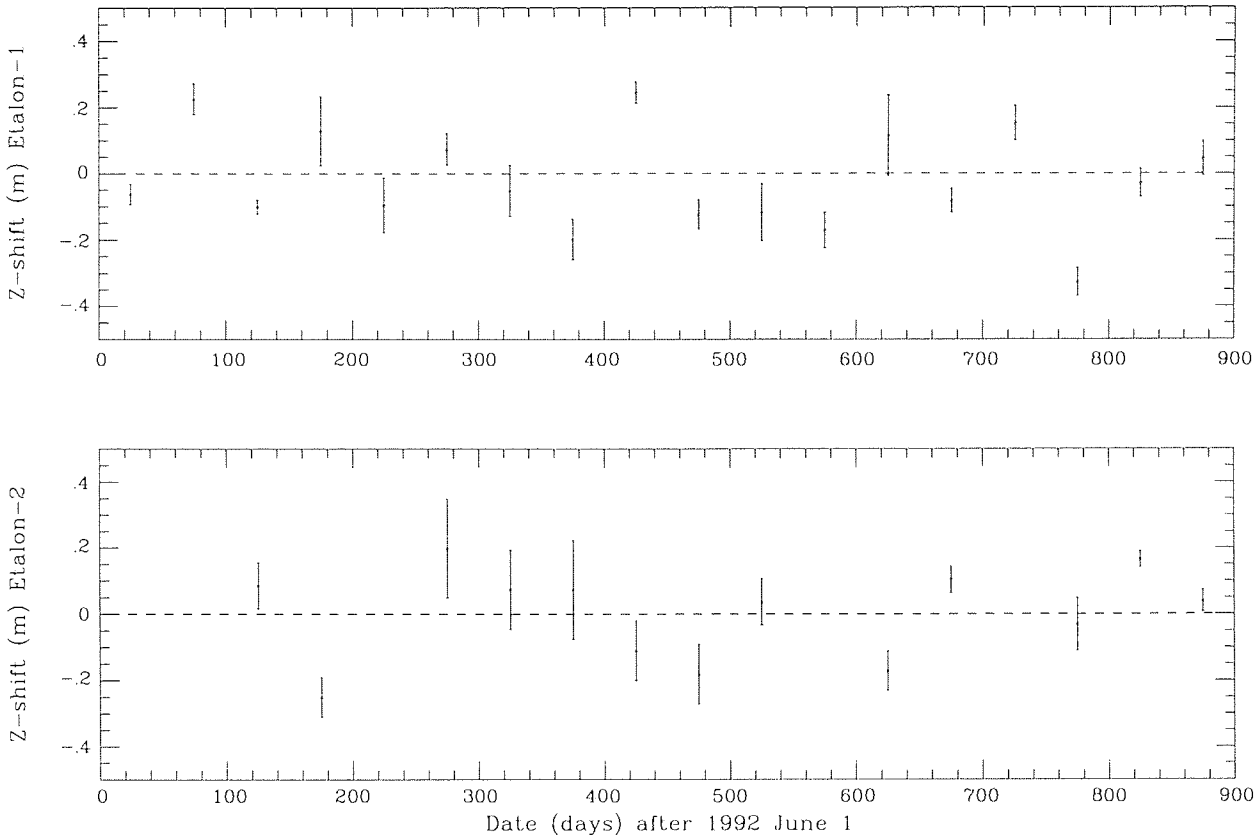


Figure 7.6: Z-shift between 50-day solutions and ITRF93

The Z-shift values are at the level of proposed seasonal variations in the centre of mass of the Earth, as determined by GPS analyses relative to the mean reference frame of ITRF93 [82]. However a periodogramme analysis of the results shown in Figure 7.6 does not identify any strong periodicities. A possible alternative cause of the Z-shift variations could be an uneven distribution of tracking stations, with often only one or two stations in the southern hemisphere contributing to the observations. A similar conclusion was reached by Vigue *et al* [83], to explain similar variations in the Z-component of the geocentre determined from an international GPS campaign.

### 7.5.3 Observational Bias

We now return to the stations whose observations were initially excluded from the solution. We remarked in Chapter 5 that the range observations from some stations appeared to be biased with respect to the orbit fitted to the majority of the data, and that such

observations were making it difficult to obtain a converged solution, particularly during periods of sparse data coverage. This is a particularly important problem for the SLR technique, as biased data is very difficult to detect during, for example, orbit determination of a low satellite such as ERS-1, when data spans of just a few days duration are frequently considered and erroneous data can easily corrupt the solution. Having now achieved a converged solution over 2.5 years for both satellites, we are in an ideal position to compare these observations with an accurate orbit, and solve for possible biases in the original measurements, which may be range bias or epoch error, or both. Such varying bias can result from temporary software or hardware faults at the observing station, or a systematic error in, for example, the assumed distance to the calibration target. Initially we calculate the difference between the observed and computed range for every observation for the stations involved. Plots of these differences in range can be a valuable aid to the diagnostic process, particularly if they show that the bias does vary with time. As an initial stage, we show in Figure 7.7 the final residuals from the fitted orbit of all

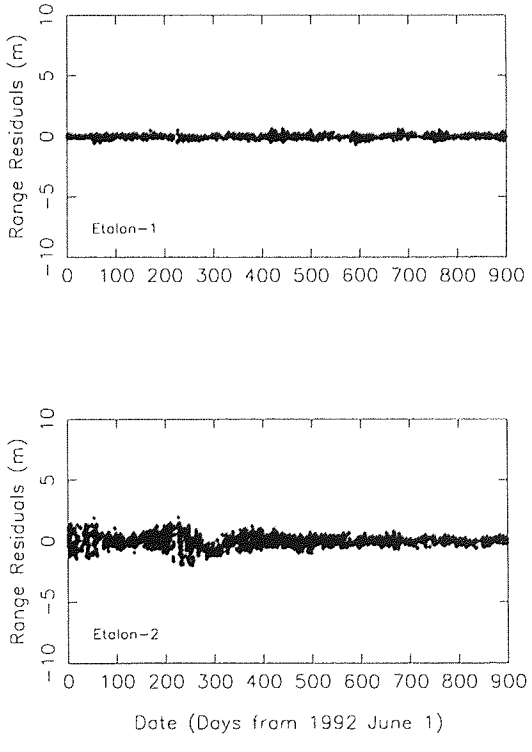


Figure 7.7: Range Residuals from Converged Solutions.

the range observations used in the analysis. The Etalon-1 results have a post solution residual rms of 15 cm and show very little evidence of remaining systematic trends. The

Etalon-2 results are, as expected, seen to contain some systematic behaviour, particularly during the anomalous first 400 days. These plots, particularly that of the Etalon-1 residuals show that the fitted orbits should readily reveal biased data from those stations suspected of having systematic measurement error.

### 7.5.4 Results.

From those stations marked with a $\star$ in Table 5.1, we find that the following stations made sufficient observations that reliable bias estimates could be determined: 1863 and 1864, Maidanak I and II, Ukraine; 7237 Changchun, China; 7502 Sutherland, South Africa; 8834 Wettzell, Germany. Figure 7.8 shows the 2.5 year history of the measurement biases of stations 8834 and 7237 with respect to the converged orbits of both satellites. The results from Wettzell clearly show that there are at least two different bias values present during the 2.5 year period, and that broadly the results from the two satellites agree with one another. By examining these plots and two similar ones for stations 1864 and 7502, we are able to partition the observations from each station into sets for which it is evident that the bias values remained constant. We then used RGODYN to solve for range and epoch bias for each of the sets of data, formed mean values over the two-satellite results, and we show these mean values along with their standard errors in Table 7.2. Included in the Table are the dates of applicability (MJD) of each set of corrections. We see that for instance station 8834 Wettzell regularly experiences a range bias of more than 35 cm, and occasional periods of larger error along with a significant epoch error.

To further test this procedure, we applied it to the data for three stations that we did not expect to have significant measurement problems. We carried out the bias solution for the observations of stations 7109 Quincy, 7939 Graz and 7840 Herstmonceux. For the Herstmonceux station in particular we have independent evidence that the monthly-averaged range bias values determined from analysis of observations of Lageos are below 1 cm in size [84]. The results, valid for the whole 2.5 year time-span, are given in Table 7.3. The corrections to the epochs are fairly large, and we consider them to be unrealistically so. Observations of these distant satellites tend to be made when the satellites are at fairly high altitude above the station, to improve the chances of obtaining returns. In this configuration, the satellite range is particularly insensitive to changes in

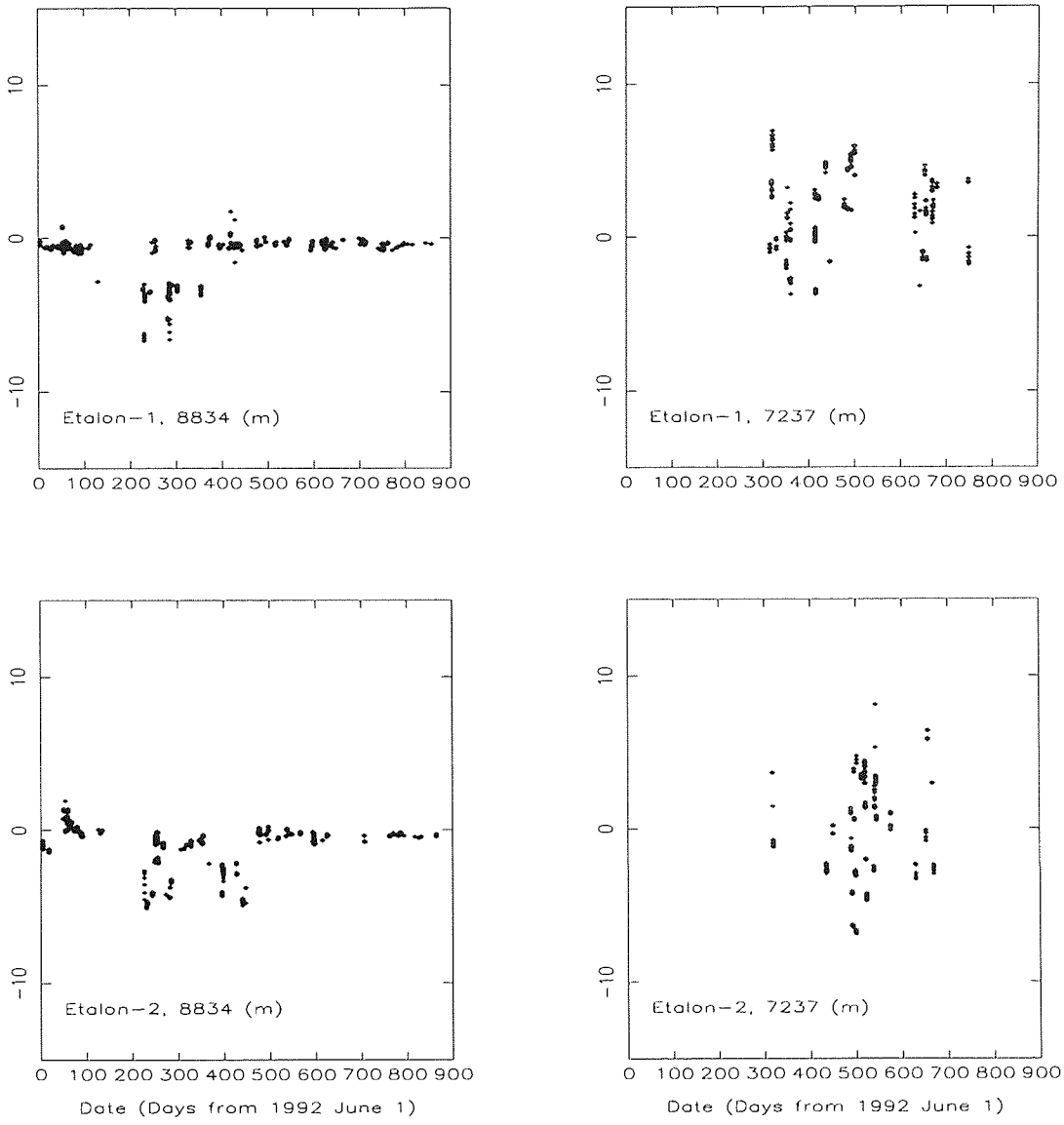


Figure 7.8: Range Residuals showing observational bias.

observational epoch, so solutions for epoch error using range measurements are liable to produce spurious results. We note that the corrections to epochs given in Table 7.2 are mostly significantly larger than those of our 'control' stations, and thus probably indicate the presence of real epoch errors. The size of the range bias values in Table 7.3, which should be fairly well-defined, show that the method is unlikely to detect range errors of less than about 5 cm, despite the very small internal standard errors associated with those quantities.

| Station | Start MJD | End MJD | ΔEpoch $\mu$s | s.e. $\mu$s | ΔRange m | s.e. m |
|---|---|---|---|---|---|---|
| 1863 | 48774.0 | 49673.0 | -3657.00 | 103.1 | - | - |
| 1864 | 48774.0 | 49673.0 | - | - | 0.021 | 0.013 |
| 7237 | 48774.0 | 49403.0 | - | - | 0.669 | 0.021 |
| 7237 | 49404.0 | 49674.0 | -138.98 | 45.1 | 1.471 | 0.115 |
| 8834 | 48774.0 | 49044.0 | - | - | -0.593 | 0.034 |
| 8834 | 49000.0 | 49018.0 | 1486.00 | 37.8 | -4.247 | 0.103 |
| 8834 | 49134.0 | 49234.0 | 499.00 | 76.7 | -0.385 | 0.080 |
| 8834 | 49234.0 | 49674.0 | - | - | -0.382 | 0.035 |

Table 7.2: Mean corrections to observation epoch and range.

| Station | ΔEpoch $\mu$s | s.e. $\mu$s | ΔRange m | s.e. m |
|---|---|---|---|---|
| 7109 | 30.1 | 10.3 | -0.044 | 0.006 |
| 7939 | -104.0 | 20.1 | -0.010 | 0.006 |
| 7840 | -233.0 | 20.7 | -0.029 | 0.006 |

Table 7.3: Mean corrections to observation epoch and range.

## 7.6 Conclusion

We have analysed the nodal residuals from the long-arc solutions from each satellite in an attempt to determine a value of $\dot{J}_2$ essentially free of corruption from variations in higher order terms of the gravity field. However, we find that our results do not have the sensitivity to allow such a determination, and conclude that a longer time-span of perhaps eight years is required to obtain a significant result. We find that the stability of the orbital planes of the satellites does allow a determination of a series of values of UT1-UTC, which departs from an inertial series by only about 0.1 ms $yr^{-1}$, which is a much better performance than possible from analysis of Lageos data, which requires frequent re-alignment with an independent source of UT1.

We find that our solutions are consistent with the currently adopted value of $GM_{Moon}$, the 2.5 year orbital analyses being of insufficient length to allow a separation of possible gravity field errors from a possible error in that parameter.

The station coordinate frame determined from the long-arc solutions agree well at the 2-4 cm level with the frame defined by the ITRF-93 station coordinates. The frames determined from station coordinate solutions at 50-day intervals show a significant variation of $\pm$ 15 cm in the z-direction with respect to ITRF-93. Possible causes are seasonal variation of the centre of mass of the Earth, or poor and variable geographic distribution of tracking stations. The long-arc orbits are also found to be of use in determining observational bias at the level of more than a few cm or a few hundred micro-seconds.

# Chapter 8

# Conclusions and Future Work

## 8.1 Conclusions

### 8.1.1 Introduction

In this Chapter we list and discuss the main conclusions of the work carried out during the course of this research. The conclusions are itemized according to their subjects, and are therefore listed in Chapter order. The final Sections discuss possible future work leading on from some of the topics discussed during this study.

### 8.1.2 Data Pre-Processing

We have developed a method of preprocessing laser range observations to remove noise events and to form normal points by fitting an orbit to the range observations obtained during a single pass. The method has been shown to work for a variety of different satellites, and we have adapted a statistical test to the problem of checking that all trends have been removed from the range residuals. The computer program is in routine use at several laser ranging systems worldwide.

### 8.1.3 Satellite Signatures and range bias

We have shown that the laser range measurements made at Herstmonceux are affected by the particular satellite being observed. We find that if the range measurements are made at a single-photon level of return, then during the course of a satellite pass the whole

return waveform is sampled, and the distribution of range residuals from a smoothing function can be accurately represented by a convolution of the laser pulse profile with the satellite impulse function and with the response function of the ranging system. We use our model to determine corrections to refer the range measurements to the centre of mass of the satellites, and show that such corrections are significantly different from pre-launch measurements which were carried out at high return levels. In particular we calculate centre-of-mass corrections for the Etalon satellites, for use later in this study.

We have also shown that for the Herstmonceux system, departure from the regime of single–photon return levels will result in range bias. We have experimentally examined the degree of bias as a function of return level from the local calibration target, over a range of from single to 1000 photons. Our model again adequately explains the observational results, and implies that finite pulse-length accounts for about half the bias, and a plausible degree of energy-dependent time-walk within the detector accounts for the remainder. For satellite ranging we find similar energy-dependent biases, which again are adequately explained by our model.

We conclude that provided calibration ranging and satellite ranging continue to be carried out at a strictly single–photon level, our normal practice, then range bias is minimal, at the expense of some loss of single–shot precision.

### 8.1.4 The SATAN SLR Analysis Package

We have outlined the principle components of the RGO SATAN analysis package, and highlighted the modifications carried out by the author as part of the present study. The main programs of the package are ORBIT and RGODYN. Program ORBIT carries out a numerical integration of the three second-order differential equations of motion of the satellite in the J2000 reference frame, and of a large number of variational equations from which partial derivatives of the satellite position with respect to a set of parameters of the force model may be computed. At each step of the integration the program forms the sum of the current components of the forces acting upon the satellite, which include the gravitational attractions of the irregular field of the Earth, the indirect attractions of the Sun, Moon and planets, and the non-conservative forces of direct and Earth-reflected solar radiation and atmospheric drag.

We have modified the force model to maintain compatibility with a new family of Earth gravity-field models which were generated using a force model which included the effects of relativity on the motion of the satellites. Such subtle effects become important when long orbital arcs are computed and compared with observations, which is a major objective of this study.

We have also carried out a study of the effect on the integration process of the satellite entering the Earth's shadow. We obtained from Herstmonceux some photometric observations of shadow passages of Lageos, in order to compare both the duration of the penumbral passage and the time of onset of the eclipse with those computed by ORBIT. Using this information we modified the program to more closely represent the time of shadow passage, but continue artificially to expand the model of the penumbral region in order that the modelled solar radiation force is only gradually removed from the force model. This work also leads to conclusions on optimum integration step sizes for the different laser satellites.

We discussed the Earth-reflected albedo model implemented in ORBIT, and modified it so that it is applicable to the high altitude geodetic satellites that are the main subject of the present study.

Program RGODYN takes laser range observations from the worldwide network of tracking stations and computes predicted range values based on the orbit computed by ORBIT. The differences between the predicted and observed ranges are used in a least-squares adjustment of a selection of a large number of force-model and geodetic parameters. These include initial state-vector of the satellite, selected terms in the expansion of the gravity field, empirical radial and along-track accelerations, station coordinates and Earth rotation parameters.

### 8.1.5 Orbit Determination of the Etalon Satellites

We carried out a preliminary orbital determination over a 6-month orbital arc of each of the two Etalon satellites, solving for initial state vectors, station coordinates and Earth rotation parameters. We compared the two sets of station coordinates with one another by solving for a seven parameter mapping of one set onto another. The parameters are three orthogonal translations, three rotations and a scale difference. We find that all

the parameters are statistically insignificant, the translation in the z-direction being the largest at 4.52 ±4.05 cm, and thus concluded that these satellites are of potential value for station coordinate determination. The solutions for UT1-UTC contain significant systematic variations with amplitude of about ± 1 ms, which suggest that un-modelled nodal perturbations exist, or that there are possible systematic effects due to periods of limited tracking data.

Following this preliminary study, we decided to investigate the stability of the Etalon orbits more fully, and we carried out long-arc solutions by fitting 2.5 years of tracking data to continuous orbits. These solutions had the specific aim of determining a stronger terrestrial reference frame, and making a better determination of the signatures in the deduced series of UT1–UTC, with a view to explaining the systematic behaviour. A further objective was to attempt to use the data to solve for corrections to some of the coefficients of the gravity field and to determine a correction to the IERS value of $GM_{Moon}$.

We found that for this long-arc work the force model used in the integration of the variational equations was insufficiently accurate to compute correctly the partial derivatives of the satellite coordinates with respect to the initial state vector. We added the luni-solar perturbations to this force model, and subsequently obtained converged solutions with post-fit range residual rms of about 2 m.

We then mapped the range residuals from the long-arc orbits into equivalent sets of residual orbital elements, for further analysis. We found that the along–track accelerations of the satellites have long–term averages of some 0.1 pico-m $s^{-2}$, upon which are superimposed annual and semi–annual terms with amplitudes of up to 2 pico-m $s^{-2}$. There were also significant signatures in the residual series of other orbital elements, in particular the eccentricity residuals.

### 8.1.6 Thermal Effects on the Etalon Satellites

We investigated the along-track accelerations on the Etalon satellites, as determined both from the single empirical drag coefficients and from the range residuals from the long-arc solutions mapped into along-track accelerations. We found that the average accelerations of some -0.1 pm $s^{-2}$ may be adequately explained by the Yarkovsky effect, (i.e. re-

radiation of heating by IR from the Earth), which could account for an acceleration of up to -0.46 pm $s^{-2}$, dependent upon the directions of the satellites' spin axes. There is no need to propose any charged or neutral-particle drag to explain the observed accelerations.

We found that the large acceleration 'spikes' of some 2 pm $s^{-2}$ associated with eclipse seasons may be modelled using the Yarkovsky-Schach effect, whereby a net acceleration is generated by the cooling and subsequent re-heating of the retro-reflectors during each shadow passage. This effect is sensitive to the direction of the satellites' spin axis, and the results can be interpreted to suggest that both are undergoing change. We were, however, unable to remove all the residual accelerations in the results using the Y-S model alone in the orbit determination process, and we resorted to the determination of a series of empirical along-track accelerations and to corrections to our Earth albedo model at small phase angles. We obtained for the 2.5 year orbits post-solution residual rms values of 15cm for Etalon-1 and 44cm for Etalon-2.

We carried out an analysis of the residual eccentricity series from the long-arc solution, by computing eccentricity excitation vectors from the eccentricity and perigee residual series. The real and imaginary parts of the Etalon-1 eccentricity excitations show regular fluctuations at annual and semi-annual periods, with amplitude equivalent to about 25 cm. This appears to be the same effect that is observed in discussions of the Lageos excitations, taking into account the greater height of the Etalon satellites, but has been considered too large to be caused by an error in ocean tidal terms. However, recently published work using space-borne measurements of Earth-reflected radiation does suggest that there could have been some corruption of terms in the current ocean tide models due to previous albedo modelling error.

By contrast, the Etalon-2 eccentricity residual series showed a large anomalous departure during the first year, equivalent to an orbital error of more than 1.3 m. The real part of the eccentricity excitation showed this anomalous behaviour clearly, but the imaginary part did not. This is exactly the same behaviour as was found by analysts of Lageos data during the anomalous stages of the Lageos orbital solutions of 1987 and 1991. That only Etalon-2 and not Etalon-1 showed this behaviour strongly suggests that the cause is related to the satellite itself, such as some further thermal effect, and not to an un-modelled external force, which should affect both satellites.

### 8.1.7 Geodetic Results from the Etalon Solutions

We analysed the nodal residuals from the long-arc solutions from each satellite in an attempt to determine a value of $\dot{J}_2$ essentially free of corruption from variations in higher order terms of the gravity field. However, we found that our results did not have the sensitivity to allow such a determination, and concluded that a longer time-span of perhaps eight years would be required to obtain a significant result. We found that the stability of the orbital planes of the satellites did allow a determination of a series of values of UT1-UTC, which departed from an inertial series by only about 0.1 ms $yr^{-1}$, which is a much better performance than possible from analysis of Lageos data, which requires frequent re-alignment with an independent source of UT1.

We attempted to solve for corrections to selected coefficients of the JGM-3 gravity field, but found that about half of the corrections were significantly different in the results for the two satellites. Also many of the corrections were un-realistically large, and we conclude that the corrections are absorbing small errors in the force model, along with possible errors in the coefficients not selected for solution.

We found that our solutions were consistent with the currently adopted value of $GM_{Moon}$, the 2.5 year orbital analyses being of insufficient length to allow a separation of possible gravity field errors and a possible error in that parameter.

The station coordinate frames determined from the long-arc solutions agreed well at the 2-4 cm level with the frame defined by the ITRF-93 station coordinates. The frames determined from station coordinate solutions at 50-day sub-sets showed a significant variation of $\pm$ 15 cm in the z-direction with respect to ITRF-93. Possible causes are seasonal variation of the centre of mass of the Earth, or poor and variable geographic distribution of tracking stations. The long-arc orbits were also found to be of use in determining observational bias at the level of more than a few cm in range and a few hundred micro-seconds in epoch.

### 8.1.8 Overall conclusion

This analysis of the Etalon observations has provided some interesting comparisons with the results from Lageos analyses, despite the relatively sparse data sets. We hope that the long-term stability of the orbits with regard to determination of UT1, for poten-

tial determination of $\dot{J}_2$ and of $GM_{Moon}$, may act as an incentive to the laser ranging community to continue to make observations of these interesting satellites.

## 8.2 Future Work

### 8.2.1 Thermal effects

The main problem with accurately modelling the thermal accelerations on the satellites is a lack of knowledge of the directions of their spin axes. It is possible that the distribution of the range residuals may contain information on these directions, since the satellites are not fully uniformly covered with retro-reflectors. This work would build on the signature work discussed in Chapter 3, and be of use in the modelling work discussed in Chapter 6.

It would be of interest to analyse a longer data set using the methods developed during this study. In particular it would be useful to check whether the acceleration spikes associated with the eclipse seasons continue to imply rapid variations in spin axis direction, and whether the year-long 'eccentricity anomaly' found for Etalon-2 repeats at a later date, and perhaps also affects Etalon-1. The periodic variations in the Etalon-1 eccentricity excitations should also be analysed further, as they may indicate that a significant error exists in some of the low frequency terms of the current ocean tidal models.

### 8.2.2 Reference frame

The demonstrated value of the Etalon satellites for determination of UT1 could be best exploited if the observations from both satellites were analysed in a simultaneous solution with both Lageos satellites. The greater tracking density of Lageos would allow for parameter determination at short time intervals, whilst the Etalon data would provide the long-term stability.

### 8.2.3 Gravity Field

The Etalon data should be used to solve for possible corrections to the JGM-3 gravity field coefficients to degree and order ten, by addition of the Etalon normal matrices to the JGM-3 covariance matrix.

### 8.2.4 Shadow passages

A significant number of photometric observations of satellite shadow passages were obtained at Herstmonceux during the course of this work. A full analysis may prove interesting for shadow boundary studies, with possible seasonal variation in shadow diameter and in density of the penumbral region. The availability of precise laser data for orbit determination of the satellites further adds to the uniqueness of this data set.

# References


[1] H. Plotkin. S66 laser satellite tracking experiment. In *Proc of the Quantum Electronics III conference*, pages 1319–1332, Columbia University Press, 1964.

[2] J.M. Bosworth, R.J. Coates, and T.L. Fishetti. The development of nasa's crustal dynamics project. In *Contributions of Space Geodesy to Geodynamics: Technology*, volume 25 of *Geodynamics Series*, pages 1–20. AGU, Washington, DC, 1993.

[3] A. Dunaev and S. Tatevian. Geodynamic satellite ETALON. The programme of the use of passive spacecraft for the solution of fundamental and applied problems in geodesy, geodynamics and geophysics. Council on the Astronomy of the Academy of Sciences USSR, Moscow, 1988.

[4] Recommendation 84a, normal points. In J. Gaignebet, editor, *Proc. 5th Int. Workshop on Laser Ranging Instrumentation.*, France, 1985. CERGA.

[5] B.E. Schutz. Quicklook normal point format. *Satellite Laser Ranging Newsletter, SLR Subcommission of the CSTG*, April 1990.

[6] A.T. Sinclair. The IRV force model and reference system. Satellite Laser Ranging Newsletter SLR Subcommission of the CSTG, June 1995.

[7] R. Wood and P. Gibbs. Timebias corrections to predictions. In *Proc. 8th Int. Conf. on Laser Ranging Instrumentation*, number 3214 in NASA Conf. Publ., pages 9.13–9.18, 1993.

[8] E.L. Crow, F.A. Davis, and M.W. Maxfield. *Statistics Manual.* Dover Publications Inc., New York, 1960.

[9] G.M. Appleby. Satellite signatures in SLR observations. In *Proc. 8th Int. Conf. on Laser Ranging Instrumentation.*, NASA Conf. Publ. 3214, pages 2.1–2.14, 1993.

[10] I. Prochazka. Single Photon Avalanche Diode Detector Package. Upgrade kit for RGO, July 1993.

[11] R.C. Wilson and H.S. Hudson. Solar luminosity variations in solar cycle 21. *Nature*, 332:810–812, 1988.

[12] M.W. Fitzmaurice, P.O. Minott, J.B. Abshire, and H.E. Rowe. *Prelaunch Testing of the Laser Geodynamic Satellite (LAGEOS)*, 1977.

[13] M Sasaki and H. Hashimoto. Launch and observational programme of the Experimental Geodetic Satellite of Japan. *IEEE Trans. on Geoscience and Remote Sensing*, GE-25(5), 1987.

[14] G. Kirchner and F. Koidl. Work at graz on satellite signatures. In *Proc. 8th Int. Conf. on Laser Ranging Instrumentation.*, number 3214 in NASA Conf. Publ., pages 2.15–2.22, 1993.

[15] J.J. Degnan. Millimeter accuracy satellite laser ranging: A review. In *Contributions of Space Geodesy to Geodynamics: Technology*, volume 25 of *Geodynamics Series*, pages 133–162. AGU, Washington, DC, 1993.

[16] R. Neubert. An analytical model of satellite signature effects. In *Proc. 9th Int. Workshop on Laser Ranging Instrumentation*, Canbera, 1995. to be published.

[17] D.A. Arnold. Transfer functions of LAGEOS. Grant NGR 09-015-002, Suppl No 57, 1987.

[18] N.T. Mironov, A.I. Emetz, A.N. Zaharov, and V.E. Tchebotarev. Etalon-1 center of mass correction and array reflectivity. In *Proc. 8th Int. Conf. on Laser Ranging Instrumentation.*, number 3214 in NASA Conf. Publ., pages 6.9–6.32, 1993.

[19] A.T. Sinclair. Data screening and peak location. In *Proc. Annual Eurolas Meeting*, pages 37–46, Munich, 1995.

[20] D.D. McCarthy, editor. *IERS Standards 1992.* Number 13 in IERS Tech.Note. Central Bureau of IERS, Observatoire de Paris, 1992.

[21] P.O. Minott, T.W. Zagwodzki, T. Varhese, and M. Seldon. Prelaunch optical characterization of the laser geodynamic satellite (LAGEOS2). NASA Tech.Paper 3400, Goddard Space Flight Centre, 1993.

[22] G.M. Appleby and P. Gibbs. Monitoring potential range biases in single-photon slr systems. In J. Luck, editor, *Proc Ninth Int. Workshop on Laser Ranging Instrumentation.*, volume 1, pages 92–102, Canberra, 1996.

[23] T. Varghese and M. Pearlman. SPAD operations on the Topex/Poseidon retroreflector array. Private Communication, September 1992.

[24] G.M. Appleby and P. Gibbs. Energy dependent range bias for single-photon-detection systems. In *Proc. Annual Eurolas Meeting*, pages 51–59, Munich, 1995.

[25] A.T. Sinclair and G.M. Appleby. A short-arc method for determination of station coordinates and baselines in the mediterranean area. In *Contributions of Space Geodesy to Geodynamics: Crustal Dynamics*, number 23 in Geodynamics Series, pages 389–396. AGU, Washington, DC, 1993.

[26] G.M. Appleby and A.T. Sinclair. European and mediterranean baselines from 10 years of Lageos observations. In *Proc. of 1st Turkish Int. Symp. on Deformations*, pages 791–799, Istanbul, 1995.

[27] L Agrotis. *Satellite Laser Ranging and the Global Positioning System.* PhD thesis, Nottingham University, 1983.

[28] W.A. Heiskanen and H. Moritz. *Physical Geodesy.* W.H. Freeman and Company, London, 1967.

[29] B.D. Tapley, M.M. Watkins, J.C. Ries, G.W. Davis, R.J. Eanes, S.R. Poole, H.J. Rim, B.E. Schutz, C.K. Shum, R.S. Nerem, F.J. Lerch, J.A. Marshall, S.M. Klosko, N.K. Pavlis, and R.G. Williamson. The Joint Gravity Model 3. *J. Geophys. Res.*, 101(B12):28029–28050, 1996.

[30] J.C. Ries, R.J. Eanes, C.K. Shum, and M.M. Watkins. Progress in the determination of the gravitational coefficient of the earth. *Geophys. Res. Lett.*, 19(6):529–531, 1992.

[31] C.F. Yoder, J.G. Williams, J.O. Dickey, B.E. Schutz, R.J. Eanes, and B.D. Tapley. Secular variation of earth's gravitational harmonic $J_2$ from LAGEOS and nontidal acceleration of earth rotation. *Nature*, 303(5920):757–762, 1983.

[32] R.J. Eanes. *A Study of Temporal Variations in Earth's Gravitational Field using Lageos-1 Laser Range Observations.* PhD thesis, University of Texas at Austin, 1995.

[33] C. Huang, J.C. Ries, B.D. Tapley, and M.M. Watkins. Relativistic effects for near-earth satellite orbit determination. *Celestial Mechanics and Dynamical Astronomy*, 48:167–185, 1990.

[34] J.C. Ries, C. Huang, and M.M. Watkins. Effect of general relativity on a near-earth satellite in the geocentric and barycentric reference frames. *Phys. Rev. Lett.*, 61(8):903–906, 1988.

[35] J.H. Lieske, T. Lederle, W. Fricke, and W. Morrando. Expressions for the precession quantities based upon the IAU(1976) system of astronomical constants. *Astron. Astrophys.*, 58(1), 1977.

[36] N.M Harwood and G.G. Swinerd. Long-period and secular perturbations to the orbits of Explorer 19 and Lageos due to direct solar radiation pressure. *Celestial Mechanics and Dynamical Astronomy*, 62:81–92, 1995.

[37] R.J. Eanes, B. Schutz, and B. Tapley. Earth and ocean tide effects on lageos and starlette. In J.T. Kuo, editor, *Proc. of Ninth International Symposium on Earth Tides*, Stuttgart, 1983.

[38] D.E. Smith, R. Kolenkiewicz, P.J. Dunn, S.M. Klosko, J.W. Robbins, M.H. Torrence, R.G. Williamson, E.C. Pavlis, N.B. Douglas, and S.K. Fricke. *LAGEOS Geodetic Analysis-SL7.1.* Number 104549 in NASA Tech. Mem. Goddard Space Flight Center, MD, 1991.

[39] R.H. Merson and A.W. Odell. The skynet orbit determination program SPOD2. Tech. Rep. 75093, Royal Aircraft Establishment, 1975.

[40] Sinclair A.T. and D.B. Taylor. Analysis of the orbits of Titan, Hyperion and Iapetus by numerical integration and by analytical theories. *Astron. Astrophys*, 147:241–246, 1985.

[41] A. Milani, A.M. Nobili, and P. Farinella. *Non-gravitational Perturbations and Satellite Geodesy.* Adam Hilger, 1987.

[42] G.M. Appleby. Directional and photometric observations of artificial earth satellites using the UK SLR system. *Planetary and Space Science*, 38(4):471–481, 1990.

[43] D. Vokrouhlicky, P. Farinella, and F. Mignard. Solar radiation pressure perturbations for earth satellites IV. effects of the earth's polar flattening on the shadow structure and the penumbra transitions. *Astron. Astrophys.*, 307:635–644, 1996.

[44] J.J. McCarthy and T.V. Martin. A computer efficient model of earth albedo satellite effects. Technical Report 012-77, Planetary Sciences Department, NASA, Goddard Space Flight Centre, MD, 1977.

[45] D.M. Lucchesi. Non-gravitational perturbations on ETALONs satellites. In A. Elipe and P. Paquet, editors, *Proc of Workshop on Accurate Orbit Determination and Observations of High Earth Satellites for Geodynamics*, pages 77–84, Luxembourg, 1995.

[46] D. Vokrouhlicky, P. Farinella, and D. Lucchesi. Albedo perturbation models: General formalism and applications to LAGEOS. *Celestial Mechanics and Dynamical Astronomy*, 57:225–244, 1993.

[47] L.G. Jacchia. *COSPAR International Reference Atmosphere.* Academie-Verlag, Berlin, 1972.

[48] S. Aoki, B. Guinot, G.H. Kaplan, H. Kinoshita, D.D. McCarthy, and P.K. Seidelmann. The new definition of universal time. *Astron. Astrophys.*, 105:359–361, 1982.

[49] J.W. Marini and C.W. Murray. Correction of laser range tracking data for atmospheric refraction at elevations above 10 degrees. Doc. no. x-591-73-351, NASA, 1973.

[50] P.A. Cross. *Lecture Notes for the Residential Seminar on Advanced Least Squares Applied to Position Fixing.* North East London Polytechnic, 1982.

[51] D.M. Lucchesi and A.M. Nobili. Dynamics of 12-hour earth satellites. In A. Elipe and P. Paquet, editors, *Proc of Workshop on Accurate Orbit Determination and Observations of High Earth Satellites for Geodynamics*, pages 77–84, Luxembourg, 1995.

[52] W.M. Kaula. *Theory of Satellite Geodesy.* Blaisdell Publ. Co., Waltham Mass., 1966.

[53] A.T. Sinclair. The motions of the satellites of Mars. *Mon. Not. R. astr. Soc.*, 155:249–274, 1972.

[54] G.M. Appleby. Orbit determination of the Lageos and Etalon satellites - a comparison of geodetic results and orbital evolution of the Etalons. In *Proc.Conf. on Dynamics and Astrometry of Natural and Artificial Celestial Bodies*, pages 333–338, Poznan, Poland, 1994.

[55] A. Savitzky and M.J.E. Golay. Smoothing and differentiation of data by simplified least squares procedures. *Analytical Chemistry*, 36(8):1627–1638, 1964.

[56] D.E. Smith and P.J. Dunn. Long term evolution of the Lageos orbit. *Geopys. Res. Lett.*, 7:437–440, 1980.

[57] D.P. Rubincam. On the secular decrease in the semimajor axis of Lageos' orbit. *Celest. Mech.*, 26:361–382, 1982.

[58] G. Afonso, F. Barlier, C. Berger, F. Mignard, and J.J. Walch. Reassessment of the charged and neutral drag of LAGEOS and its geophysical implications. *J. Geophys. Res.*, 90:9381–9398, 1985.

[59] F. Barlier, M. Carpino, P. Farinella, F. Mignard, A. Milani, and A.M. Nobili. Non-gravitational perturbations on the semimajor axis of LAGEOS. *Ann. Geophysicae*, 4A:193–210, 1986.

[60] D.P. Rubincam. Drag on the LAGEOS satellite. *J. Geophys. Res.*, 95:4881–4886, 1990.

[61] D.P. Rubincam. Lageos orbit decay due to infrared radiation from the earth. *J. Geophys. Res.*, 92(B2):1287, 1987.

[62] D.P. Rubincam. Yarkovsky thermal drag on LAGEOS. *J. Geophys. Res.*, 93(B11):13805–13810, 1988.

[63] E.J. Opik. Collision probabilities with the planets and the distribution of interplanetary matter. *Proc Roy. Irish Acad.*, 54A:165–199, 1951.

[64] J.A. Burns, P.L. Lamy, and S. Soter. Radiation forces on small particles in the solar system. *Icarus*, 40:1–48, 1979.

[65] B. Bertotti and L. Iess. The rotation of LAGEOS. *J. Geophys. Res.*, 96(B2):2431–2440, 1991.

[66] R. Scharroo, K.F. Wakker, B.A.C. Ambrosius, and R. Noomen. On the along-track acceleration of the Lageos satellite. *J. Geophys. Res.*, 96:729–740, 1991.

[67] V. Shargorodsky, 1995. Personal Correspondence.

[68] L. Sehnel. Effects of the terrestrial infrared radiation pressure on the motion of an artificial satellite. *Celest. Mech.*, 25:169–179, 1981.

[69] D.M. Lucchessi and P. Farinella. *J. Geophys. Res.*, 1994.

[70] H.F. Fliegal, T.E. Gallini, and E.R. Swift. Global Positioning System radiation force model for geodetic applications. *J. Geophys. Res.*, 97(B1):559–568, 1992.

[71] B.D. Tapley, B.E. Schutz, R.J. Eanes, J.C. Ries, and M.M. Watkins. LAGEOS laser ranging contributions to geodynamics, geodesy and orbital dynamics. In *Contributions of Space Geodesy to Geodynamics: Earth Dynamics*, number 24 in Geodynamics Series, pages 147–173. AGU, Washington, DC, 1993.

[72] P. Gegout and A. Cazenave. Temporal variations of the earth's gravity field for 1985-1989 derived from Lageos. *Geophys. J. Int.*, 114:347–359, 1993.

[73] R.S. Nerem. Measuring temporal gravitational variations using SLR data. In *Satellite Laser Ranging in the 1990s. Report of the 1994 Belmont Workshop*, number 3283 in NASA Conf. Publ., 1994.

[74] C. Martin and D. Rubincam. Effects of earth albedo on the Lageos-1 satellite. *J. Geophys. Res.*, 101(B2):3215–3226, 1996.

[75] R.S. Nerem, B.F. Chao, A.Y. Au, J.C. Chan, N.K. Pavlis S.M. Klosko, and R.G. Williamson. Temporal variations of the earth's gravitational field from satellite laser ranging to LAGEOS. *Geophys Res. Lett.*, 20(7):595–598, 1993.

[76] R.J. Eanes and S.V. Bettadpur. Temporal variability of earth's gravitational field from satellite laser ranging. In R.H. Rapp, editor, *Proc. of Symposium G3, IAG Symposia Series*, 1996.

[77] I. Ciufolini. Measurement of the Lense-Thirring drag on high altitude, laser-ranged artificial satellites. *Phys. Rev. Lett.*, 56:278–281, 1986.

[78] IERS: Missions and goals for 2000. Central Bureau of IERS, Observatoire de Paris, 1995.

[79] A.M. Nobili. An international campaign for optical observations of geosynchronous satellites (COGEOS): Scientific aims and organization. *CSTG Bull.*, 9(19), 1987.

[80] F. Blesa, G. Catastini, and A.M. Nobili. Medium arc analysis of ETALON data with ORBIT10. In A. Elipe and P. Paquet, editors, *Proc of Workshop on Accurate Orbit Determination and Observations of High Earth Satellites for Geodynamics*, pages 49–54, Luxembourg, 1995.

[81] A.T. Sinclair. The determination of station coordinates and baselines from the 1986 and 1987 WEGENER/MEDLAS data by global and short-arc solutions. In *Fourth International Conference on the WEGENER/MEDLAS Project*, Scheveningen, 1989.

[82] 1994 IERS annual report. Central Bureau of IERS, Observatoire de Paris, 1995.

[83] Y. Vigue, S.M. Lichten, G. Blewitt, M.B. Heflin, and R.P. Malla. Precise determination of earth's center of mass using measurements from the global positioning system. *Geophys. Res. Lett*, 19(14):1487–1490, July 1992.

[84] P. Dunn. Personal communication, 1996.

# Appendix A

# Computation of orbital elements from rectangular coordinates.

For given instantaneous values $x, y, z$ and $\dot{x}, \dot{y}, \dot{z}$ of the geocentric rectangular coordinates and velocities of a satellite, we have

$$r^2 = x^2 + y^2 + z^2$$

$$v^2 = \dot{x}^2 + \dot{y}^2 + \dot{z}^2$$

Now from, for example, Kaula [52] we have that

$$v^2 = GM\left(\frac{2}{r} - \frac{1}{a}\right)$$

from which we obtain $a$, the semi-major axis. Then from Kepler's Third Law,

$$n^2 a^3 = GM,$$

we compute $n$, the mean motion.

Now

$$r = a(1 - e\cos E), \tag{A.1}$$

where $E$ is the eccentric anomaly and $e$ the eccentricity. So we can compute $e\cos E$. Now from Kepler's equation

$$M = E - e\sin E,$$

we have

$$\dot{M} = n = \dot{E} - e\cos E\dot{E},$$

or

$$\dot{E} = \frac{n}{1 - e\cos E}$$

So from equation (A.1), we have

$$\dot{E} = \frac{na}{r}$$

Now, by differentiating (5.1) we obtain

$$\dot{r} = ae\sin E\dot{E},$$

so,

$$\dot{r} = \frac{na^2e}{r}\sin E$$

So by using Kepler's Third Law again to substitute for $n$, we have

$$\dot{r} = \left(\frac{GM}{a^3}\right)^{\frac{1}{2}}\frac{a^2}{r}e\sin E,$$

or,

$$\dot{r} = \frac{(GMa)^{\frac{1}{2}}}{r}e\sin E$$

Thus we have $e\sin E$, and with $e\cos E$ from above, we can compute $e$ and $E$.

Now the angular momentum vector $\mathbf{h}$ is by definition perpendicular to the orbital plane and expressed as $\mathbf{h} = \mathbf{x} \times \dot{\mathbf{x}}$. In component form this is

$$\mathbf{h} = (h_1, h_2, h_3) = (y\dot{z} - z\dot{y}, z\dot{x} - x\dot{z}, x\dot{y} - y\dot{x}) \tag{A.2}$$

The situation is shown in Figure A.1.

From figure A.1, $h_3 = \cos I$. We now denote by $n$ the unit vector from 0 towards the Right Ascension of the orbital ascending node on the Earth's equator. This vector has components $(\cos\Omega, \sin\Omega, 0)$

From the figure,

$$\mathbf{z} \times \hat{\mathbf{h}} = n\sin I \tag{A.3}$$

Now, $\mathbf{z} = (0, 0, 1)$, so $\mathbf{z} \times \mathbf{h} = (-h_2, h_1, 0)$

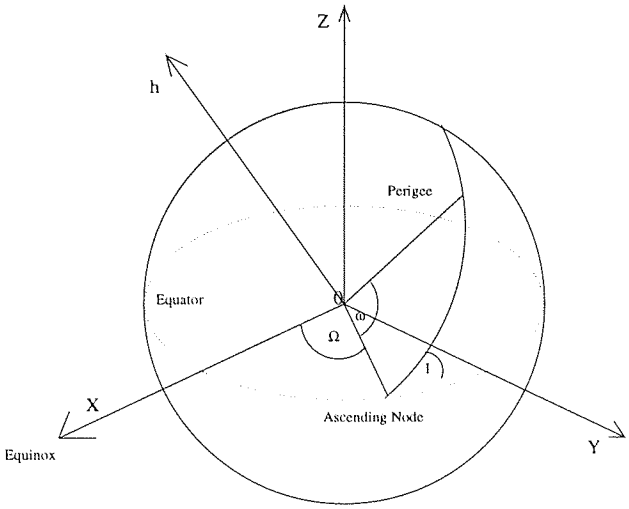


Figure A.1: The Orbital Elements $I, \Omega, \omega$

So from equation A.3, $h_2 = -\sin I \cos \Omega$ and $h_1 = \sin I \sin \Omega$

Then

$$\mathbf{h} = (\sin I \sin \Omega, -\sin I \cos \Omega, \cos I) \tag{A.4}$$

Then by equating the two expressions for the components of $\mathbf{h}$, equations A.2 and A.4, we can obtain $I$ and $\Omega$.